

TABLE OF CONTENTS

	Page
INTRODUCTION	1
I Prosthetic Proprioception through Soft Microfluidic Sensing	5
CHAPTER 1 CONTEXT & LITERATURE REVIEW	7
1.1 The human touch sensors	7
1.2 Prosthetic touch sensory needs	10
1.3 Artificial proprioceptive sensing technologies	11
1.3.1 Strain gauges	12
1.3.2 Optical sensors	13
1.3.3 Piezo-resistive sensors	13
1.3.4 Capacitive sensors	14
1.3.5 Magnetic position mapping	15
1.3.6 Inertial measurement units	15
1.3.7 Microfluidic sensors	16
1.4 Research conducted: soft sensors for a prosthetic Hand	17
1.4.1 Soft microfluidic strain sensor	17
1.4.2 Soft microfluidic skin sensor	19
1.4.3 Soft wearable artificial skin for hand motion detection	21
CHAPTER 2 SOFT MICROFLUIDIC STRAIN SENSOR	25
2.1 Sensor design	25
2.1.1 Conductive liquids	26
2.1.1.1 Ionic solution	26
2.1.1.2 Eutectic Gallium-Indium	27
2.1.2 Electrically conductive interface	28
2.1.3 Electrical interface	32
2.2 Fabrication	34
2.3 Results	37
2.3.1 Sensor resistance variation under strain	41
2.3.2 Comparaision with eGaIn	41
2.3.3 Frequency dependency of the sensor impedance	44
2.3.4 Sensor stiffness	45
CHAPTER 3 SOFT MICROFLUIDIC SENSITIVE SKIN	47
3.1 Tomographic imaging and ionic liquid microchannel embedded silicone sensor	47
3.2 Design and fabrication	51
3.2.1 Sensor base layer and soft electrodes	51

3.2.2 Injection of RTIL into the sensor 53

3.2.3 Sealing of the sensor 56

3.3 Simulation 57

3.4 Experiments: contact location and image reconstruction 61

3.4.1 Sensing mechanism of the skin 61

3.4.2 EIT image reconstruction 62

CHAPTER 4 SOFT WEARABLE MICROFLUIDIC SKIN FOR HAND MOTION DETECTION 67

4.1 Design 67

4.1.1 Sensor configuration 67

4.1.2 Detection mechanism 69

4.1.2.1 Microfluidic sensing 69

4.1.2.2 Conductive liquids 70

4.1.3 Instrumentation circuit 70

4.2 Manufacturing 72

4.2.1 Mold preparation 74

4.2.2 Skin sensor layer 74

4.2.3 Sealing and injection 75

4.2.4 Signal wires and hand fasteners 75

4.3 Data collection and signal processing 75

4.4 Preliminary characterization 76

II Prosthetic actuation through the "Programmable Permanent Magnet" actuator 79

CHAPTER 5 THE "PROGRAMMABLE PERMANENT MAGNET" ACTUATOR 81

5.1 A novel paradigm for torque generation 83

5.2 The PPM actuator design 88

5.2.1 Recent approaches 88

5.2.2 Magnet Selection 90

5.2.3 Halbach magnetic circuit 93

5.2.3.1 Benefits 93

5.2.3.2 Design 96

5.2.4 Actuator prototype 97

5.3 Experimental results 100

5.3.1 Actuator torque output 100

5.3.2 Halbach magnetic flux density 101

5.3.3 Pulse characterization 102

CONCLUSION AND RECOMMENDATIONS 105

6.1 Microfluidic sensing 106

6.1.1	Reframing contemporary microfluidics	106
6.1.2	Recommendations on microfluidic sensing	108
6.1.2.1	Liquids for microfluidics	108
6.1.2.2	Interconnects for microfluidics	109
6.2	Prosthetic actuation	109
6.2.1	Prosthetic and robotic actuation	109
6.2.2	Recommendations for the PPM actuator	111
BIBLIOGRAPHY		114

LIST OF FIGURES

	Page
Figure 0.1	Photo for real life upper limb prostheses 2
Figure 0.2	Images extracted from recent movies and illustrating ULPs ideal capabilities 3
Figure 1.1	Illustration of the mechanoreceptors of the skin..... 8
Figure 1.2	Photos of the Soft Strain Sensor 18
Figure 1.3	Photos of the Soft Microfluidic Artificial Skin 20
Figure 1.4	Photos of the Wearable Soft Skin for Hand Motion Detection 22
Figure 2.1	Schematic of the sensor and equivalent electrical circuit 25
Figure 2.2	Impact of NiCCF on elastomer interfaces residual strain 29
Figure 2.3	Comparison of the mechanical response of doped elastomer..... 30
Figure 2.4	Scanning electron microscope image of the conductive silicone nanocomposite 31
Figure 2.5	Schematic of the Soft strain sensor circuit design and resulting PCB..... 32
Figure 2.6	Schematic of the soft strain sensor fabrication and assembly procedure 34
Figure 2.7	3-D Image of the acrylic mold after laser engraving 35
Figure 2.8	3-D images of the sensor composite interface 36
Figure 2.9	Photo of the soft strain sensor test setup 39
Figure 2.10	Resistance variation as a function of strain for the ionic solution sensor. 41
Figure 2.11	Resistance variation as a function of strain for the eGaIn sensor. 42
Figure 2.12	Normalized change in resistance as a function of strain for saline-filled and eGaIn-filled soft strain sensors. 43

Figure 2.13	Normalized change in the oscillation period as a function of strain for the sensor filled with ionic solution.	44
Figure 2.14	Stress-strain relationship of the soft strain sensor.	45
Figure 3.1	Schematic of the EIT acquisition protocol.	48
Figure 3.2	Schematic of a possible conductive chain path in a piezoresistive composite	49
Figure 3.3	Photo of the complete skin sensor prototype	50
Figure 3.4	Schematic of the soft skin manufacturing process.....	52
Figure 3.5	Close up photo of the laser engraved mold	53
Figure 3.6	Details of the mesh layer mold and resulting net like structure.....	55
Figure 3.7	Simulation's voltage pattern example.....	57
Figure 3.8	Simulation's conductivity changes as a function of pressure	58
Figure 3.9	Simulation of single and double point load.....	60
Figure 3.10	Photo of the experimental setup.....	63
Figure 3.11	Pressure localization and Force discrimination experiments	64
Figure 3.12	Two point load experiment results	64
Figure 4.1	Photos of the artificial skin prototype	68
Figure 4.2	Schematic of the complete artificial skin sensing system.....	71
Figure 4.3	Schematic of the artificial skin manufacturing process	73
Figure 4.4	Psoc raw experimental data during strain and curvature experiment.	77
Figure 4.5	Photos of the real-time sensing and 3-D graphical reconstruction	78
Figure 5.1	Photos of the PPM prototype.....	81
Figure 5.2	Maxon 339286 brushless motor power characteristics.....	84
Figure 5.3	PPM actuator power characteristics.....	86
Figure 5.4	Low speed actuators efficiency comparison	88

Figure 5.5	Schematic of the typical ferromagnetic material hysteresis curves.	91
Figure 5.6	Second quadrant of the BH curve and $\frac{B_r}{H_{ci}}$ ratio for various Ferromagnetic materials	92
Figure 5.7	Schematic of typical Halbach arrays configurations	93
Figure 5.8	FEA magnetostatic simulation of the one Halbach array	94
Figure 5.9	FEA maximum torque function, mesh, and magnetic flux density with core magnet.	95
Figure 5.10	Halbach magnet positioning equations and example.....	97
Figure 5.11	General system diagram of the PPM actuator	99
Figure 5.12	Robotiq 2-finger gripper with PPM motor grabbing a stress ball.	100
Figure 5.13	Experimental actuator torque as a function of capacitors terminal voltage.	101
Figure 5.14	Graph of the experimental Halbach array magnetization curve.....	102
Figure 5.15	Current pulses in a Halbach array	103

LIST OF ABBREVIATIONS

AC	Alternating current
AlNiCo	Aluminum-Nickel-Cobalt
DC	Direct current
eGaIn	eutectic Gallium-Indium
EIT	Electrical Impedance Tomography
EMISE	1-Ethyl-3-Methylimidazolium Ethyl Sulfate
EPM	Electropermanent
FEA	Finite Element Analysis
HTMR	High Threshold Mechanoreceptors
IA	Intermediate Adapting
IL	Ionic Liquid
LTMR	Low Threshold Mechanoreceptors
NdFeB	Neodymium-Iron-Boron
NiCCF	Nickel Coated Carbon Fibers
NiNs	Nickel Nano-strand
PCB	Printed Circuit Board
PPM	Programmable Permanent Magnet
PSoC	Programmable System on Chip
RA	Rapidly Adapting

XX

RTIL	Room Temperature Ionic Liquid
SA	Slowly Adapting
SmCo	Samarium-Cobalt
ULP	Upper Limb Prosthetic
MCP	Metacarpal-phalangeal (joint)
PIP	Proximal inter-phalangeal (joint)
IP	Inter-phalangeal (joint)

LISTE OF SYMBOLS AND UNITS OF MEASUREMENTS

<i>A</i>	Ampere
°C	Celsius degrees
<i>cm</i>	Centimeter
<i>dB</i>	Decibel
<i>g</i>	Grams
<i>H</i>	Henry
<i>Hz</i>	Hertz
<i>J</i>	Joule
<i>kHz</i>	Kilohertz
<i>m</i>	Meter
<i>mA</i>	Miliampere
<i>ml</i>	Milliliter
μm	Micrometer
μF	Microfarad
<i>mm</i>	Millimeter
<i>N</i>	Newton
Ω	Ohm
<i>Pa</i>	Pascal
<i>kA</i>	kiloampere

<i>kPa</i>	Kilopascal
<i>kΩ</i>	Kilo ohm
<i>kV</i>	KiloVolt
<i>rad</i>	Radians
<i>rpm</i>	Rotations per minute
<i>S</i>	Siemens
<i>T</i>	Tesla
<i>V</i>	Volts
<i>W</i>	Watt

INTRODUCTION

Everyone has a plan 'till they get punched in the mouth.

M. Tyson

The goal of this thesis is to improve the design of prosthetics. The absence or loss of a limb is probably one of the most prejudicial impairments one can suffer. Since this handicap is often highly impactful on one's quality of life, current healthcare best practice aspires at restoring some degree of function and independence through the use of a prosthetic limb. However, prosthetics are still far less capable than biological organs.

To assess the use of prosthetics worldwide is hard because access to healthcare as well as statistical compilations differs among countries. Besides, causes for amputation vary widely. In developed countries, vascular dysfunction associated with diabetes is pervasive and on the rise. In developing countries, trauma either caused by wars, landmines or heavy machinery is the prevalent cause (Esquenazi (2004)). As an example, amputations in the U.S. number between 50,000 to 158,000 every year (Pezzin *et al.* (2004); Esquenazi (2004)).

Because there are substantial differences in use and design between upper and lower limb prosthetics (Raichle *et al.* (2008)), this thesis will focus exclusively on upper limb prosthetics (ULPs). ULPs can be divided in three groups: active and body powered, active and battery operated and passive prosthetics. Passive prosthetics appear to suffer less from maintenance and discomfort than their active counterparts, and can be extremely lifelike in appearance (Biddiss & Chau (2007)) but are, in return, quite limited in function.

ULPs rejection rates are consistently high. Biddiss & Chau (2007) computed rejection rates in a survey of 25 years of recent literature. Depending on the ULP type, mean adult rejection rates



Figure 0.1 Real life prostheses. Courtesy of the U.S. Army, by Walter Reed photographers.

are between 23% and 39%. However, the same survey shows how rejection rates appear to vary widely across papers. Using recent literature, it seems to be difficult to precisely identify the causes for prosthesis rejection (price, age of the subject, cause of limb loss, wait time before prosthetic fit, etc.).

However, one can easily observe the huge disconnect between reality (Fig 0.1) and the dream prosthetic such as portrayed in popular work of fiction (Fig 0.2). Thus, we propose that increasing prosthetics functions and capabilities is an appropriate and relevant course of action that will drive adoption as well as improve users' quality of life.

In studies on user research priorities that were conducted over the past 25 years, and in which records were collected from hundreds of users, **heat dissipation** and **reduced weight** consistently appear as the most desired improvements by battery operated prosthetics users. Addi-

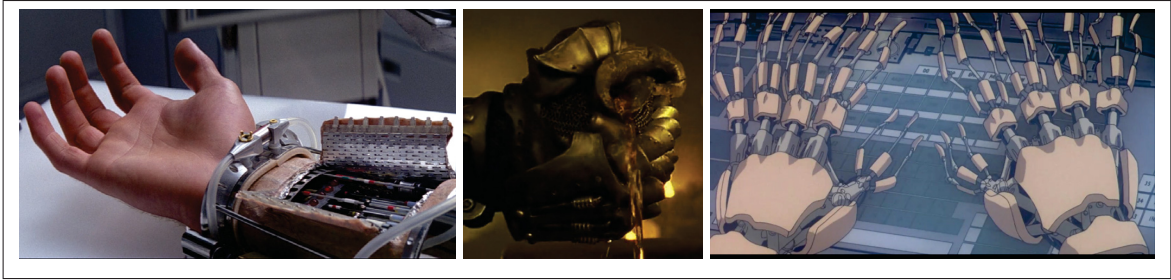


Figure 0.2 Pop culture images of ULPs. From left to right: "The Empire Strikes Back" ; "Army of Darkness" ; "Ghost in the Shell".

tionally, both battery and body powered prosthetics users identify **greater sensory feedback** and **increased dexterity** as high ranking priorities (Kejlaa (1993); Atkins *et al.* (1996); Biddiss *et al.* (2007)).

Based on these reported user needs, we propose two fundamental axes that can improve ULPs design: **Sensing** and **Actuation**.

Sensing. Our biological hands are equipped with touch, which is actually one of the most fundamental and vitally important senses that we have (Sacks (2009); Sainburg *et al.* (1995)). The sense of touch allows humans to explore and respond to their environment, as well as to intuitively know the body configuration through proprioception. The loss of a hand or arm causes the loss of touch, and although this loss can be counterbalanced through the sense of sight, it requires attention to be dedicated to the limb's actions. Therefore, instrumenting prosthetics is a first necessary step toward both restoring exploratory function and better prosthetic control.

Actuation. Weight and heat generation are one of the main user concerns. However, actuators – one of the principal sources of heat and weight – are vital components for both battery powered prosthetic actuation and haptic sensory stimulation. Furthermore, typical actuation struggles with generating large torques for extended period of times in an efficient manner and most prosthetics related applications such as prosthetic gripping, or haptic skin deformation,

precisely necessitate low speed and continuous high torque. Thus improving on actuators could yield tremendous improvements and should be a priority of ULPs design.

The work presented in this thesis addresses these two research problems. Thus, the thesis is divided in two parts, along two research axes: **Part I** is concerned with **Sensing** while **Part II** focuses on **Actuation**. Each part contains its own literature review, research corpus, and conclusion.

This thesis also addresses general ULPs design aspects. Rather than designing for a specific prosthetic model, we demonstrated research concepts that are applicable to many different ULPs. As a consequence, the ideas presented in this thesis are inspired from, and also readily transferable to a wide range of applications. The work introduced in this thesis will consequently include research fields such as soft sensing and bio-inspired robotics, wearable technologies, haptics and actuator design.

Part I

Prosthetic Proprioception through Soft Microfluidic Sensing

CHAPTER 1

CONTEXT & LITERATURE REVIEW

In preparing for battle, I have always found that plans are useless but planning is indispensable.

Dwight D. Eisenhower

It is commonly recognized that humans are equipped with five senses: taste, sight, touch, smell, and hearing. The sensory receptors, neural pathways, and brain structures from these five senses together form the sensory system.

The ultimate goal of a prosthetic is to substitute for the lost limb in an identical or even improved manner. Missing a hand diminishes not only the mechanical function of the body, but also its exploratory and sensitive capabilities. Among the five senses, touch is the only one which sensory receptors are scattered all over the body and within the skin. Therefore, any perfect limb prosthesis also needs to restore the human sense of touch.

In this thesis, we are concerned with Upper Limb Prosthetics. Consequently, Part I of this thesis will seek ways to emulate the sense of touch embodied in human hands, in prosthetics. In order to have a better idea of how to imitate the tactile sensory system, it seems judicious to first review its biological components.

1.1 The human touch sensors

The ability of our bodies to capture different types of information is granted by a variety of touch receptors. These touch receptors are the distal part of sensory neurons. When stimulated, sensory neurons transmit the information from the periphery to the cell body, situated in the spinal cord. Then, the sensory neuron's body processes the message up to the brain (Abraira & Ginty (2013); Li *et al.* (2011b)).

A multiplicity of touch receptors exist in our body, that allow us to discriminate between many different types of tactile events. Skin touch receptors are called mechanoreceptors, and their density varies according to the skin region as well as the type (hairy or glabrous) of skin, as illustrated in Fig 1.1.

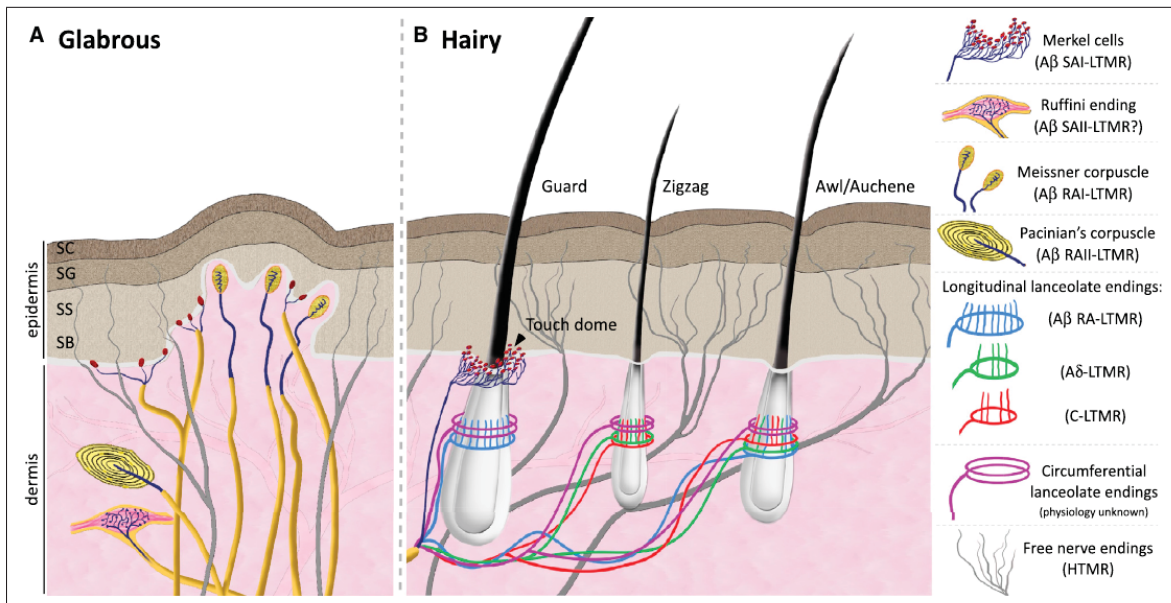


Figure 1.1 Illustration of the different types of Mechanoreceptors contained within the skin. Reproduced with permission (Abraira & Ginty (2013)).

Usually, one distinguishes mechanoreceptors (Vallbo & Johansson (1976); Vallbo *et al.* (1984)) according to their adapting speed (rapidly, intermediate, and slowly adapting: RA, IA, SA), their receptive field size, and their activation threshold (low or high threshold mechanoreceptors: LTMR, HTMR).

The adaptation speed of a mechanoreceptor regulates the type of stimulus it will react to. Slowly adapting mechanoreceptors will be continuously sending electrical pulses ("action potentials") during sustained indentation, whereas faster adapting mechanoreceptors will react only during transient deformations of the skin such as when exposed to vibrations. The receptive field size of a mechanoreceptor determines how much area they are capable of sensing.

In general this information is summarized in Tab. 1.1, although we refer the interested reader to Abraira & Ginty (2013) for an extensive review of the mechanoreceptors and somatosensory pathways.

Table 1.1 Typical skin mechanoreceptors classification (Abraira & Ginty (2013)).

Physiological subtype	Skin type	End organ Ending Type	Location	Optimal stimulus
SAI-LMTR	Glabrous	Merkel cell	Basal Layer of epidermis	Indentation
	Hairy	Merkel cell (touch dome)	Around Guard hair follicles	
SAII-LMTR	Glabrous	Ruffini	Dermis	Stretch
	Hairy	unclear	unclear	
RAI-LMTR	Glabrous	Meissner corpuscle	Dermal papillae	Skin movement & Hair follicle deflection
	Hairy	Longitudinal lanceolate ending	Guard & Awl-Auchene hair follicles	
RAII-LMTR	Glabrous	Pacinian corpuscle	Deep dermis	Vibration
A δ -LMTR	Hairy	Longitudinal lanceolate ending	Awl-Auchene & Zigzag hair follicles	Hair follicle deflection
C-LMTR	Hairy	Longitudinal lanceolate ending	Awl-Auchene & Zigzag hair follicles	Hair follicle deflection
HMTR	Glabrous & Hairy	Free nerve ending	Epidermis & Dermis	Noxious mechanical

Although the skin is the principal organ of touch, two other touch receptors are also present in deeper tissues:

- Golgi tendon organs, which allow us to feel the amount of force exerted by the muscles;
- Muscle spindles, which have the ability to sense the muscle elongation, and thus grant us the ability to map the position of our limbs.

The role of each touch receptor is still not always clearly identified. Not only are different types of mechanoreceptors activated through the same tactile events, but also our conscious perception of the sense of touch arises from the complex processing of the action potentials from all the tactile sensors, through the central nervous system.

For these reasons, rather than studying the sense of touch as a unique inseparable sense, or dividing it down to each neurobiological receptor, a compromise is often made and touch is roughly subdivided into three different psychophysical components (Abraira & Ginty (2013)):

- Exteroceptive. The perception of stimuli originating from outside the body such as pressure, vibration, wetness. (RAI-, RAII-, SAI- and SAII-LTMRs);
- Interoceptive. The perception of stimuli originating from inside the body such as pain, heat or itching (HTMR);
- Proprioceptive. The perception of the body posture in space (the "body schema"), such as knowing where a limb is without looking at it (SA-II-LTMRs, Golgi tendon organs, Muscle spindles, vision, audition), as well as the perception of the body position in space relative to the environment. ¹

1.2 Prosthetic touch sensory needs

Within this framework – Interoception, Exteroception, or Proprioception – we now can ask ourselves which part of touch we aim to restore. As proposed in the introduction, prosthetic users report a need for more sensitive feedback as well as increased dexterity.

Interoception is mainly concerned about the pain sensation that allows us to feel damage done to the limbs. It is not the first part of touch that we will consider repairing.

¹ Stricter definitions of proprioception are commonly used. In our case, since we are ultimately concerned with using a prosthesis to interact with the world, we chose this rather broad definition. This definition is also supported by the fact that both vision as well as some components of audition (inner ear) are involved in the mental body representation (Proske (2015); Làdavas & Pavani (1998)).

Exteroception is extremely important. It allows us to feel objects in contact: surface textures, shear forces, pressure, and many others. Building exteroceptive sensors is one of the avenues pursued by the CoRo laboratory, and multimodal tactile sensors have been created (Duchaine & Rana (2014); Rana *et al.* (2016); Le *et al.* (2017)). These sensors can detect forces as well discriminate between surfaces of different roughness (Rispoli *et al.* (2017a,b)).

This thesis has been realized concurrently to the work on exteroception, and therefore explored the subject of proprioception. Since all touch receptors are missing, the only way for a ULP user to know its prosthetic limb position in space is to look at it. That action induces a bigger cognitive load on the user than when equipped with proprioceptors. In other words, proprioceptive feedback through vision burdens the user.

Studies in human and non-human primates have shown that simple tools, even though they do not contain proprioceptors and are not part of our body (Maravita & Iriki (2004)), may be integrated through experience, within our body schema. This suggests that humans may have the ability to incorporate passive prosthetics too, within the body mental representation.

Since our ultimate goal is a prosthetic that imitates the biological human hand, we are designing for 24 to 26 degrees of freedom prosthetic. There is, beyond any doubt, a need for incorporating proprioceptors to the prosthesis.

1.3 Artificial proprioceptive sensing technologies

In order to be able to give to ULPs users a synthetic yet intuitive sense of proprioception, we first need to capture the position of the prosthetic. In order to fulfill this task, we need to equip the prosthetic with sensors. Since we are designing a solution that should fit to a wide array of ULPs, we do not want to assume anything about the prosthetics mode of actuation, shape, or in general, internal structure.

This work being done in conjunction with exteroceptive sensors design, which will be located on the prosthetic's palm and finger pads, our sensors should ideally be located on the outward

facing part of the prosthetic. In addition, these sensors should not add significant weight and bulkiness to the prosthetic.

Therefore, we propose the general sensor's shape to be some sort of strain sensitive skin. This skin should cover the back of the prosthetic and would be able to sense the prosthesis movements.

In many respects, this work straddles the line between the fields of robot sensing and artificial skin (Lumelsky *et al.* (2000); Cutkosky *et al.* (2008)) and human motion capture (Sturman & Zeltzer (1994); LaViola (1999); Dipietro *et al.* (2008)). We will hence start by presenting the most recent academic progress as well as past commercial endeavors in both these fields.

1.3.1 Strain gauges

Maybe the most widespread type of strain sensor – strain gauges – exploit the change in resistance of a conductor as it is deformed through elongation.

In robotics, strain gauges have been widely used as sensors in many applications (Carrozza *et al.* (2000); Butterfaß *et al.* (2001); Feliu & Ramos (2005)) for their mechanical and electrical simplicity, compact form factors and cost effectiveness. Strain gauges have also been used to monitor bending angles in glove-based motion capture devices (Simone *et al.* (2007); Gentner & Classen (2009)).

Indeed, strain gauges provide relatively high accuracy for measuring small strains. However, the measurement range of conventional strain gauges is limited by the material of the sensor, typically on the order of 1% or less, thus making them unsuitable for soft structures that may experience large deformations and strains.

1.3.2 Optical sensors

Light can also be harnessed for sensing. Light possesses inherent qualities that make it a great tool for sensing and information delivery. Not only is it unaffected by electromagnetic interference but it also can carry a large amount of information thanks to a large bandwidth.

For these reasons, optical sensors are indeed used widely for measuring strain of large magnitude in robotics (Suganuma *et al.* (1999); Kiesel *et al.* (2007); Park *et al.* (2009); Dobrzynski *et al.* (2011)) as well as for hand pose estimation (Wise *et al.* (1990); Williams *et al.* (2000); Li *et al.* (2011a)). However, due to the nature of the waveguides and of the computing speed required to process information, optical sensing is often bulky and difficult to integrate into soft and wearable structures.

As an answer to this issue, recent papers tend to bypass this problem by designing diffuse waveguides. Instead of using spectrum analysis, they rely purely on the signal amplitude as a measure of the strain (To *et al.* (2015); Zhao *et al.* (2016)). By doing so, both the computing power and waveguide manufacturing requirements are relaxed.

As demonstrated as soon as 1989 by Lumelski and Cheung (Cheung & Lumelsky (1989, 1992)), sensing through light does not necessarily requires waveguides. Light based sensing from an external frame of reference, such as when using multiple cameras, has also been used to measure the movement of human hands (Garg *et al.* (2009); Kim *et al.* (2012)), human whole-body movement, as well as to track robot motion.

These systems, however, must often be operated within a controlled environment. They can suffer from occlusion and, as they do not control the medium through which the light moves, also become more sensitive to interference.

1.3.3 Piezo-resistive sensors

Several researchers have proposed the use of silicone micro-composites (Knite *et al.* (2004)) or more recently nano-composites (Kang *et al.* (2006); Johnson *et al.* (2010a)) to build piezo-

resistive soft strain sensors. Using comparable manufacturing methods, larger soft piezoresistive skins for robotic sensing have also been fabricated (Shimojo *et al.* (2004); Duchaine *et al.* (2009)).

As sensitive skins are formed of many sensors, wiring and signal routing frequently becomes an issue. Advanced imaging techniques such as Electrical Impedance Tomography (EIT) have been proposed to circumvent this drawback (Nagakubo *et al.* (2007); Kato *et al.* (2007); Elsanadedy (2012); Tawil *et al.* (2009)).

Unlike their metallic alternatives, sensors made of silicone can sustain very large elongations and typically have relatively high gauge factors (Loh *et al.* (2008)) due to the bandgaps resulting from the change in the inter-atomic spacing.

However, the latter characteristic makes their output highly nonlinear and thus difficult to predict (Lacasse *et al.* (2010)). Indeed, the change in the resistance of such materials is dominated by much more complex effects such as quantum tunneling (Hu *et al.* (2008); Johnson *et al.* (2010b)) rather than simple changes in geometry, making their responses nonlinear and often prone to hysteresis.

1.3.4 Capacitive sensors

Capacitive sensors have been a very popular choice for force sensing in the recent years (Hoshi & Shinoda (2006); Maggiali *et al.* (2008); Ulmen & Cutkosky (2010); Rana *et al.* (2016)). Indeed, when appropriately used, capacitance allows for high sensitivity measurements.

However, as has already been pointed out, capacitance measurements usually only have a narrow range sensitivity and use moderately complex electronics (Rana *et al.* (2016)). Hence, capacitance measurements in soft and highly conformable sensors may be hard to measure over very large strains.

1.3.5 Magnetic position mapping

Magnetic sensors can be used to track and reconstruct position (Mitobe *et al.* (2006)). Due to the nature of electromagnetism, one can obtain very precise measurements at high acquisition rates with these sensors. Due to their nature, they are however highly sensitive to electromagnetic noise.

Many battery powered prosthetics use electromagnetic actuators, which tend to induce electromagnetic interference. Moreover large parts of the electromagnetic spectrum are used continuously around us for a large number of applications such as communication. Therefore these sensors do not seem appropriate for our application.

1.3.6 Inertial measurement units

Recent years have seen tremendous developments in micro-electro-mechanical systems leading to the design and commercialization of new small and cheap Inertial Measurement Units (IMUs) and accelerometers. These have been used as sensors for hand motion tracking (Lin *et al.* (2014); Kortier *et al.* (2014); Hsiao *et al.* (2015)).

However, these sensors are actually ill-suited by design to accomplish such a task over long periods of time. Indeed, the sensors forming an IMU usually measure acceleration, rotation rate, and the earth's magnetic field, each along three axes.

Although precise orientation maybe obtained by the combination of the magnetometer and gyroscope, to obtain an exact position necessitates to integrate data from the accelerometer over time, twice. This yields velocity and then position in space. Because of the imperfect nature of the computation and sensing, the position error tends accumulate over time, making the device imprecise, and requiring either frequent calibration or an external reference.

1.3.7 Microfluidic sensors

Usually made of very flexible and stretchable polymers with embedded conductive liquids, microfluidic sensors are in many ways very similar to strain gauges. The change of the resistance of these soft sensors is a function only of the change in geometry, that is, the length and the cross-sectional area of the microchannels. Their output is therefore nearly linear over a wide range of strain and hence easily predicted. These qualities make these sensors good candidates for soft robotics and prosthetics applications.

It has been observed that conductive liquid metal alloys such as eutectic Gallium-Indium (eGaIn) are extremely well suited for use in microchannels to create soft electrical wiring (Dickey *et al.* (2008)).

Indeed, highly stretchable sensors composed of a hyperelastic elastomer and embedded microchannels filled with eGaIn have demonstrated relatively high accuracy and reliability for measuring large strains (Park *et al.* (2010, 2012a); Tabatabai *et al.* (2013); Park *et al.* (2014)), contact pressures (Park *et al.* (2012a,b); Wong *et al.* (2012)), shear forces (Vogt *et al.* (2013)) and curvatures (Majidi *et al.* (2011)).

For example, Kramer *et al.* (2011b) used this technology as a single axis curvature sensor to monitor the bending angle of a finger joint. However, there are certain limitations of the applicability of eGaIn for this purpose. Although its relative response in terms of resistance is reliable, the absolute difference between the resistance of the unbent and the fully bent sensor remains small, due to the high conductivity of eGaIn (Kramer *et al.* (2011b)).

As subsequently pointed out by Majidi *et al.* (2011), this low resistivity makes the sensor sensitive to electrical noise and variations in the interface resistance due to factors such as movement of connecting wires. Furthermore, since the entire sensor is wired with eGaIn, any external stimulus changing the geometry of a channel dedicated to signal routing could be interpreted as a strain.

Hence, as part of the larger growing trend toward soft and stretchable electronics, one may not be satisfied by using only liquid metal alloys as the single material for the manufacture of soft stretchable microfluidic electrical components. Indeed, other types of conductive liquids exist, such as ionic solutions and Room Temperature Ionic Liquids (RTILs), and have recently started to be used in microfluidics too (Zhu *et al.* (2009); Noda *et al.* (2010); Wu *et al.* (2011); Yan & Pan (2011)). Contrary to liquid metal alloys in which electrons move freely, these liquids conductivity derives from the movement of ions. As such, they exhibit very different electrical characteristics.

1.4 Research conducted: soft sensors for a prosthetic Hand

Based on the different technologies available presented above, and their respective shortcomings, we will now present the research that has been conducted.

1.4.1 Soft microfluidic strain sensor

As a first step toward a full prosthetic skin capable of measuring the hand position, we created a strain sensor. Requirement for this sensor were that it should be extremely soft and capable of withstand and measure very large strains. In addition, the sensor should not only we be able to connect to it in a reliable way with conventional electronics, but also should be able to separate sensing from signal routing, so that ultimately the prosthetic skin would be made of the same flexible material connected to single remote computing element.

Indeed, due to the unstructured nature of the environment in which a prosthetic hand will be used, it is obvious that soft wires located on the back of the hand will be subject to occasional stresses such as contact with an object. Ideally, these uncontrolled contacts should not affect the sensors measures.

Different technologies available were reviewed, microfluidic sensors seemed the only option offering a simple and reliable way to measure large strains without complex electronics or a bulky and complex device.

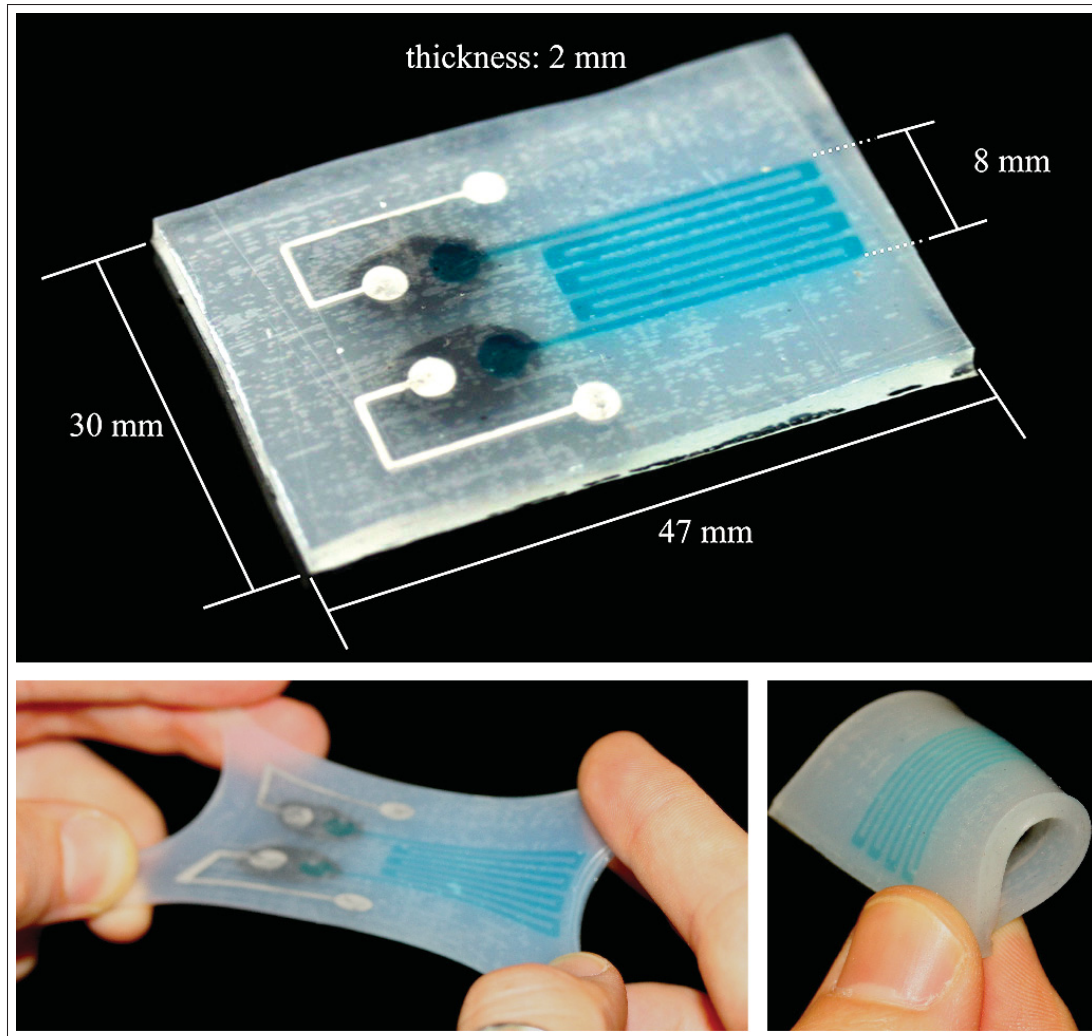


Figure 1.2 Hybrid soft strain sensor prototype.

However, microfluidic sensors seemed to be suffering from unreliable connections to conventional electronics (Majidi *et al.* (2011)), and to the best of our knowledge, no microfluidic sensor had embedded both sensory and signal routing microchannels.

The research conducted thus addressed these two issues:

- In order to make the sensors only measure the strain applied at desired measurement area, channels were filled with different types of conductive liquids. While eGaIn channels were

dedicated to routing the electrical signal, thus acting as soft wires, an ionic solution was used as sensing element;

- In order to connect the conductive liquids either together or with external electronics, soft conductive interfaces were manufactured by doping the elastomer with conductive nanoparticles.

Chapter 2 of this thesis will be dedicated to the manufacturing of this microfluidic strain sensor. The results of this hybrid approach led to a conference and a journal publication (Chossat *et al.* (2012, 2013)), and are illustrated in the Figure 1.2.

1.4.2 Soft microfluidic skin sensor

During our work on unidirectional soft microfluidic sensors we uncovered several difficulties related to microfluidic sensor manufacturing. This subsequent work represents our efforts in addressing these shortcomings with the goal of easing the making of microfluidic devices, as well as our exploration of alternative microfluidic sensing modalities.

The first issue we decided to tackle is the sensors manufacturing complexity. Indeed, the extreme softness of the materials often used for microfluidic sensors makes their handling both difficult and hardly reproducible. In addition, the interplay between the surface tension of the conductive liquids, the size of the microchannels, and the polymer's hydrophobicity often causes difficulties for embedding conductive liquids in the sensor.

Although the method used in the first chapter (injection) is reliable, it seemed fundamentally associated with the unidirectional inflow of liquid and outflow of air, from a single channel. The above mentioned manufacturing method, although fine for a unidirectional sensor, would not work to fill multiple interconnected microchannels.

A second shortcoming, regardless of the technology used, concerned a common issue with sensitive skins. The connection of multiple sensing elements or sensor array leads to complicated internal wiring. In order to circumvent the associated physical constraints, the use of a

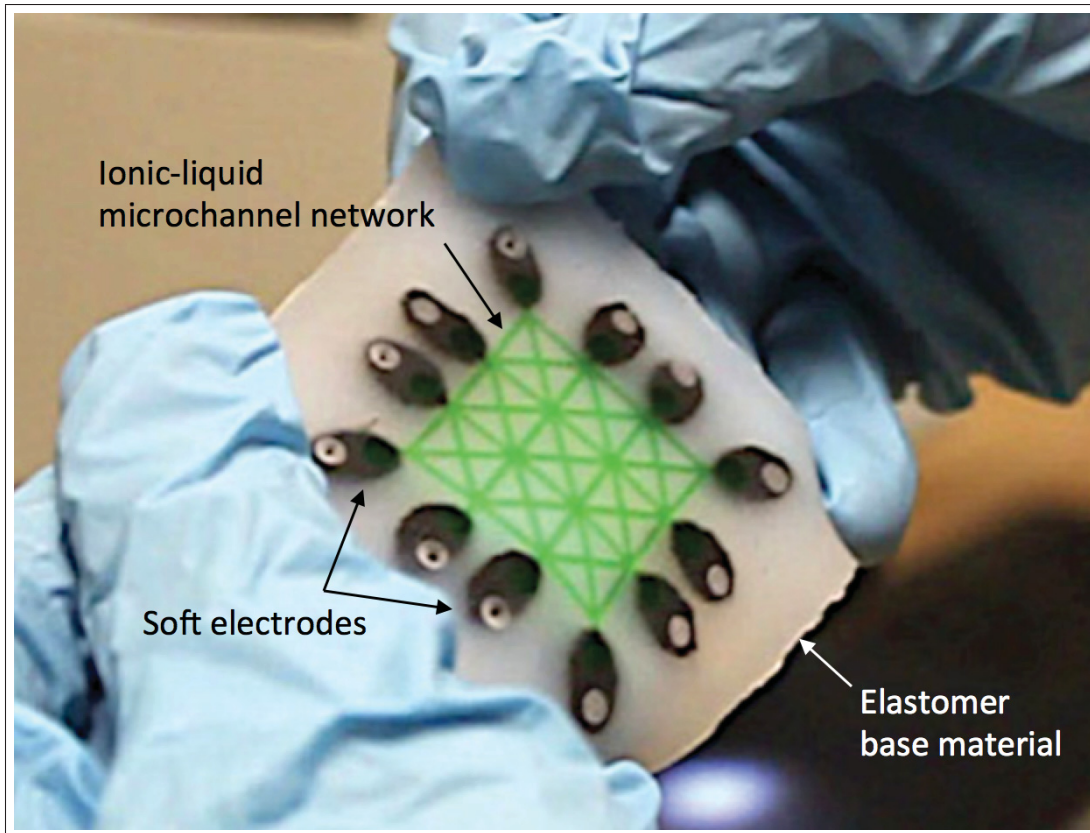


Figure 1.3 Artificial skin prototype with an embedded ionic-liquid microchannel network.

flexible Printed Circuit Boards (PCBs) layer or flexible/stretchable wires has been proposed. However, this method also limits the robustness of the device and its mechanical properties such as flexibility and stretchability.

To solve our first manufacturing problem, we created a soft structure that would allow for the air to be naturally expelled out of the sensor while the injected conductive liquid – an Ionic Liquid (IL) in our case – would be retained. This method allowed for easier and robust manufacturing of a soft microfluidic sensitive skin.

To remedy to second issue, we proposed the use of EIT combined with an conductive liquid embedded soft sensor (Figure 1.3) for tactile sensing.

This EIT based tactile sensing technique simplifies the previously mentioned complicated internal wiring since deformations caused by contact pressures on a large flexible surface can be easily measured without constraining the mechanical properties of the material.

As a third improvement over the previous design, we used a low conductive RTIL in concert with eGaIn. RTILs are chemically stabler when compared to ionic solutions (e.g. saline solutions) that are composed of water and ions, while also retaining lower surface tensions than liquid metals (e.g. gallium-indium alloys).

In other words, previous work on strain sensors was generalized to multiple interconnected microchannels. This was made through several improvements:

- Creating air permeable soft structure for microchannel filling during manufacturing;
- Using EIT in order to avoid wiring complexity;
- Injecting a new conductive liquid referred known as RTIL.

This work will be presented in Chapter 3 of the present thesis and led to a journal publication (Chossat *et al.* (2015a)).

1.4.3 Soft wearable artificial skin for hand motion detection

Building on the above mentioned research, we finally designed a soft wearable skin with multiple microfluidic strain sensors embedded, displayed in Fig 1.4. This skin, although tailored for human hand motion detection in the present thesis, was built with the goal of estimating the configuration of a ULP. As human hands are soft, extremely mobile, and of various sizes, we argue that it could be easily adapted to fit a ULP.

In order to design the soft wearable skin and as a complement to our knowledge of microfluidics, we inspired ourselves from past research and commercial endeavors in the field of gloved-based interfaces. Glove-based wearable sensing devices (Dipietro *et al.* (2008);



Figure 1.4 Wearable soft artificial sensing skin made of a hyperelastic elastomer material for detecting multi-joint motions.

Williams *et al.* (2000); da Silva *et al.* (2011); Li *et al.* (2011a)) are portable systems placed on or around the hand for detecting hand gestures by measuring the finger joint motions.

Various technologies have been proposed with slight functional or mechanical design differences. Although the research focus or target applications may not be always the same, many of them look like a glove that covers the entire user hand.

This field has indeed seen a variety of devices being developed since the 1970s for both research and commercial applications (Sturman & Zeltzer (1994); LaViola (1999); Dipietro *et al.*

(2008)). It is interesting to note that in spite of these efforts, these devices have yet to reach large scale commercial success.

The development of a practical hand motion detection system is promising, but appears to be only achievable by low-cost sensing materials that could provide relatively high accuracy and reliability on capturing complex hand's motions. Furthermore, the detection system should be compact, lightweight, mechanically simple, and convenient to use in various unconstrained environments, both indoor and outdoor.

We designed and manufactured a soft artificial skin with an array of embedded soft strain sensors that could detect various hand motions. Eleven embedded microchannel sensors filled with a RTIL provided a capability of tracking one DOF motion on 11 finger joints.

In addition to the RTIL, we used another type of conductive liquid (eGaIn) with much higher electrical conductivity for flexible and stretchable wiring.

This work, presented in Chapter 4, has been published as a conference paper (Chossat *et al.* (2015b)).

CHAPTER 2

SOFT MICROFLUIDIC STRAIN SENSOR

*Do not go gentle into that good night,
Old age should burn and rave at close of day;
Rage, rage against the dying of the light.*

*Though wise men at their end know dark is right,
Because their words had forked no lightning they
Do not go gentle into that good night.*

Dylan Thomas

2.1 Sensor design

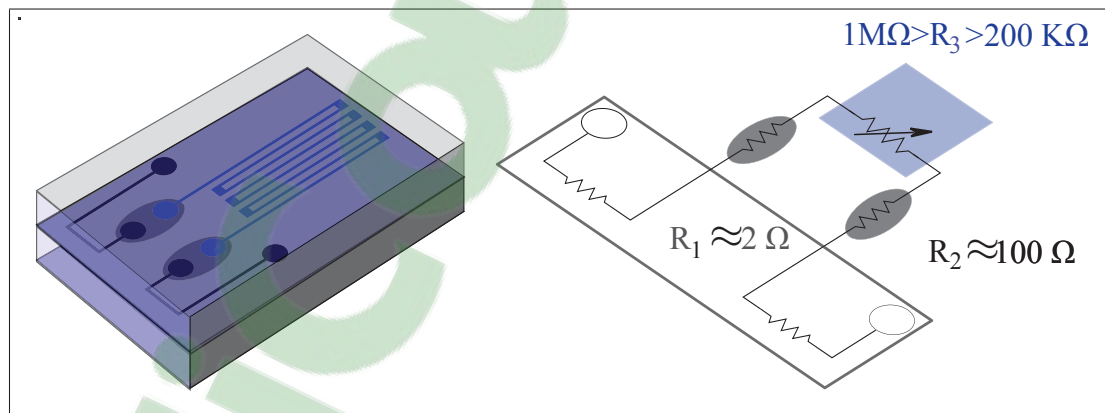


Figure 2.1 Schematic of the sensor and equivalent electrical circuit. R_1 , R_2 , and R_3 respectively being the eGaIn, doped silicone, and ionic solution resistances.

As mentioned in the introduction, we manufactured a soft microfluidic sensor with two different conductive liquids embedded. While this hybrid method allows us to have both soft

microfluidic wiring as well as soft microfluidic sensing in one hyperelastic sensor, it also created two main design challenges that we had to overcome:

1. The two liquids are required to be kept separate in order to prevent them from being mixed. As a consequence, we created solid yet soft conductive interfaces that were embedded between the two different microchannels;
2. The use of an ionic solution introduces constraints in the design of the associated electrical circuit since we must avoid electrolysis of the solution and polarization of the electrodes. Thus, a custom-designed circuit applies a low voltage AC current centered at 0 V with a fixed frequency range is used to electrically interface with the sensor.

This section is dedicated to presenting in detail the different elements of the sensor's design as illustrated by the Fig 2.1.

2.1.1 Conductive liquids

Our goal is to produce a soft sensor that is sensitive to strain generated by the movements of a prosthetic hand, and relatively insensitive to strain or stress occurring elsewhere on the glove. This motivated the use of a higher resistivity liquid in the sensing portion attached to the joints and of a more conductive liquid in the signal-routing portions attached to the static surfaces of the glove.

2.1.1.1 Ionic solution

The liquid used in the strain-sensitive portions of the sensor is a solution of sodium chloride (NaCl) in water (H₂O) containing glycerol (Atlas Laboratories). Glycerol was used for the increased viscosity of the solution (1:1 water/glycerol by volume).

NaCl was dissolved using a planetary mixer (Thinky ARE-310), which produces a centrifugal force of up to 400 g to ensure perfect dissolution. The solubility of NaCl in 1:1 water/glycerol

being 21.8 g per 100 ml at room temperature¹, our solution contained 19 g of NaCl per 100 ml. With this concentration, no precipitate formed in the sensor even with pressure or temperature variations.

The use of Ionic solutions for sensing have been previously proposed. Cheung *et al.* have proposed a cylindrical strain sensor using a saline solution and reported the analysis of the impedance of the solutions over a very wide range of frequency and strain (Cheung *et al.* (2008)).

However, the sensor was considerably larger than in the present study and involved the use of rigid metal electrodes. These two characteristics would make this sensor very difficult to be integrated into a compact, portable and soft application such as a proprioceptive glove.

Ionic liquids (IL) have also been used for monitoring fluid pressure in a microfluidic system in order to characterize flow conditions and liquid properties (Wu *et al.* (2011)).

2.1.1.2 Eutectic Gallium-Indium

The second liquid used in our sensor is an eutectic metal alloy consisting of gallium (75%) and indium (25%) (eGaIn, Sigma-Aldrich). Maintaining its liquid state at room temperature (15.7°C melting point), this alloy and Galinstan (Liu *et al.* (2010)), a similar alloy, are considered non-toxic alternatives to mercury (Dickey *et al.* (2008)).

With a resistivity of only a few $\text{m}\Omega/\text{cm}$ ($29.4 \times 10^{-6} \Omega/\text{cm}$; Dickey *et al.* (2008)), eGaIn has a conductivity close to that of copper. Both eGaIn and Galinstan have been used recently in flexible and stretchable electronics (Shaikh & Liu (2007); Irshad & Peroulis (2009); Lipomi *et al.* (2011); Cheng & Wu (2011)).

In our sensor, microchannels filled with eGaIn are used to supply electric currents to the strain-sensitive portion of the sensor and transmit the sensor signal. As previously demonstrated

¹ The solubility of NaCl at room temperature is 35.7 g per 100 ml in water and 7.8 g per 100 ml in glycerol.

(Cheung *et al.* (2008)), the resistivity of the saline solution is much greater than that of eGaIn. Indeed, the conduction mechanism of saline solution is fundamentally different from that of eGaIn, since it is the movement of hydrated ions that makes a saline solution electrically conductive.

2.1.2 Electrically conductive interface

Although the oxide skin of eGaIn (Dickey *et al.* (2008); Xu *et al.* (2012)) possesses many characteristics that would make it a good electrode for an ionic solution (highly conductive and oxidation resistant), the mechanical properties of both liquids make direct contact between them undesirable. The eGaIn viscosity is too low to prevent against the mixing of the two different liquids when under external stress.

One of the main challenges in this work was therefore to create a soft conductive interface between the saline solution and eGaIn. This soft interface must act as an electrode between the saline solution and the eGaIn-filled microchannels. It should be highly conductive but with very low piezoresistivity and should not affect the mechanical properties of the sensor. For this purpose, we use a platinum-cured silicone elastomer doped with conductive micro and nanoparticles.

Since the conductivity and the elasticity of the resulting composite have opposing dependencies on the amount of conductive particles, these two variables seemed irreconcilable. In order to minimize the loss of elasticity, we used nanoparticles with a high aspect ratio, since such geometry is known to provide good conductivity at lower filler volumes (Baldyga *et al.* (2008)).

The particle chosen was a nickel nano-strand (NiNs, length 30 μm , Conductive Composites inc.). Nickel is highly conductive, affordable, slow to oxidize, and hence suitable for our application. The nanopowder was incorporated into a very soft silicone (EcoFlex, Smooth-On) of Shore hardness 00-30. To avoid damage to the strands, the resulting composite was mixed for three minutes using a planetary mixer (Thinky ARE-310).

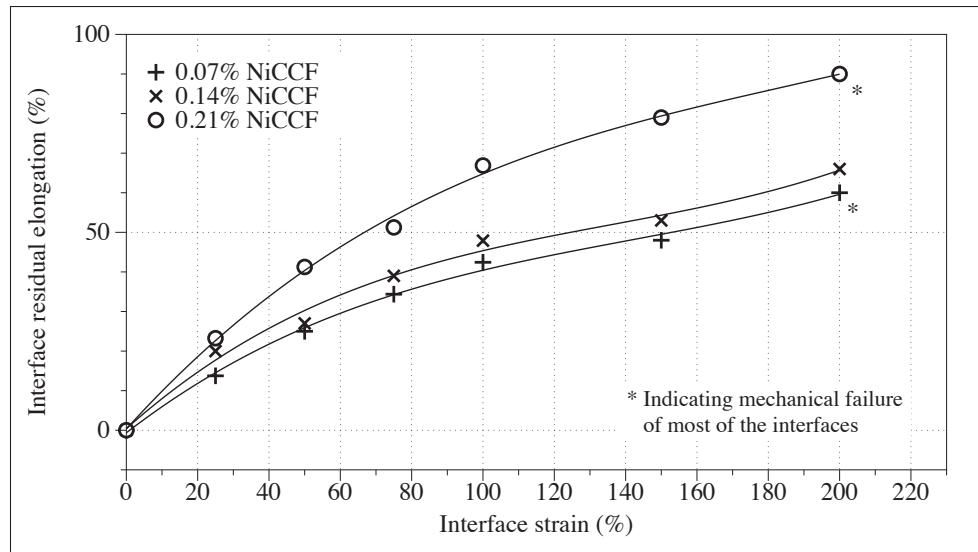


Figure 2.2 Impact of NiCCF volume on elastomer interfaces length after strain, as they get stretched over multiple length ratio (with fixed NiNs aspect ratio: 4% per vol.).

These high-aspect-ratio particles are known to form agglomerates in spite of powerful mixing (Baldyga *et al.* (2008)). In order to increase the overall electrical conductivity, we used a small amount of chopped nickel-coated carbon fiber (NiCCF, Conductive Composites inc.) to interconnect the nano-strand agglomerates (Chung *et al.* (2004)). Moreover, the Gallium contained in the eGaIn alloy, is known to corrode metals such as Nickel (Luebbers & Chopra (1995)), and even though very few contact points are possible, the use of carbon based fibers thus further increases the reliability of the interfaces in terms of conductivity.

It is also well known that long particles result in good conductivity at low filler volumes (Lee *et al.* (2012)). However, embedding long particles into a soft silicone matrix is also known for creating mechanical hysteresis. Extrusion was attempted as a mean to manually extrude aligned fibers. However, it ultimately failed because of the uncured polymer clotting even needless syringes.

Indeed, as pointed by Rogers *et al.* (2010), the large differences in mechanical properties between soft silicone and long carbon fibers creates highly heterogeneous systems with a nonlin-

ear behaviour in buckling mode. Manual extrusion was attempted using needless syringes but ultimately failed as the uncured doped polymer proved viscous and subject to clotting.

Figure 2.2 illustrates the mechanical response of several interfaces made with different amounts of NiCCF. This figure shows the residual increase in length after stretch. We can observe that even for a very small amount of NiCCF (0.07% by volume), the residual length after stretch is considerable. Therefore, to minimize this effect we decided to use the smallest amount of NiCCF in our interface.

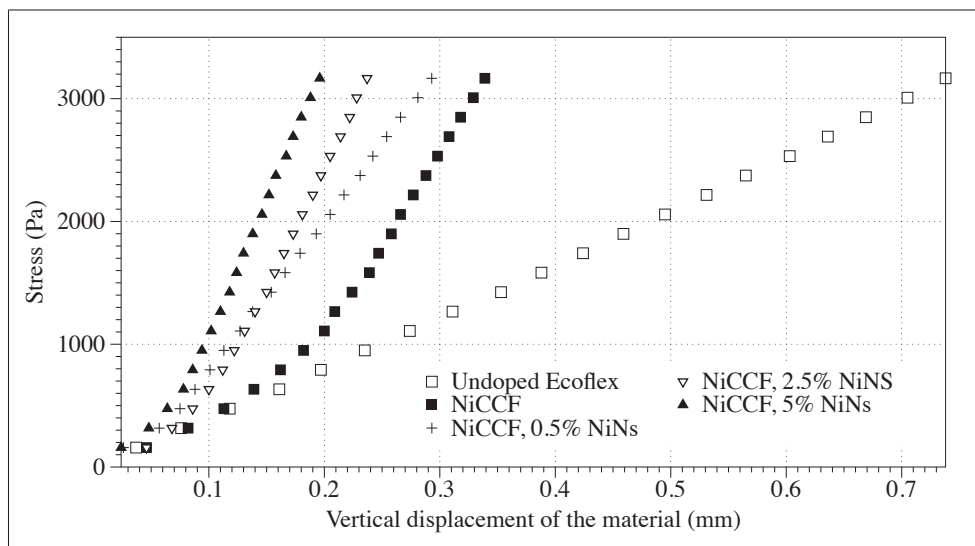


Figure 2.3 Comparison of the mechanical response of doped elastomer (NiNs and 0.07% per vol. NiCCF) and non-doped EcoFlex.

The NiNs particles being significantly smaller than NiCCF particles, they do not contribute noticeably to mechanical hysteresis in the composite. However, the amount of NiNs that is required to form enough effective conductive pathways through the silicone is higher than with NiCCF. Typically, increasing the volume ratio of filler in a composite will also increase the compressive strength of the resulting material (Fang *et al.* (2009)).

Figure 2.3 shows how the compressive strength of our silicone composite increases with the amount of NiNs used. In order to keep the properties of our sensor as homogeneous as possible,

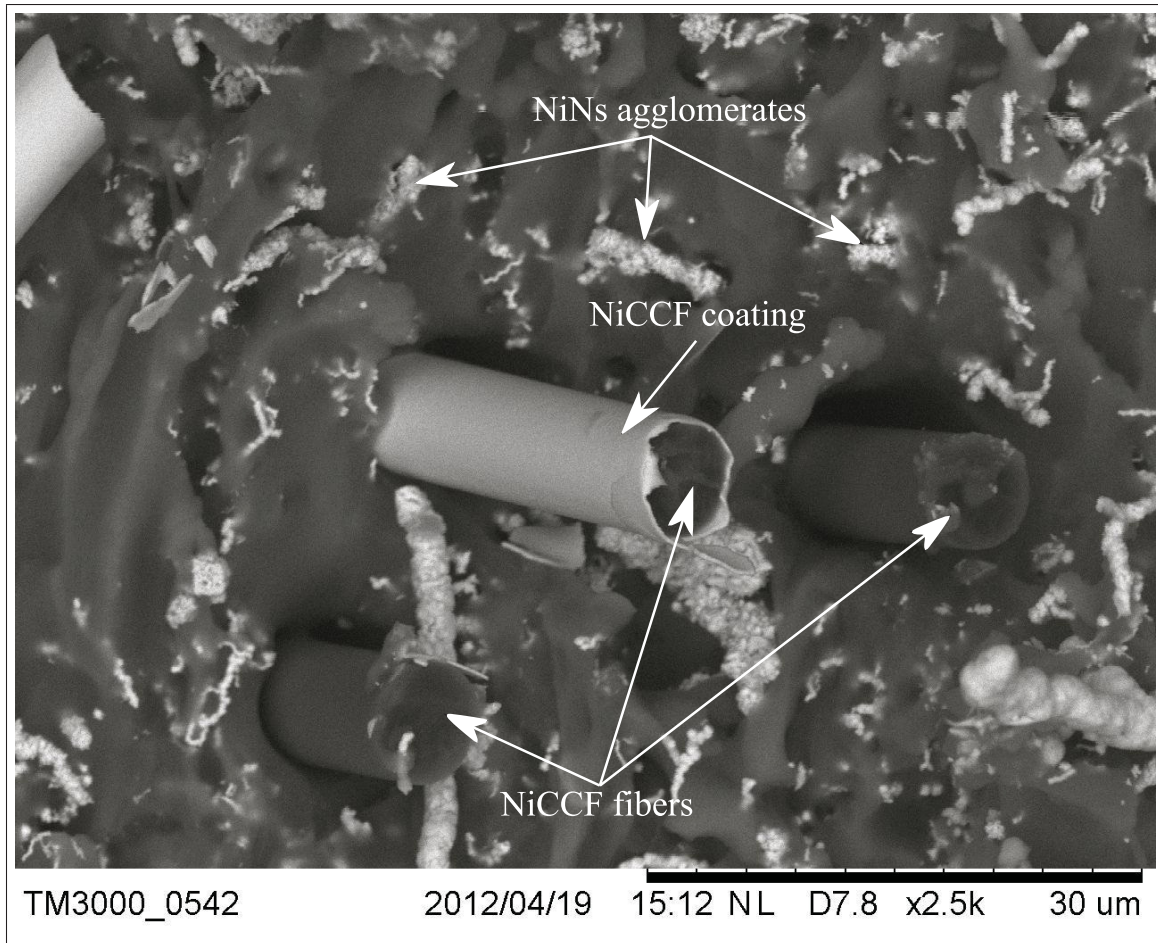


Figure 2.4 Scanning electron microscope image at 2500X of the silicone nanocomposite used for the conductive interfaces of the soft strain sensor.

conductive interfaces with a high compressive strength should be avoided. Hence, the final NiNs and NiCCF proportion used in our interfaces was chosen as a trade-off between the two above undesired effects: the chosen mixture contained 4% NiNs and 0.09% (length $800\mu\text{m}$) NiCCF by volume.

The measured resistivity was $80 \Omega \cdot \text{cm}$, which was much greater than eGaIn, but negligible compared to that of the ionic solution (Cheung *et al.* (2008)). The interaction between the two different particle types is apparent in the scanning electron microscopy image shown in Figure 2.4.

2.1.3 Electrical interface

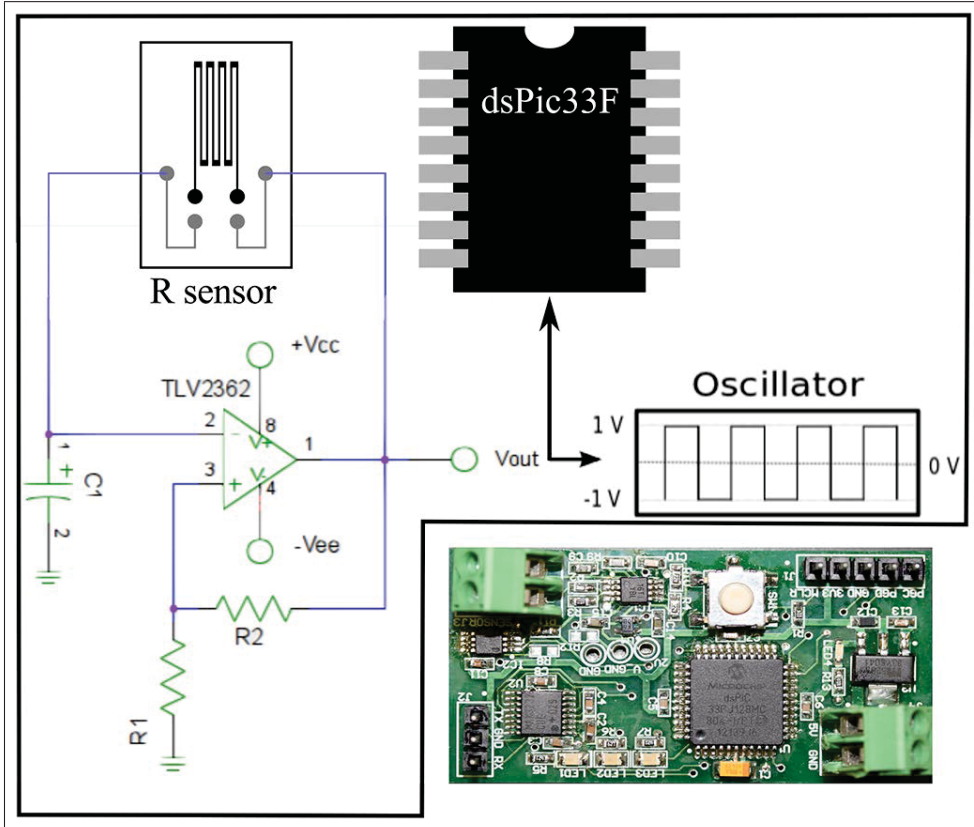


Figure 2.5 Soft strain sensor circuit design and resulting PCB

At voltages above 1.23 V, electrolysis of water divides molecules to produce hydrogen and oxygen gas. Thus, we designed a relaxation oscillator circuit using a low-voltage operational amplifier (TLV 2362, Texas Instruments) in order to obtain an integrated low-voltage AC circuit.

This simple circuit, schematized in Fig 2.5, measures the resistance change of the sensor and has the advantage of using a DC supply to generate a -1 V to 1 V oscillation where the pulse length is a linear function of the sensor resistance, according to the following equation:

$$T = 2R_s C_1 \ln \frac{1+B}{1-B}, \quad (2.1)$$

where R_s is the resistance of the sensor, C_1 is the oscillator capacitance, with sensor's capacitance being negligible in comparison, and B is a function of resistances R_1 and R_2 , specifically,

$$B = \frac{R_1}{R_1 + R_2}. \quad (2.2)$$

As the sensor is stretched, the resistance of the ionic solution will increase and the frequency of the resulting oscillation will decrease. Previous characterization of the dependence of the impedance of the ionic solution on frequency (McAdams *et al.* (1995); Cheung *et al.* (2008)) shows that the frequency of the AC signal can be a major influence on the flow of ions and thus on the real part of the impedance.

Direct current (or an extremely low frequency) will cause electrolysis and polarize the electrodes. At the other extreme, an extremely high frequency will increase the conductivity of the solution by the Debye-Falkenhagen effect (Harris & O'Konski (1957)). As previously shown, at frequencies between 40 Hz and 10 MHz, the real part of the impedance will slowly decrease in a predictable way (Cheung *et al.* (2008)).

The dependence of the resistance of the ionic solution on frequency will have an impact on eq. (2.1) as the relationship becomes coupled. Not only does resistance have an impact on oscillation frequency, oscillation frequency has an impact on resistance. Therefore, eq. (2.1) can be rewritten as follows:

$$T = 2R_s(f)C_1 \ln \frac{1+B}{1-B}. \quad (2.3)$$

This equation is no longer linear, which has the effect of increasing the perceived gauge factor. To maximize this coupling effect, the components C_1 , R_1 and R_2 in the circuit were chosen such that the oscillation frequency at the sensor nominal resistance was around 600 Hz, following the analysis of the data presented in (McAdams *et al.* (1995); Ferrara *et al.* (2000); Cheung *et al.* (2008)).

The oscillation frequency is measured using a counter input of a digital signal processor (dsPIC33F, Microchip Technology). Figure 2.5 shows a schematic of the oscillator circuit and the completed PCB.

2.2 Fabrication

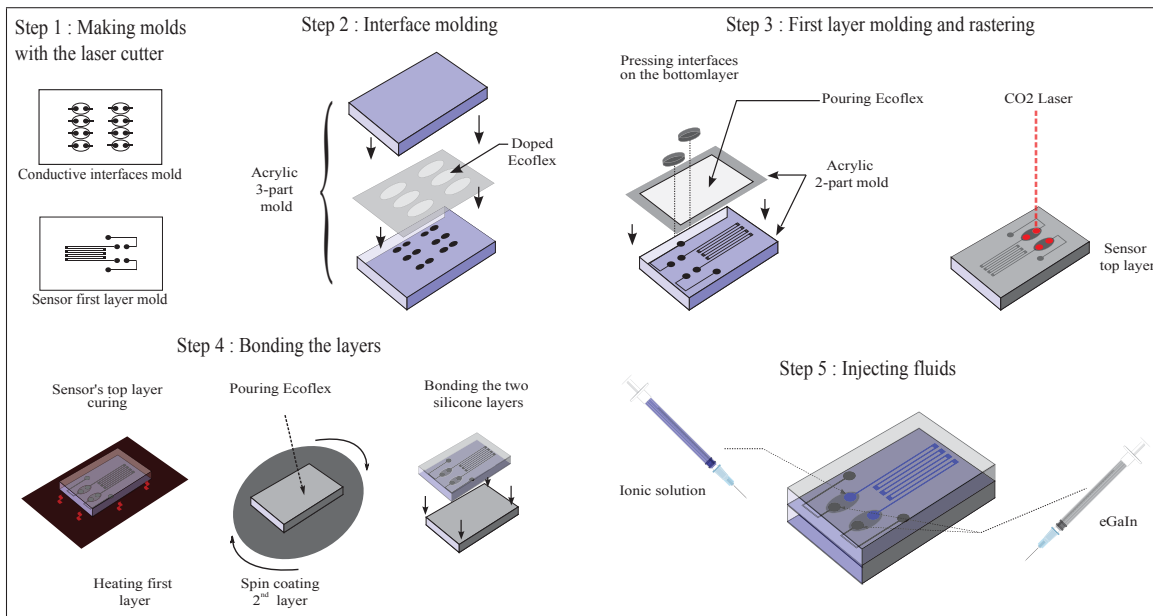


Figure 2.6 Soft strain sensor fabrication and assembly procedure.

The sensor was fabricated according to the procedure illustrated in Figure 2.6. Three acrylic molds were engraved in *Stucki* mode² using a CO₂ laser cutter (Epilog Helix 40 Watts): one for casting the conductive interfaces, another for the sensor layer with microchannels and the last for the top layer.

The laser allow us to make channel widths varying from 200 to 550 μm (from top to bottom). By controlling the power and speed of the laser, channel depth could also be controlled. The present prototype is 2 mm thick with channel depth of 600 μm . Figure 2.7 shows a close-up

² The *Stucki* algorithm is a graphical dithering technique, aiming at reducing the quantisation error by averaging each pixel's depth with the neighbouring pixels of the image. Laser engraving using this algorithm leads to a better surface finish (Stucki (1992)).

view of the resulting mold with the microchannel pattern, including channel dimensions. This figure also shows that the laser produces non-square (trapezoidal) channel geometry.

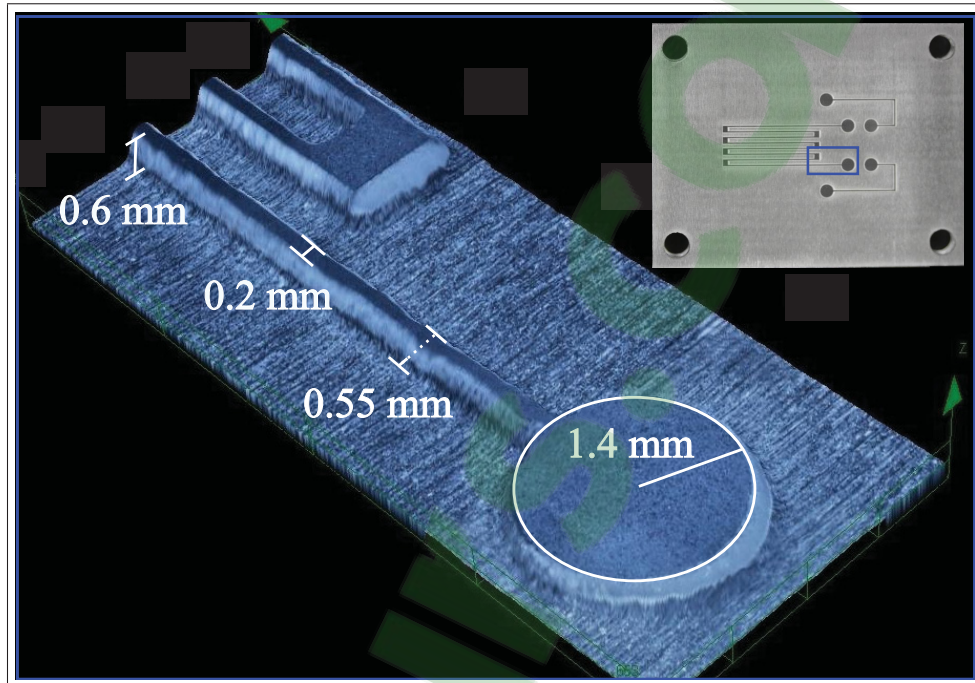


Figure 2.7 Acrylic mold and features dimensions. By rastering the mold extraneous surfaces in Stucki mode, the laser uncovers the mold features.

As mentioned above, the base material of the conductive interface is a platinum cure silicone (EcoFlex, Smooth-On) with a very low Shore hardness (00-30). The conductive nano and micro particles, NiNs (4% by volume) and NiCCF (0.09% by volume) were embedded into the elastomer by mixing for three minutes in the planetary mixer. The resulting composite was degassed in a vacuum chamber, poured into the clean mold, and cured for 25 minutes in an oven at 65°C.

The cured conductive interfaces were placed in their positions in the sensor mold and additional EcoFlex was poured to form the portion of the sensor that contains the microchannels. After 30 minutes of curing at 65°C, the CO₂ laser was used at low power (30% of maximum speed, 22% of maximum power) to micro-machine the interfaces in order to remove the poorly conducting

elastomer layer formed during curing and thereby expose the nanoparticles on the surfaces that will contact the fluids. This did not affect the nickel particles, since the laser wavelength ($10.6 \mu\text{m}$) was too long to be absorbed by this metal (Chen *et al.* (1996)).

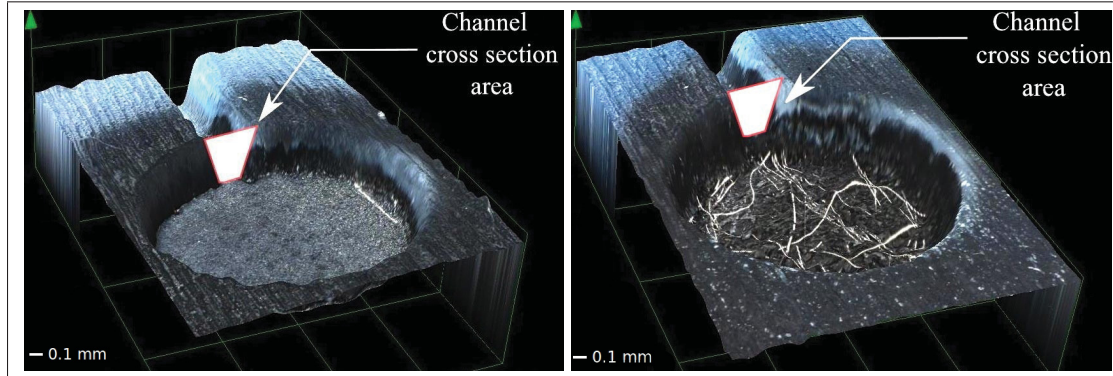


Figure 2.8 3-D images of the sensor composite interface taken with an opto-digital microscope a) before micro-machining and b) after micro-machining.

The resistance of the resulting interface was as low as 30Ω throughout its entire length (4 mm). It was found that the resistance could be decreased by at least one order of magnitude by micro-machining the top of the interfaces, and that repeatability was increased as a result of different interfaces having much closer nominal resistances. Figure 2.8 shows the interface material before and after laser treatment.

The top layer that covers the microchannels was then cast and bonded to the cured bottom layer. Since silicone elastomer is extremely hydrophobic, bonding two layers can be difficult. Although oxygen plasma bonding (Zucker *et al.* (1993)) is often used to bond Polydimethylsiloxane (PDMS), attempts to bond Ecoflex using this method were unsuccessful.

To achieve good bonding, the patterned layer was kept in the oven at 65°C , while the top layer was spin-coated with Ecoflex at low speed (350 rpm), and then for the last 20 seconds at a greater speed (1600 rpm) spreading the Ecoflex as a flat, uniform and very thin layer. Ecoflex thin layers, in addition with the use of a pre-heated patterned layer, allows for faster curing and prevents the sensor channels to be filled by curing polymer, as shown in previous work (Park

et al. (2012a)). The heated layer was then carefully placed on the spin-coated layer, and the assembly was deposited in the oven for 15 minutes at 65°C.

The final steps consisted of filling the microchannels with eGaIn and saline solution using syringes fitted with a hypodermic needle (one for injecting the liquid and another for withdrawing captured air at the other end of the channel). Small wires are inserted at the end of the eGaIn channels. Ecoflex is then spread in small amounts around the connection point, thus sealing the holes left by the needles and attaching the wires that link the sensor to the PCB. The sensor is finally cured at room temperature.

2.3 Results

In order to test the robustness of our design, in particular the effectiveness of our conductive interface at eliminating electrode polarization and electrolysis, the sensor was first connected to the circuit shown in Figure 2.5 and stimulated with AC current for over 100 hours. No bubble formation or change in resistance was observed in the sensor. In comparison, a single hour under 3V DC was sufficient to cause bubble formation in an earlier prototype and render the device non-conductive.

However, after long term storage at room temperature of the sensor (weeks), some evaporation of the water contained in the ionic solution was noted. This change created a proportional small drift of the resistance of the ionic solution channel, although it did not change the overall behaviour of the sensor.

There could be many sources for this evaporation such as an imperfect bonding between the sensor layers or an imperfect closure of the syringe's holes. Although we didn't find any information regarding the gas permeability of Ecoflex, the permeability of this silicone is another source that could be responsible for these losses.

ILs have been proposed in comparable situation to overcome this effect as they are both conductive and have very low volatility (Zhu *et al.* (2009); Noda *et al.* (2010); Wu *et al.* (2011)) and are investigated for further stability of the sensor.

In addition to the liquid evaporation, silicone elastomer polymers mechanical properties are known to change as the material ages. Although no tests were devised to measure this particular aspect, our sentiment is that designing soft sensors whose strains requires very small forces when compared to the expected actuation forces renders that aspect of the aging process mostly negligible.

Stress was also applied to the eGaIn channels to verify that the sensor was sensitive only to stretching of the portion containing the saline-solution-filled microchannels. Neither stretching nor pressure applied to the eGaIn channels produced any significant change in the overall sensor resistance, up to the point at which these channels were pinched and rendered non conductive.

Following these qualitative experiments, the sensor was mounted on a force test stand (Mark-10 ES20,) equipped with a force and a displacement gauge (Mark-10 M4-10 and Mitutoyo 543-693, respectively) to measure the relationship between resistance and strain (see Figure 2.9). The resistance variation of the sensor was monitored with a LCR meter (B&K Precision 878B) at a frequency of 1KHz. The purpose of this test was to characterize the sensor response and verify the gauge factor as well as compare it to a theoretical model.

To model the change in the resistance of our sensor under strain, we had to consider the resistance of the solution as well as the effect of the geometry. The electrical resistance R of a channel filled with an ionic solution is known to follow the relationship defined by the following equation:

$$R = \rho \frac{L}{A}, \quad (2.4)$$

where ρ is the resistivity of the ionic solution, A the smallest cross-sectional area of the channel, and L is the length of the microchannel. Assuming incompressibility, the ionic solution can be

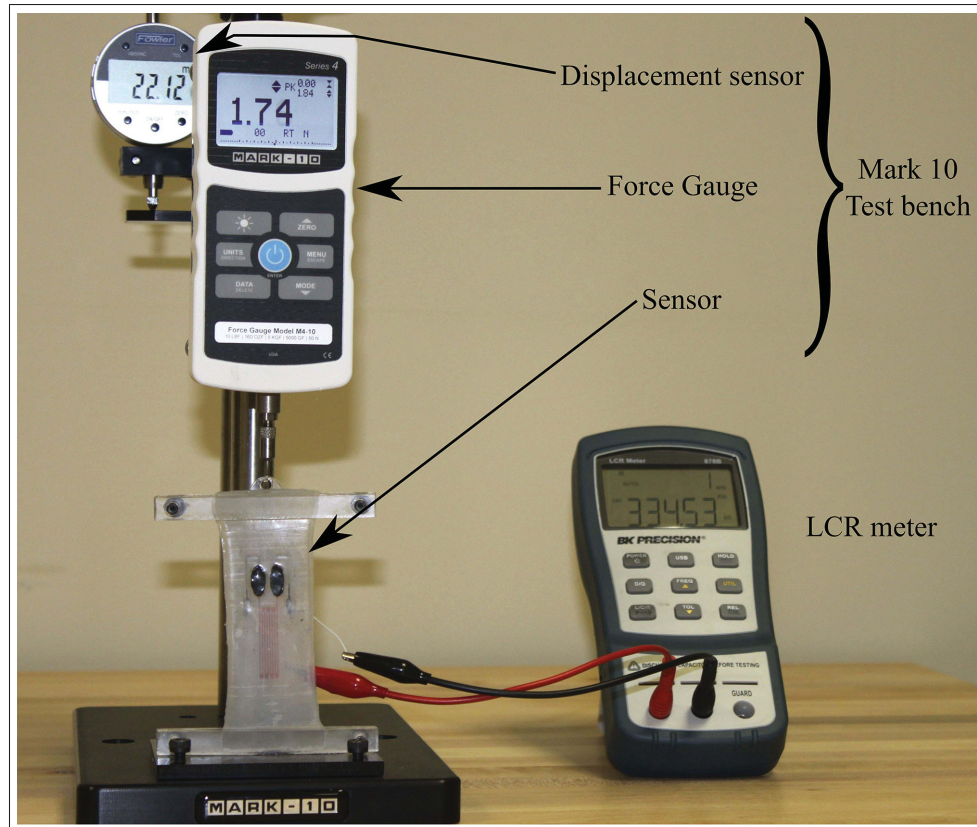


Figure 2.9 Soft strain sensor test setup.

modeled as a liquid with constant specific resistance ρ . The value of ρ was calculated using the measured initial sensor dimensions (L and A) and the initial resistance at 1 KHz.

The specific resistance being constant, the variation in the resistance of the sensor is due solely to the change in the dimension L and the cross-sectional area A . As shown in Figure 2.8, the channel cross-section is trapezoidal. The area of an isosceles trapezoid is calculated using the following equation:

$$A = h \frac{a+b}{2}, \quad (2.5)$$

where h is the trapezoid height, and a and b are, respectively, the top and bottom widths of the channels. Measurements made with an opto-digital microscope (Olympus DSX100) show that the channel initial height h_0 was 0.6 mm and that the maximal and minimal initial widths were

$a_0 = 0.55$ mm and $b_0 = 0.2$ mm, respectively. The initial channel length L_0 was designed to be 160 mm.

The length of the sensor channels subject to a strain $\varepsilon = \frac{\Delta L}{L_0}$ is expressed as follows:

$$L = L_0 + \Delta L = L_0(1 + \varepsilon). \quad (2.6)$$

In response to this stretching, the cross-sectional area A of a channel will decrease as follows:

$$A = (h_0 + \Delta h) \frac{\{(a_0 + \Delta a) + (b_0 + \Delta b)\}}{2}. \quad (2.7)$$

Using the relation defining transversal and axial strains, Δh , Δa and Δb can be, replaced, respectively by $-\nu\varepsilon h_0$, $-\nu\varepsilon a_0$ and $-\nu\varepsilon b_0$, where ν is the Poisson's ratio of the material. By substituting these expressions into eq. (2.7), the relationship between the applied strain and the channel cross-sectional area can be expressed as follows:

$$A = \frac{h_0(a_0 + b_0)(1 - \nu\varepsilon)^2}{2}. \quad (2.8)$$

Substituting eqs. (2.6) and (2.8) into eq. (2.4), the resistance of the sensor for applied strain becomes

$$R_s = \frac{2L_0\rho(1 + \varepsilon)}{h_0(a_0 + b_0)(1 - \nu\varepsilon)^2}. \quad (2.9)$$

It should be noted that the mechanical property of the resulting sensor is anisotropic due to the presence of channels filled with fluids and doped polymer interfaces. Therefore, the conventional value of 0.5 for the Poisson's ratio of an elastomeric material is not applicable. This ratio was instead calculated using experimental measurements of the cross sectional area at different strains under a microscope. The Poisson's ratio ν determined experimentally for our sensor was 0.39.

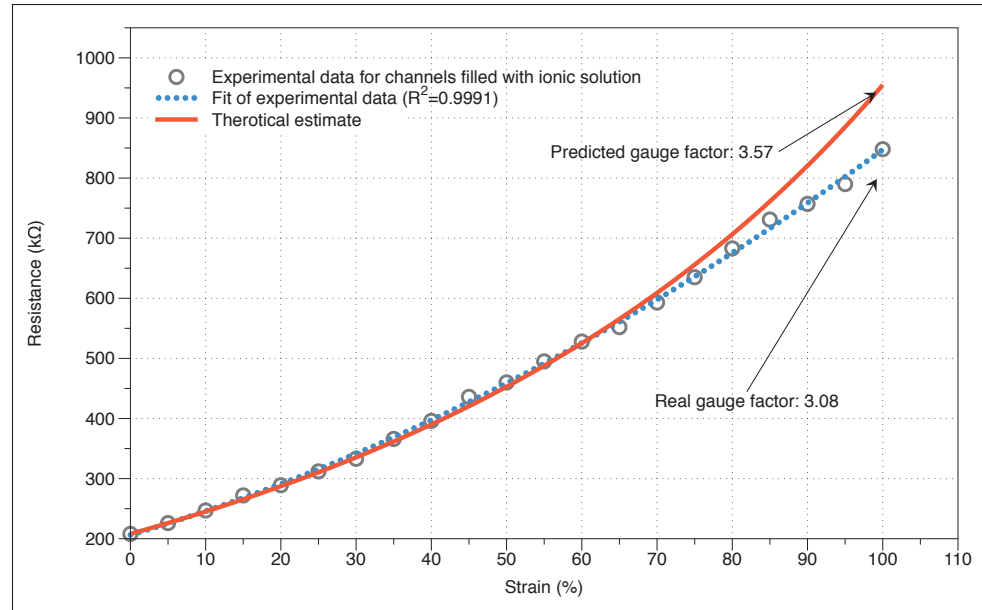


Figure 2.10 Resistance variation as a function of strain for the ionic solution sensor.

2.3.1 Sensor resistance variation under strain

Figure 2.10 shows the measured resistance as a function of strain as well as the theoretical curve obtained with the model. It is noted that for strain less than 70%, the model appears to match the experimental data almost perfectly. The less pronounced slope of the experimental curve for the portion above 70% leads to a smaller gauge factor (3.08) than what was anticipated based on the model (3.57).

2.3.2 Comparison with eGaIn

Although the main motivation for the hybrid (ionic solution/eGaIn) approach was to decouple the sensing portion from the signal routing channels in order to make the sensor less sensitive to stress on the signal-carrying portions, we also wished to verify the impact of replacing eGaIn with saline solution on the sensor response. We therefore filled a sensor entirely with eGaIn and measured its strain response using the same test setup.

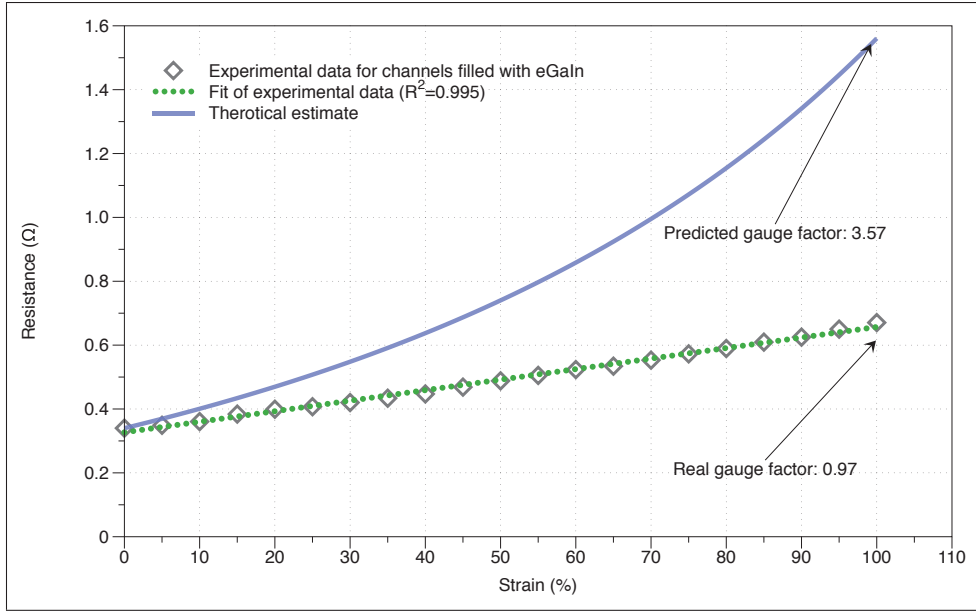


Figure 2.11 Resistance variation as a function of strain for the eGaIn sensor.

Figure 2.11 shows the measured resistance of the eGaIn sensor, as well as the theoretical curve given by the model represented by eq. (2.9). The experimental curve differs considerably from the theoretical prediction. In fact, instead of the expected nearly quadratic function, we obtained a quasi-linear relation that follows the change in channel length quite precisely:

$$R_s \approx kL_0(1 + \varepsilon), \quad (2.10)$$

where k is a constant defined as $\frac{\rho}{A_0}$. This has the effect of lowering the gauge factor of the eGaIn-filled sensor to a considerable extent (0.97 instead of 3.57 theoretically at $\varepsilon = 1$).

Figure 2.12 shows the measured normalized change in resistance versus applied strain for the ionic solution sensor and for the the eGaIn only sensor. It is noted that the gauge factor is more than three times (3.17 times) greater for the ionic solution sensor.

The gauge factor G of a sensor for a given temperature is given by $G = \Delta R/R_0\varepsilon$, where ΔR is the sensor change of resistance, R_0 is initial resistance and ε the strain. Using eqs. (2.9)

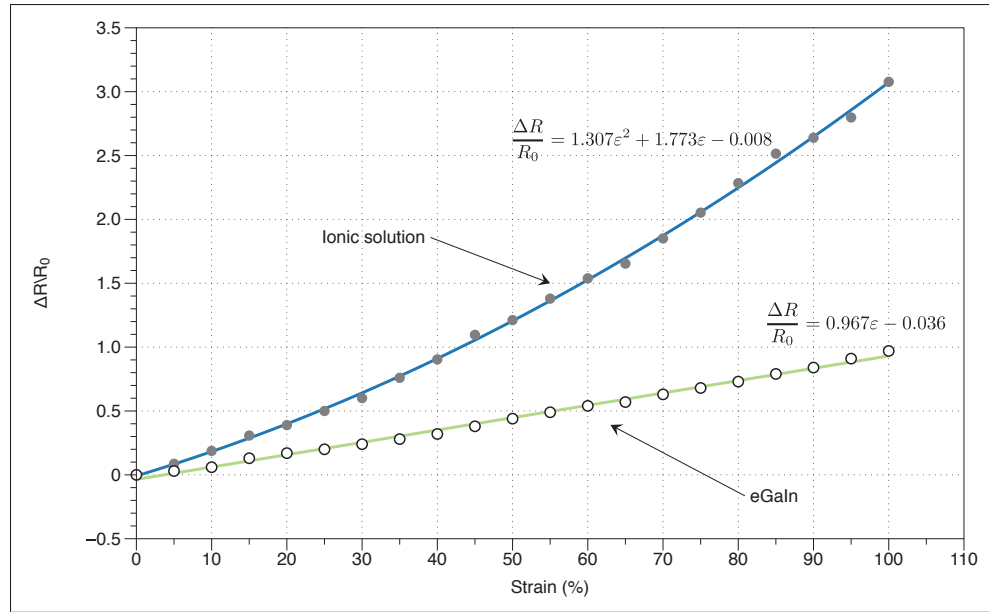


Figure 2.12 Normalized change in resistance as a function of strain for saline-filled and eGaIn-filled soft strain sensors.

and (2.4), the gauge factors of our sensor is :

$$G = \frac{1 + \varepsilon - (1 - \nu\varepsilon)^2}{\varepsilon(1 - \nu\varepsilon)^2}. \quad (2.11)$$

According to this equation, the gauge factor is a function only of the strain and the Poisson's ratio and therefore should be the same no matter what conductive fluid is used.

Our hypothesis to explain this discrepancy is that the surface tension of the oxidized skin of eGaIn prevents this non-Newtonian liquid from forming the exact shape of the channel. This surface tension is known to be very high (Dickey *et al.* (2008)). Therefore, up to a certain critical stress and channel cross-sectional area, it is possible that the effective area of the liquid therefore remains constant.

Observations made at higher strains than presented in these graphs support this explanation. Beyond a strain of 130%, the curve loses its linearity and acquires the characteristic of a quadratic system in which the channel length and the cross-sectional area both change. The

sensors were stretched up to 200% of their initial length without mechanical failure, however the sensor very high impedance made the strain value very hard to experimentally measure.

2.3.3 Frequency dependency of the sensor impedance

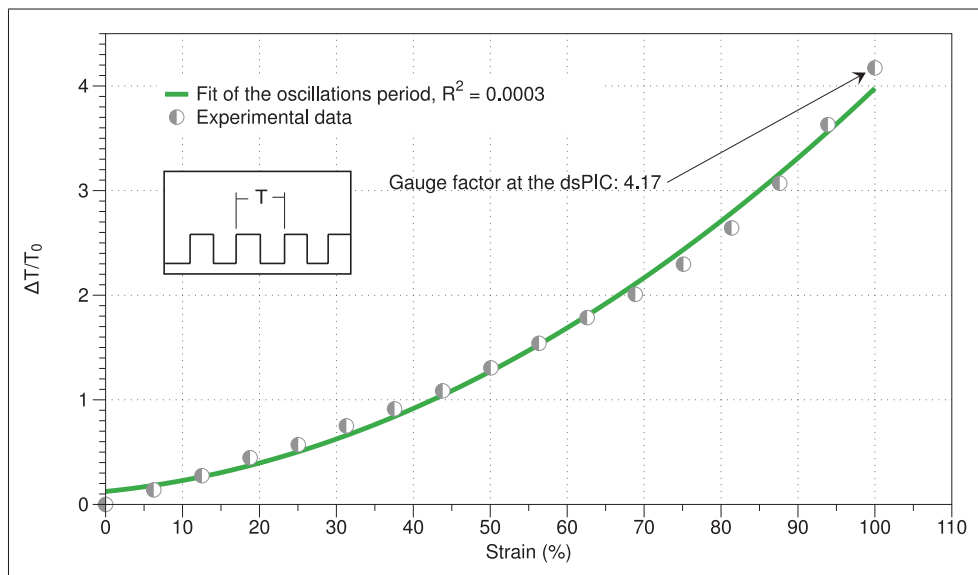


Figure 2.13 Normalized change in the oscillation period as a function of strain for the sensor filled with ionic solution.

One other point to validate was the frequency dependency of the sensor impedance on the perceived gauge factor at the micro-controller. As mentioned in section 2.1.3, the resistance of an ionic solution is a function of the frequency of the AC input at the electrodes.

The circuit used to power the sensor and measure its response is a low-voltage op-amp that oscillates at a frequency that is a function of sensor resistance, based on eq. (2.3). This generates coupling that will increase the perceived gauge factor.

To validate this hypothesis, the sensor filled with ionic solution was tested using the apparatus shown in Figure 2.9 but connected this time to the circuit shown previously in Figure 2.5.

Since the resistance will be measured in terms of the duration of an oscillation rather than by reading a voltage we recorded the normalized change in the period of the oscillation as a function of the strain applied to the sensor in order to calculate the gauge factor at the micro-controller (see Figure 2.13).

As anticipated, the coupling in our circuit increased the gauge factor of the sensor (from 3.08 to 4.17) compared to when its resistance was measured at a fixed frequency.

2.3.4 Sensor stiffness

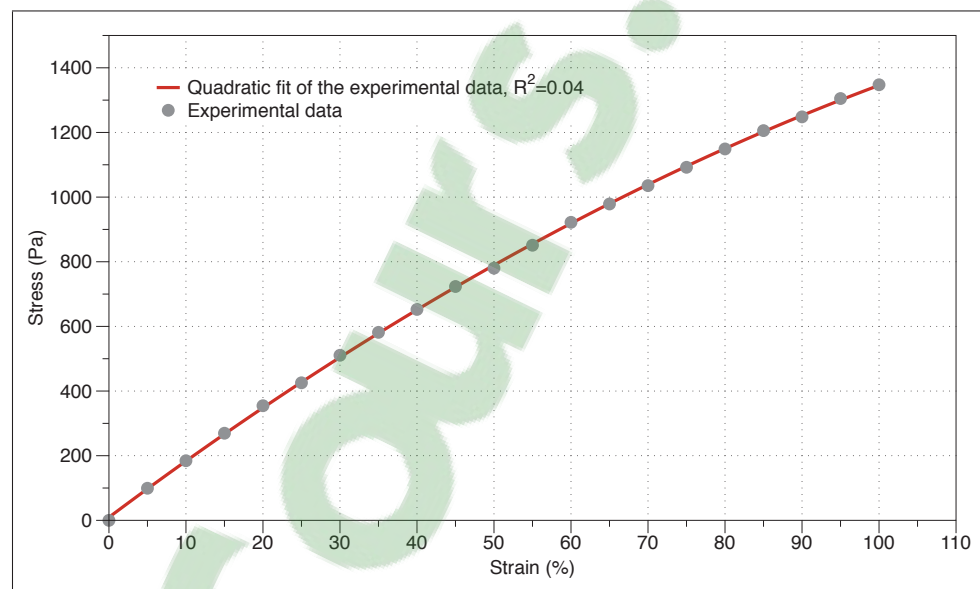


Figure 2.14 Stress-strain relationship of the soft strain sensor.

Finally, since our sensor was designed for the purpose of measuring motion associated with the phalanges of a prosthetic hand, the stiffness of the material should not interfere with its movement. Indeed, a high stiffness could impede the grasp motion of the prosthetic hand.

Figure 2.14 shows the strain versus pulling force response of the sensor. Although the stiffness appears non-linear, it is very predictable. Preliminary tests suggested that in the context of our application the maximum strain that our sensor will undergo is around $\epsilon = 10\%$. According to

Figure 2.14 and Fig 1.2, and using the relationship $stress = \frac{F}{A}$, reaching this strain requires only a few millinewtons, which is significantly below typical prehension forces (Dargahi & Najarian (2005)).

Mechanical failure over a large number of cycles was not investigated. The silicone elastomer (Ecoflex 00-30, Smooth-On) having a very large elongation at break (900%) we do not expect it to fail given the comparatively low strains it is being subjected to, even over a large number of cycles. The most critical aspect of the sensor in respect to a large number of cycles is the connection between the conductive and soft eGaIn channels and external conventional electronics. Because of the differences in hardness, delamination or break may occur. To remedy to this issue, an ideal soft sensor may either:

- Progressively increase in hardness as it connects with conventional electronics, in order to share the strain over large areas instead having it focused on local boundaries between materials;
- Use completely soft electronics.

Finally, although the effect of temperature was not studied, we expect it to have an impact on the sensor measures as it is widely known that ionic conductivity increases with temperature. Calibration of the sensor for different temperatures in combination with temperature tracking using conventional electronic components should allow for accurate strain measurements over a large range of temperatures.

CHAPTER 3

SOFT MICROFLUIDIC SENSITIVE SKIN

*Good men, the last wave by, crying how bright
Their frail deeds might have danced in a green bay,
Rage, rage against the dying of the light.*

*Wild men who caught and sang the sun in flight,
And learn, too late, they grieved it on its way,
Do not go gentle into that good night.*

Dylan Thomas

Expanding on the research presented in Chapter 2, this chapter's aim was to generalize previous work by creating multiple interconnected channels. We designed a matrix-type soft sensor made of silicone elastomer with embedded microchannels filled with an RTIL.

This Chapter describes the novel design and manufacturing processes of the proposed sensing skin, as well as the image reconstruction algorithm used to detect contact location and pressure without adding internal wiring.

3.1 Tomographic imaging and ionic liquid microchannel embedded silicone sensor

Tomographic imaging is a widely used technology in medical fields since it can provide relatively precise images of inside of a human body in a non-invasive and radiation-free way. By definition, tomographic imaging is based on the inverse reconstruction of cross-sectional images from measurements made at boundaries. Different types of measurement methods may be used depending on applications.

For example, X-ray computed tomography (X-ray CT) measures X-rays going from the the X-ray source to the X-ray sensors through the patient's body while EIT measures electrical

potentials of multiple measurement electrodes when an electrical current was injected through the body (see Figure 3.1).

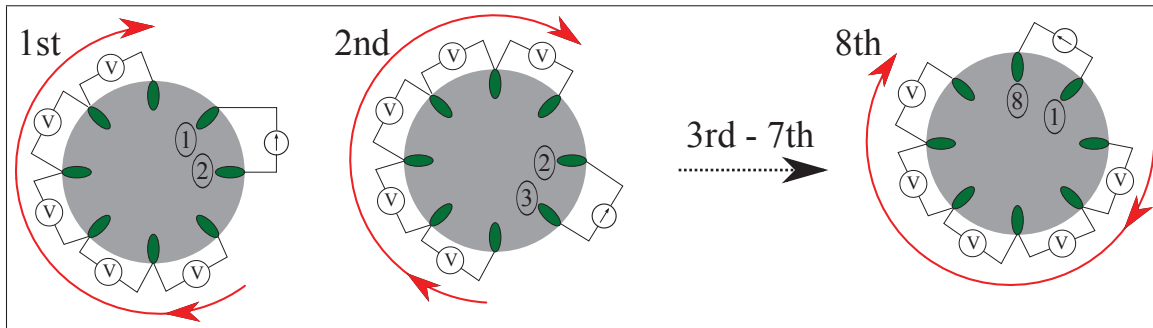


Figure 3.1 Example of a typical EIT acquisition protocol with 8 electrodes. EIT requires 8 consecutive current injection electrode pairs and 48 distinct voltage measurements.

The difference is that X-rays, unlike electrical currents, pass through the body in a straight line. In the case of EIT, electrical current paths are dependent on the internal conductivity of the medium and will cover the full conductive surface (Nagakubo *et al.* (2007); Kato *et al.* (2007)). The mathematical reconstruction of EIT is thus often described as a complex and severely ill-posed problem.

The main advantage of using EIT to reconstruct the stress patterns within a piezoresistive sheet is that electrical connections only at the edges of the material is sufficient. Conductive rubber sheets generally consist of polymer matrices blended with conductive nanoparticles or microparticles.

In this type of materials, electric current flows through conductive chains as a result of the quantum tunneling effect (Hu *et al.* (2008)). As shown in Figure 3.2, unlike with bulk metal conductors, the current in a piezoresistive composite does not necessarily flow through the straight line (the shortest path) between two electrodes but rather follows the principal chains of conductive particles, which may form an arbitrary path within the rubber sheet.

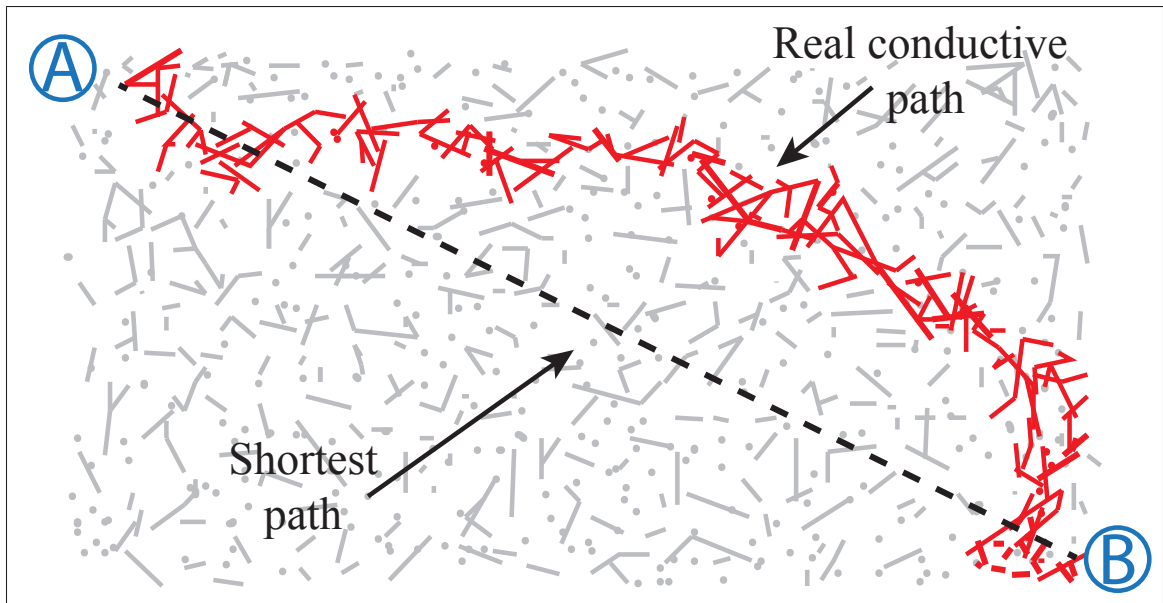


Figure 3.2 Possible conductive chain path in a piezoresistive composite.

This means that a stress applied to a point at a considerable distance from the shortest geometric path between two electrodes could change the sensor impedance more than a stress applied to a point on this line, resulting in a compromised accuracy of the contact location.

In order to solve this problem, we propose use of a silicone sheet containing a network of microchannels filled with an ionic liquid, as shown in Figure 3.3. Ionic liquids, also called molten salts, are salts in a liquid state, and unlike ionic solutions, are composed only of ions.

By selecting anions and cations, it is theoretically possible to create 10^{18} different ionic liquids (Visser *et al.* (2009)). Some of these have melting points below room temperature, acquiring the name room temperature ionic liquids. This property is mainly due to the charge distribution of the ions as well as their symmetry and hydrogen bonding ability (Marsh *et al.* (2004)).

Depending on the ions used, the material properties of RTILs can be tailored with specific applications. RTILs in industry are generally considered as a "green" alternative to conventional solvents or electrolytes (Marsh *et al.* (2004)) because of their high ionic conductivity and non-volatility (Visser *et al.* (2009)). These characteristics also make them suitable for use in silicone sensors (Zhu *et al.* (2009); Noda *et al.* (2010)).

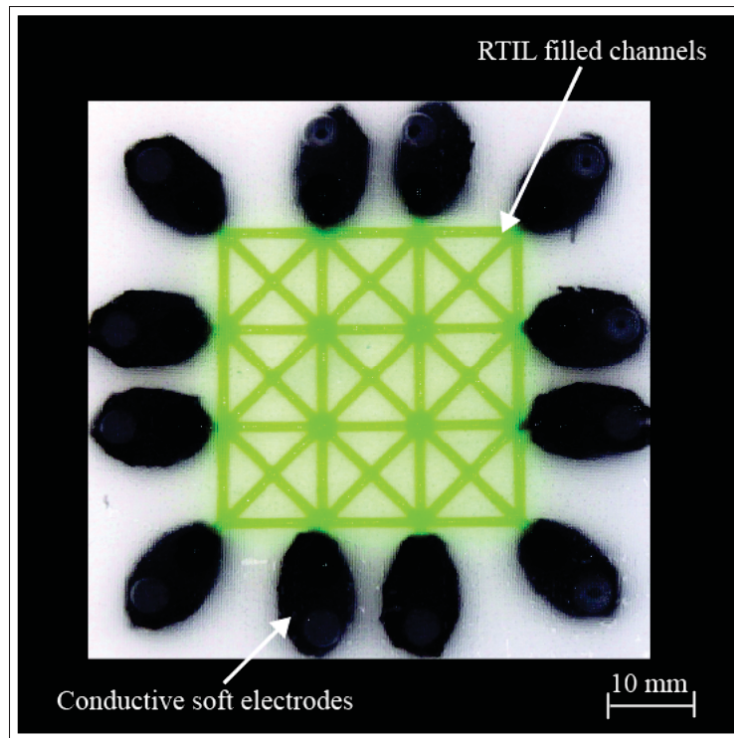


Figure 3.3 Complete skin sensor prototype. Green lines are microchannels filled with RTIL, and black ellipses are conductive polymer patches as electrical interfaces to measurement electrodes.

Since silicone is gas-permeable, bubbles can form in the channels of sensors containing ionic solutions as changes in temperature increase then decrease the hydrosolubility of atmospheric gases. Water itself forms vapor as temperature increases. Avoiding the presence of water altogether is preferable.

No general theoretical model is available to predict the properties of RTILs, thus information is largely collected through experimental measurements. The RTIL (1-ethyl-3-methylimidazolium ethyl sulfate, EMISE, Sigma-Aldrich/BASF, $\geq 95\%$ purity) used in our sensor prototype has a melting point of -30°C (ChemSpider (2014)). Previous research has reported that this RTIL has negligible vapor pressure and is chemically stable with contacts with both air and water (Zuo *et al.* (2010)).

Another advantage of using RTIL as a conductive medium into a resistive based artificial skin is that its sensitivity will remain stable over time (Visser *et al.* (2009)). While the overall resistivity of a piezoresistive rubber is known to increase greatly with the aging of the silicone matrix (Ying *et al.* (2007)), the resistivity of an RTIL is not affected by time (Visser *et al.* (2009)).

ILs are also preferred to liquid metals (e.g. eGaIn, $\rho = 29.4 \times 10^{-4} \Omega \cdot m$, Dickey *et al.* (2008)) due to their higher resistivity ($\rho = 2.5 \Omega \cdot m$), thus maximizing the variation in absolute resistance and minimizing the impact of random variations at the interface between solid and liquid.

As it is well known that the conductivity of a channel filled with conductive liquids is a function of only the length between the two electrodes and the area of the channel cross-section, the electrical resistance between two points is thus easily predicted.

3.2 Design and fabrication

3.2.1 Sensor base layer and soft electrodes

Our sensor was made of an extremely soft platinum-cured silicone called Ecoflex (Smooth-On, shore 00-30) following the manufacturing process presented in Figure 3.4.

A mold was first machined from an acrylic sheet using an Epilog Helix 40-Watt CO₂ laser cutter at 20 % speed and 30 % power. This mold bore features that produced channels of which the cross-section was trapezoidal, measuring 350 μm in depth, 650 μm at the bottom and 1300 μm at the top.

Larger channels than reported in Chapter 2 were preferred in order to increase the channel volume fraction of the resulting sensor. The mold is shown in Figure 3.5.

In order to avoid leakage of the ionic liquids from the sensor due to movement of metal probes, we used the same silicone-based electrodes than in Chapter 2, containing a mixture of

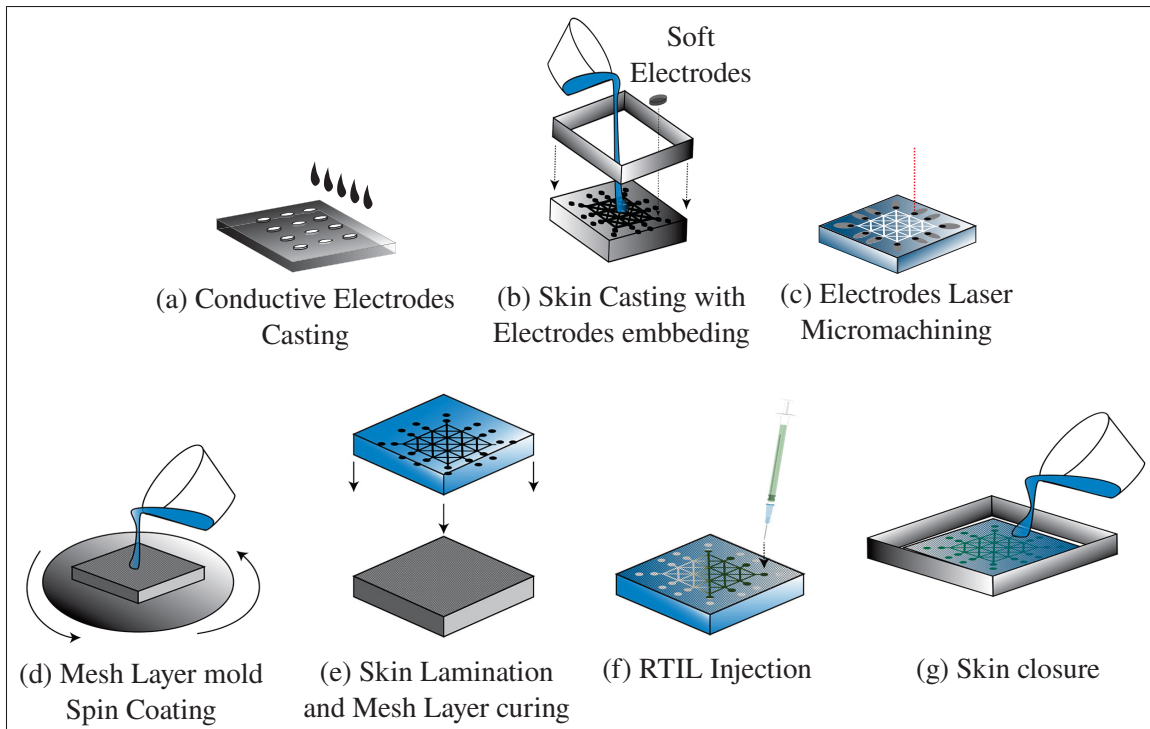


Figure 3.4 Skin manufacturing process. (a) Cast soft electrodes using a mixture of nickel strands and carbon fibers with liquid silicone. (b) Pour liquid silicone to cast a base sensor layer with a microchannel pattern and embed electrodes. (c) Micromachine electrodes for increased conductivity using low-power laser. (d) Spin coat liquid silicone on a mesh layer mold. (e) Laminate the base layer on the uncured mesh layer for bonding. (f) Remove the mesh-bonded base layer from the mold and inject an RTIL. (g) Pour another silicone layer for top mesh sealing.

high-aspect-ratio nickel strands (NiNs) and nickel-coated micron-sized carbon fibers (NiCCF). Nickel is highly conductive, affordable, slow to oxidize, and hence suitable for our application.

As presented before, this mixture provided very good conductivity with minimal impact on the mechanical properties of the silicone elastomer (e.g. high elongation at break, low hysteresis, and low Young's modulus). It contained 4 % NiNs and 0.09 % NiCCF by volume. The measured resistivity of these conductive interfaces was $8 \times 10^3 \Omega \cdot m$, far below the resistivity of the ionic liquid ($\rho = 2.5 \Omega \cdot m$).

Twelve casted electrodes were placed in the mold described above and Ecoflex silicone was added, degassed and then cured in an oven at 65°C for approximately 25 minutes.

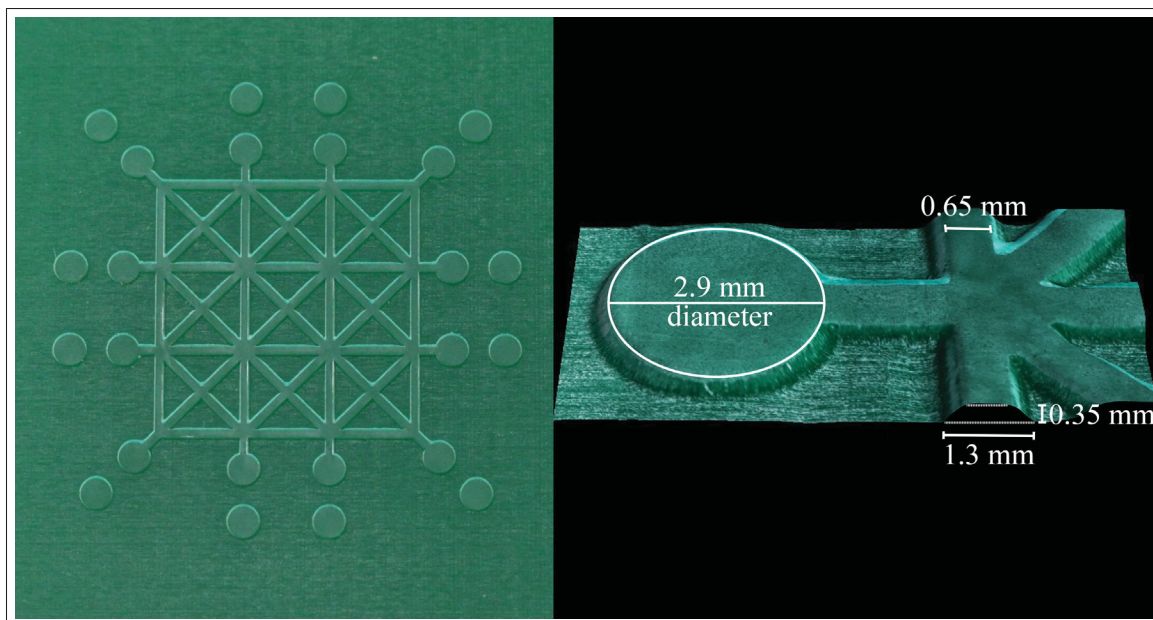


Figure 3.5 Laser cut microchannel mold (left) and its 3-D microscopic view (right) of engraved details.

The cured layer was separated from the mold and the electrode surfaces that come into contact with the RTIL were etched at low power with the CO₂ laser in order to expose the conductive fibers and thus increase greatly the conductivity. The wavelength of a CO₂ laser (10.6 μm) is such that the laser is reflected by nickel and only the silicone is removed.

3.2.2 Injection of RTIL into the sensor

RTIL was injected into the first layer of the sensor. In previous studies, the liquid was injected into the completed assembly, using a needle to vent air from the distal end of each channel (Park *et al.* (2012a); Chossat *et al.* (2013); Kramer *et al.* (2011a)). Although this technique has proven its simplicity and reliability, it allows only one-dimensional filling of a single channel in one direction, and thus cannot be used for multiple interconnected channels.

Indeed, in our case, it is extremely hard to completely fill the sensor array only from one injection point to one suction point, as experience shows that liquids first flow into the most

friction-less path between the two needles, resulting in empty channels in the other areas. Hence, the technique developed should allow a multidirectional filling of the channels.

Furthermore, due to the high surface tension of the liquid, combined with the hydrophobic character of silicone, filling the open channels was not possible either. Besides, the platinum-based catalyst used to cure Ecoflex is very sensitive to extraneous chemical agents, and any contact between RTIL and subsequently applied liquid silicone would inhibit curing and cause defects in the skin.

As an alternative, electrowetting (Lee *et al.* (2002)) of the bottom surface of the channels has been investigated as a means of guiding the flow of ionic liquid into the sensor skin. However, ionic liquids are less compliant than other liquids with electrowetting (Dubois *et al.* (2006)). Our tests showed that the required electric field was strong enough to cause dielectric breakdown of the silicone. Freezing the liquid before curing the silicone (Fassler & Majidi (2013)) was not practical either, since the melting point of the RTIL is approximately -30°C (Chem-Spider (2014)).

Our solution to the RTIL injection problem was to fabricate a silicone mesh layer that allowed air to pass through while retaining water (like hydrophobic air filters or a Gore-Tex[®] material). An acrylic mold was prepared by laser micro-machining using a CO₂ laser engraver with minimum power to obtain a grid of cones approximately 150 μm in height and 200 μm apart, as shown in Figure 3.6. A thin layer of a liquid silicone (EcoFlex 0030) was then spin-coated on the acrylic mold at 800 rpm for 30 sec.

Meanwhile, the first sensor layer was heated in an oven at 65°C for 10 minutes. The heated layer was placed on the spin-coated mold, and the assembly was placed in the oven again for curing. The skin was then carefully detached from the mold after curing maintaining the mesh layer bonded on the first sensor layer. The resulting membrane had holes approximately 50 μm in diameter.

The skin was finally filled with RTIL using a syringe with a hypodermic needle, at room temperature, starting from one point and until all channels were filled. The needle was able to penetrate the mesh layer without damaging the net structure by taking advantage of the high stretchability of the silicone material.

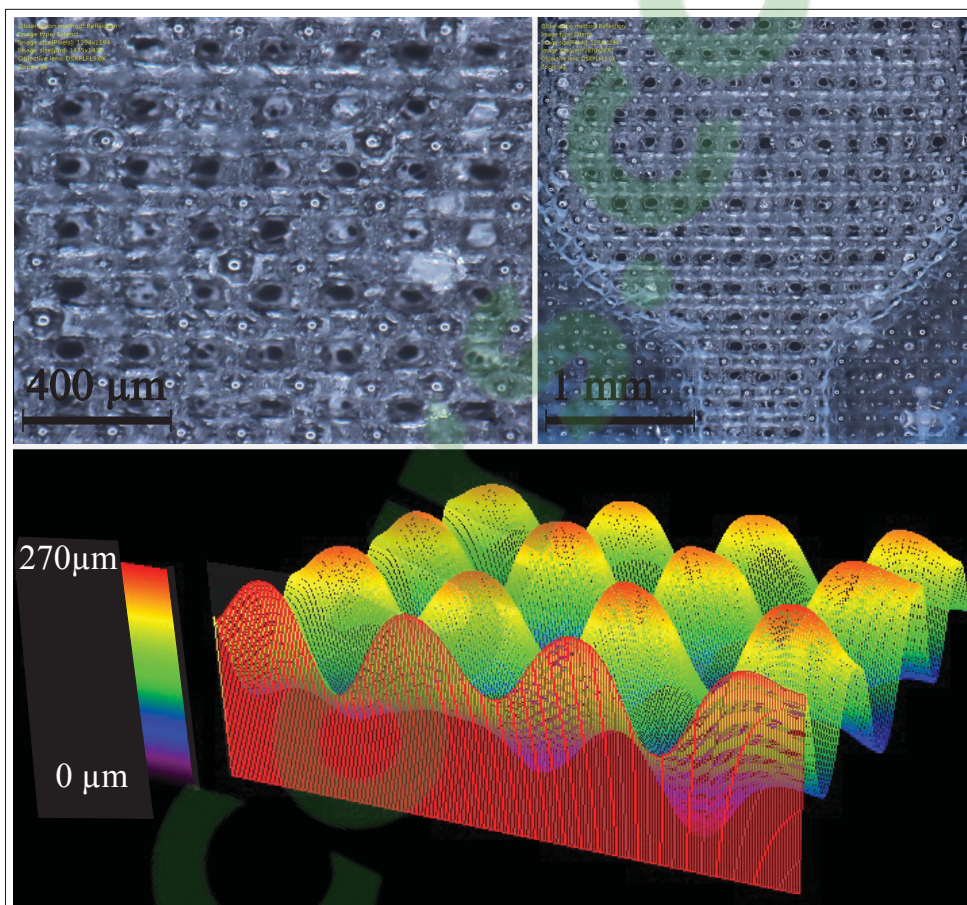


Figure 3.6 Mesh layer mold (top) and 3-D image reconstitution (bottom) with an opto-digital microscope (Olympus DSX-100). Color scale indicates height of structures after laser ablation.

When injected through a microchannel, the RTIL is constrained by the bottom and side walls. This forces the RTIL to either flow forward in the microchannel or to pass through the small holes on the top mesh layer. Although the dynamics of Newtonian liquids are usually con-

strained by the gravitational force, this principle does not apply any more in such small dimensions (Lambert (2013)).

The RTIL's surface tension ($\gamma = 48.79 \times 10^{-4} N \cdot m^{-1}$; Yang *et al.* (2004)) therefore govern the RTIL's flow, and, with the help of the mesh layer, constrains the RTIL to flow undivided through all the networked microchannels. Indeed, the mesh layer holes' are approximately 170 times smaller than the cross-sectional area of the microchannel and allow the air to vent out while being small enough to act decisively on the RTIL's surface tension.

Approximately 1 ml of RTIL was used to fill the microchannel network. We believe that this filling procedure will be useful in other fabrication and design of microfluidic sensors, especially when building complex multi-channel structures.

3.2.3 Sealing of the sensor

The net-like structure should be sealed once the sensor is filled, since wetting of the pores is possible and the RTIL could leak under external pressure. Ecoflex was mixed and degassed for 30 sec and then pre-cured for 5 minutes in the oven at 65°C. This increases its viscosity considerably, although it can still be poured into the enclosed space and spread carefully over the porous surface.

The resulting bond was much better than what we experienced with the conventional approach of bonding two previously cured flat layer, thus insuring good robustness of the skin. This better bonding is mainly due to the geometry of the net-like structure that increase the surface area in contact between the two layers and that also trap the uncured silicone in its pores.

Although the skin was not tested for mechanical fatigues by cyclic loading, the softness and intrinsic elasticity of Ecoflex (900 % elongation at break) as well as the use of only soft or liquid components make the sensor quite robust. Moreover, unlike with the usual channel filling method, our approach did not require to create holes for liquid injection once the sensor has been sealed.

Large forces (about 600 N) were applied to test our sealing methods. These caused no leakage or visible damage to the skin.

3.3 Simulation

Before conducting experiments, we checked our EIT pressure sensing concept through simulation using an open source MATLAB toolkit (EIDORS- v.3.7.1 ; Alder & Lionheart (2006)) for designing and solving an EIT model through the finite element method.

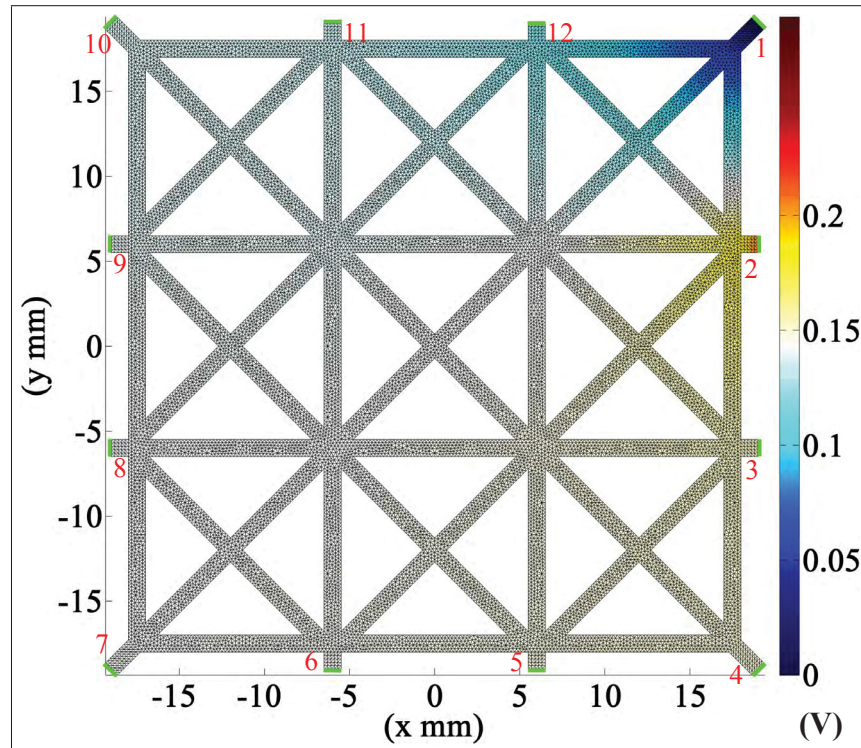


Figure 3.7 Voltage pattern from the first stimulation injecting a constant current into electrode 1 and 2. Each electrode is denoted with the green bars and the orders in red. Color code represents voltage difference in the network.

A base mesh structure of the microchannel network was made in 2-D using a commercial finite element model software (ABAQUS/CAE 6.13-3, Dassault Systems) and exported to EIDORS¹.

As illustrated in Figure 3.7, EIDORS generates a stimulation pattern that follows the EIT imaging protocol. It applies a constant current to each pair of adjacent electrodes and calculates the voltage charged on each element of the mesh through a forward solver. Based on the calculated voltage, the inverse solver of EIDORS reconstructs the conductivity of the mesh and generates an image of the reconstructed conductivity (Vauhkonen *et al.* (2001)).

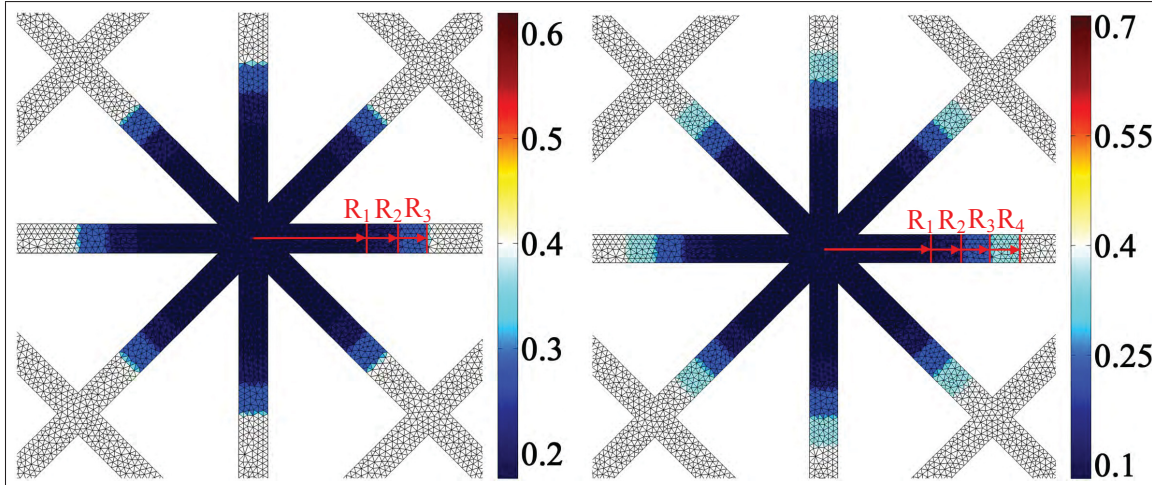


Figure 3.8 Conductivity patterns with different pressure values, 35 kPa (left) and 50 kPa (right). Color code represents conductivity gradient ($S \cdot m^{-1}$). The coefficient ζ determines the boundary of the effective pressure area (R_3 at 35 kPa and R_4 at 50 kPa). At 35 kPa, $\zeta \approx 0.4433, 0.452, 0.5048,$ and 0.7154 for $R_1 = 3$ mm, $R_2 = 4$ mm, and $R_3 = 5$ mm, respectively, and $\zeta \approx 1$ (i.e. $\sigma = \sigma_0$) for R_i ($i \geq 4$); At 50 kPa, $\zeta \approx 0.2047, 0.2171, 0.2926, 0.5935,$ and 0.8949 for $R_1 = 3$ mm, $R_2 = 4$ mm, $R_3 = 5$ mm, and $R_4 = 6$ mm, respectively, and $\zeta \approx 1$ (i.e. $\sigma = \sigma_0$) for R_i ($i \geq 5$). The coefficients are calculated based on the dimensions and material properties of the prototype.

The dimension of this simulation model was the same as that of the sensor prototype. The base mesh structure contains 12 electrodes (resistance: 0.2Ω) and a circular pressure area (diameter: 6mm), as shown in Figures 3.7 and 3.8, respectively.

¹ A .vrm file generated in ABAQUS was converted to a .stl file using MeshLab (Cignoni *et al.* (2008)), and then the .stl file was imported to EIDORS.

Chapter 2 presented simple model for microchannel deformation as a function of strain, in this chapter we will use a more accurate analytical model for hyperelastic pressure sensing from Park *et al.* (2010). The equation expresses the conductivity of the pressure area expressed as a function of the applied pressure.

$$\Delta R = \frac{\rho L}{wh} \left\{ \frac{1}{1 - 2(1 - \nu^2)w \chi p/Eh} - 1 \right\} \quad (3.1)$$

ρ , ν , and E are the electrical resistivity of the ionic liquid, and poisson's ratio and elastic modulus of the silicone material, respectively. L is the length of the microchannel, w and h are the width and height of the cross-section of the microchannel, respectively, and χ is a correction on the channel center line. Then, based on Eq. (3.1), the new conductivity of the pressure area is:

$$\sigma = \zeta \cdot \sigma_0 \quad (3.2)$$

where σ_0 is an initial conductivity and the coefficient $\zeta = 1 - 2(1 - \nu^2)w \chi p/Eh$.

Since the applied pressure has an influence on the conductivity changes of not only the pressure area but also its vicinity, in Eq. (3.2), the effective pressure area was calculated and used in the simulation, as illustrated in Figure 3.8.

Using this conversion process, we simulated the deformation of the skin, as shown in Figure 3.9. Both pressure locations and magnitudes were estimated for different pressure inputs, show in Figure 3.9(a), using an input current of 10 mA. The following parameters were also used in the simulation: $\sigma_0 = 0.398 \text{ S} \cdot \text{m}^{-1}$, $\nu = 0.49$, and $E = 125 \text{ kPa}$. 20dB of SNR (Signal-to-Noise Ratio) was also included make a similar condition of actual sensors.

The results showed the minimum conductivity at the center of the pressure and a gradual conductivity increase at the adjacent areas as the distances from the center increase reaching the

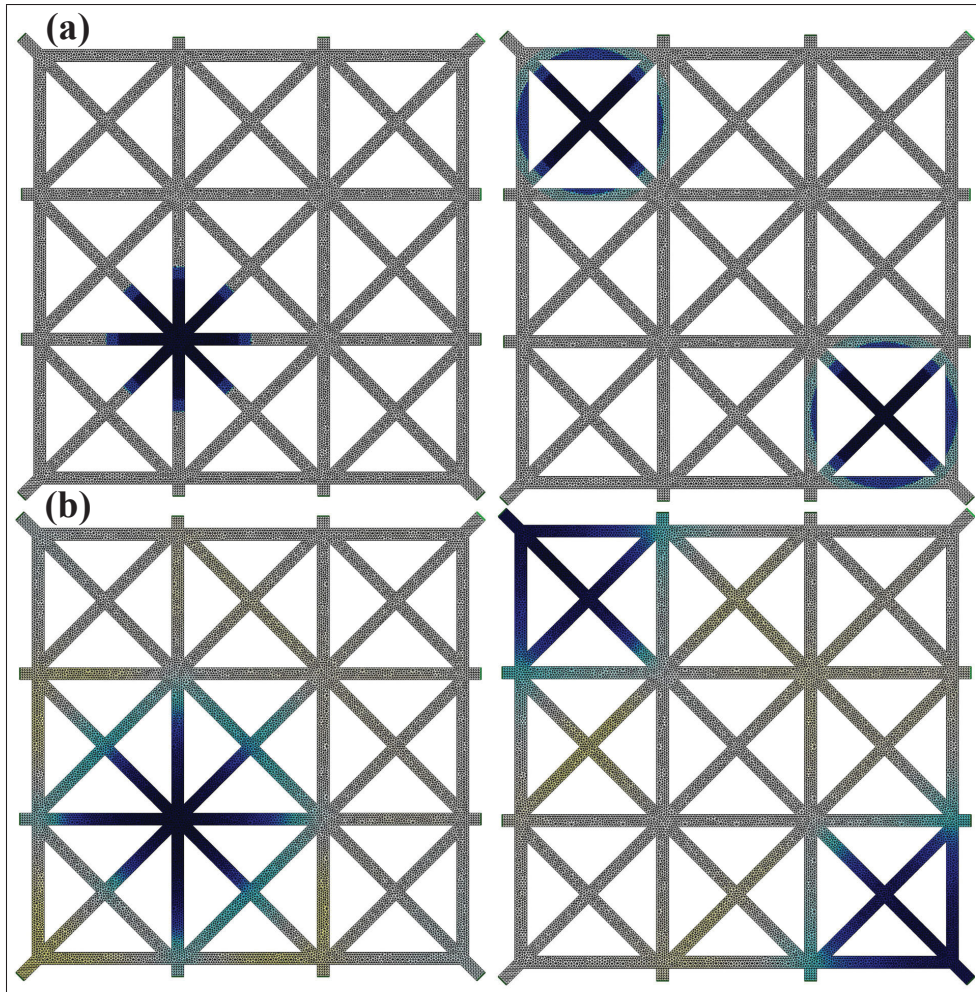


Figure 3.9 (a) Conductivity distributions with one point load ($p=35$ kPa) centered at $(x=-6\text{mm}, y=-6\text{mm})$ and two point loads ($p=50$ kPa) centered at $(x=-12\text{mm}, y=12\text{mm})$ and $(x=12\text{mm}, y=-12\text{mm})$. (b) Images of reconstructed conductivity of the loads.

initial conductivity (σ_0) eventually. The conductivity reconstruction (i.e. pressure estimation) was reliable regardless of the magnitudes and the number of the pressures.

Although the current approach does not incorporate the 3-D deformation of the microchannels, the simulation results demonstrated that the EIT can be easily combined with microfluidic soft sensing devices for detecting contact pressures.

3.4 Experiments: contact location and image reconstruction

The goal of this chapter was to present a novel idea of implementing EIT to a touch-sensitive skin filled with an IL and discuss the design challenges associated with this approach. The inverse EIT problem is a complex topic on which many papers have been published over the last 20 years.

Future work may target the question of how one can improve the touch image quality using more complex but more precise reconstruction algorithms. In the meantime, this section will present simple experiments conducted on the skin prototype in order to show that the proposed fabrication method leads to artificial skin that can effectively detect pressure contacts as well as their magnitudes.

3.4.1 Sensing mechanism of the skin

Given that the specific conductivity of the ionic liquid is isotropic and since the number and shape of the channels is known, the skin can be modeled as a matrix of resistors in which each channel section is a resistor and each connection between the channels is a node.

The impedance of an ionic liquid is a function of the distance between electrodes, and the smallest cross-sectional area of the microchannel between the electrodes, and the liquid conductivity. The pressure applied to the skin will deform the microchannel and decrease its cross-sectional area, and it consequently increases the impedance that can be measured from the electrodes located at the edge of the skin.

Since the impedance changes are due to the area changes of the cross-section of the microchannel, and also the deformed silicone elastomer can easily return to its original shape when the pressure is released, the impedance changes are highly predictable and reproducible.

In addition, the dynamics of ions as charge carriers are constant in a large frequency domain (Zhu *et al.* (2009)), whereas the paths of current as modified by forces applied to silicone doped with conducting nanoparticles are far more difficult to predict (Lacasse *et al.* (2010); Kost *et al.*

(1994); Ding *et al.* (2007)), the sensing mechanism in the our skin is more reliable than that those of EIT skin sensors that use conductive rubbers (Nagakubo *et al.* (2007); Kato *et al.* (2007)).

3.4.2 EIT image reconstruction

A conventional way of acquiring EIT data is measuring electrical potentials between all the electrodes except two electrodes to which an alternating current (AC) is injected. This process is repeated by changing the two injection electrodes until it covers all the electrodes (Nagakubo *et al.* (2007); Kato *et al.* (2007)).

Complex numerical methods may be used to reconstruct the image from the obtained data. However, in our case, we employed a simple numerical method called *weighted filtered back projection* (Kotre (1994)) since the purpose of our experiments was to validate the concept of using EIT on a soft skin sensor that contains an network of embedded conductive microchannels.

In our method, the image reconstruction algorithm creates a matrix by attributing a score to each node of the skin. This score is calculated by summing the impedances of the channels crossing at this position. This simple method provides accurate results, since our skin is composed of a discrete set of channels that follow a symmetric organization as opposed to the unknown medium generally explored with EIT, thus simplifying the problem. Furthermore, the conductivity of EMISE ionic liquid is isotropic, which makes the current flow inside the channels much more predictable.

Normal forces were applied to the skin using a commercial force gauge (M4-10, Mark-10) and a test stand (ES10, Mark-10), and the impedance was measured at 1 kHz at the edge electrodes of the skin. To apply a force in a repeatable manner, a rigid cylindrical end-effector (6 mm in diameter, 6.35 mm in height) was mounted on the force gauge.

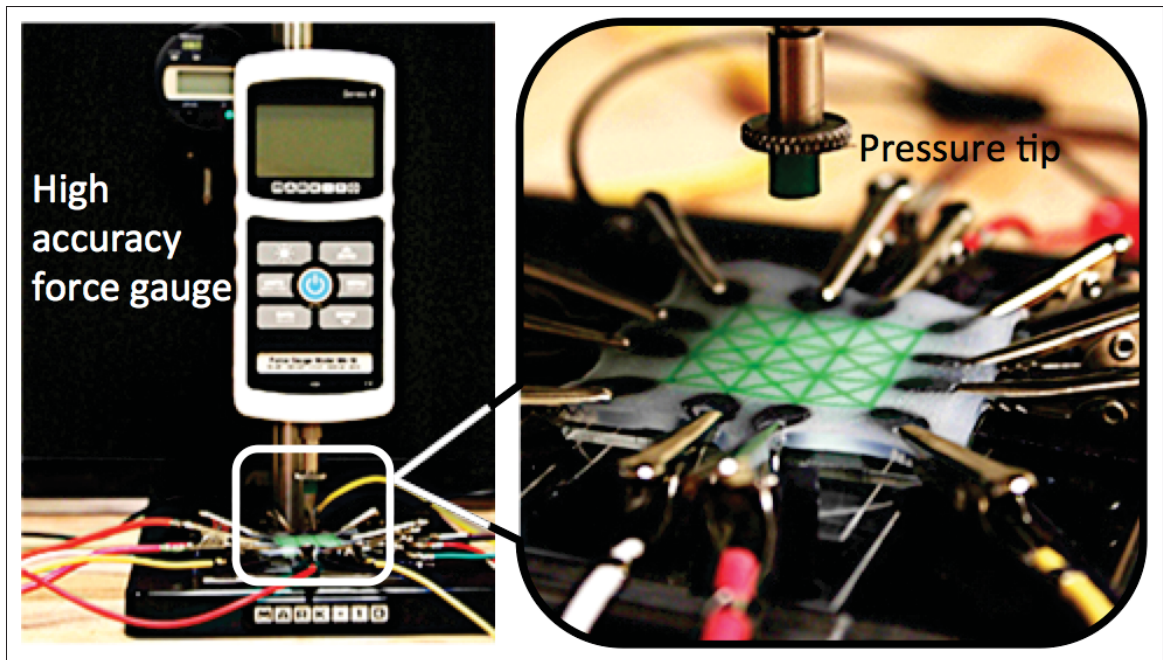


Figure 3.10 Experimental setup for pressure response measurement using a high accuracy force gauge (left) and the close-up view of the sensor and the pressure tip (right).

Since the measurements were performed manually using an external device, a simple custom data acquisition protocol was followed. Impedance was measured between one electrode and the next, in a clock-wise order, without redundancy. Measurements were performed first without any load in order to populate a calibration matrix used to evaluate the impedance due to other causes than the RTIL filled channels, and mitigate their impact on the sensors' accuracy.

The end-effector was then brought down to the skin until the force measured by the force gauge reached target value. The experimental setup is shown in Figure 3.10.

Two experiments were conducted to evaluate the skin prototype. In the first experiment, a single load with three different force levels were applied to a same location. The skin was able to detect both the location and the magnitude of the force, as shown in Figure 3.11.

For the force estimation, the resistance difference between the collected data and the calibration matrix was calculated and then filtered through bicubic interpolation in MATLAB. Al-

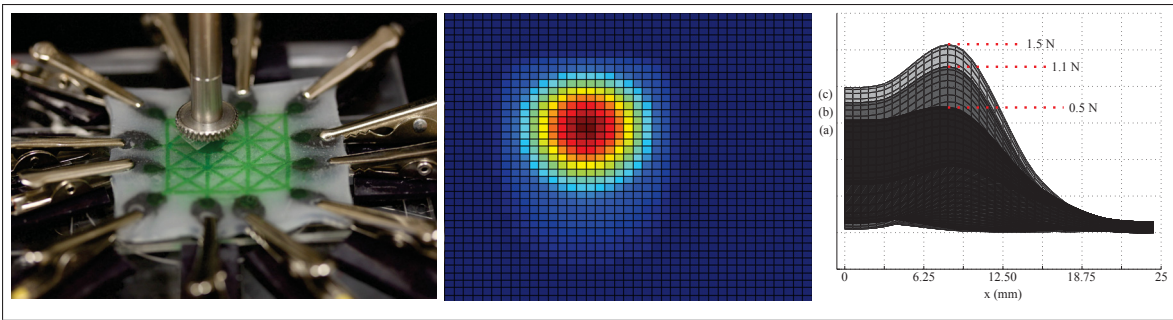


Figure 3.11 Photo of the pressure application experiment (left) and its post-processed estimated pressure image (center) with Matlab generated images of 3 distinct forces applied at the same skin position (right).

though the experiments were simple and use only one subset of the measurements obtained, this method demonstrates the capability of extracting the location and magnitude of a contact.

The contact was detected exactly at the same location of the actual load. Also, although the relationship is not exactly linear, the three different forces were estimated with the three shaded curves with peaks of different amplitudes in Figure 3.11.

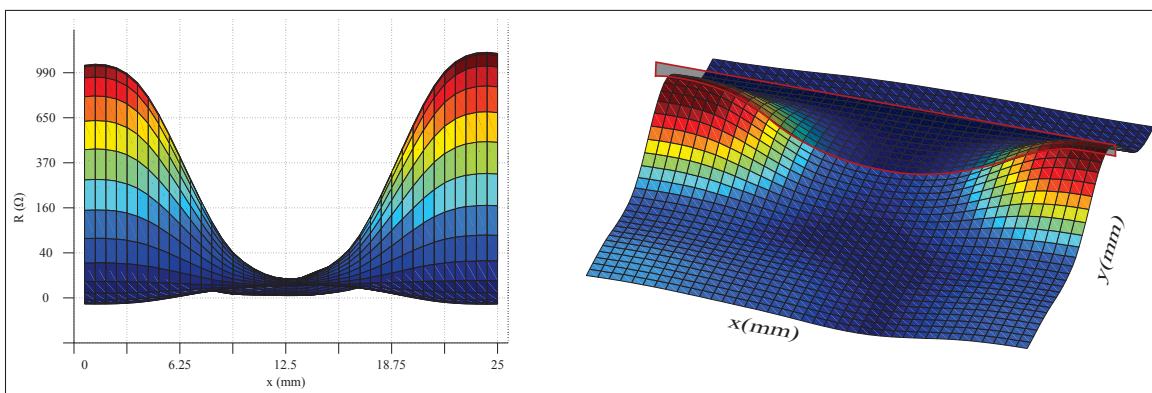


Figure 3.12 Matlab images and cross section view caused by the two contact points of the force gauge end-effector with a force of 0.5 N, and demonstrating skin ability to detect multiple contact location. Both images were built from the differences in resistance between the calibration matrix and the deformed skin's matrix. (The y-axis scale of both plots is not linear since it is based on bicubic interpolation of image processing.)

In the second experiment, two same loads (0.5N) were applied to the two different locations. The result, shown in Figure 3.12, shows that two same resistance changes were detected at the two contact locations.

The experimental results validated that our skin prototype was able to identify the locations and magnitudes of contact forces for both single and multiple load conditions.

CHAPTER 4

SOFT WEARABLE MICROFLUIDIC SKIN FOR HAND MOTION DETECTION

We become what we behold. We shape our tools, and thereafter our tools shape us.

Marshall McLuhan

As a final step toward a wearable prosthetic strain sensing skin, we developed and tested a soft wearable strain sensing skin that was mounted on a human hand. Indeed, human hand motions are more complex than today's prosthetics, and thus represent the ultimate sensing challenge.

Motion sensing must be achieved through both precise and unobtrusive measures. Our design thus aimed for increasing the compactness of the device and also for improving its performance, which have not been easy to achieve simultaneously in the previous designs.

The skin showed in Fig 4.1, was cast from a soft silicone rubber that can easily conform to a human hand. The skin contains embedded microchannels filled with liquid conductors for stretchable sensing and wiring. The liquids in the microchannels do neither introduce rigidity to the structure nor increase the size of the device.

4.1 Design

4.1.1 Sensor configuration

A human hand is highly complex and requires 24 DOFs to be fully kinematically modeled (Cobos *et al.* (2008)). However, the concept of motor synergies (Santello *et al.* (1998); Prattichizzo *et al.* (2010)), which couple more than one DOF joint motions of one or more fingers, allows us to simplify some finger motions by defining the coupled joints.

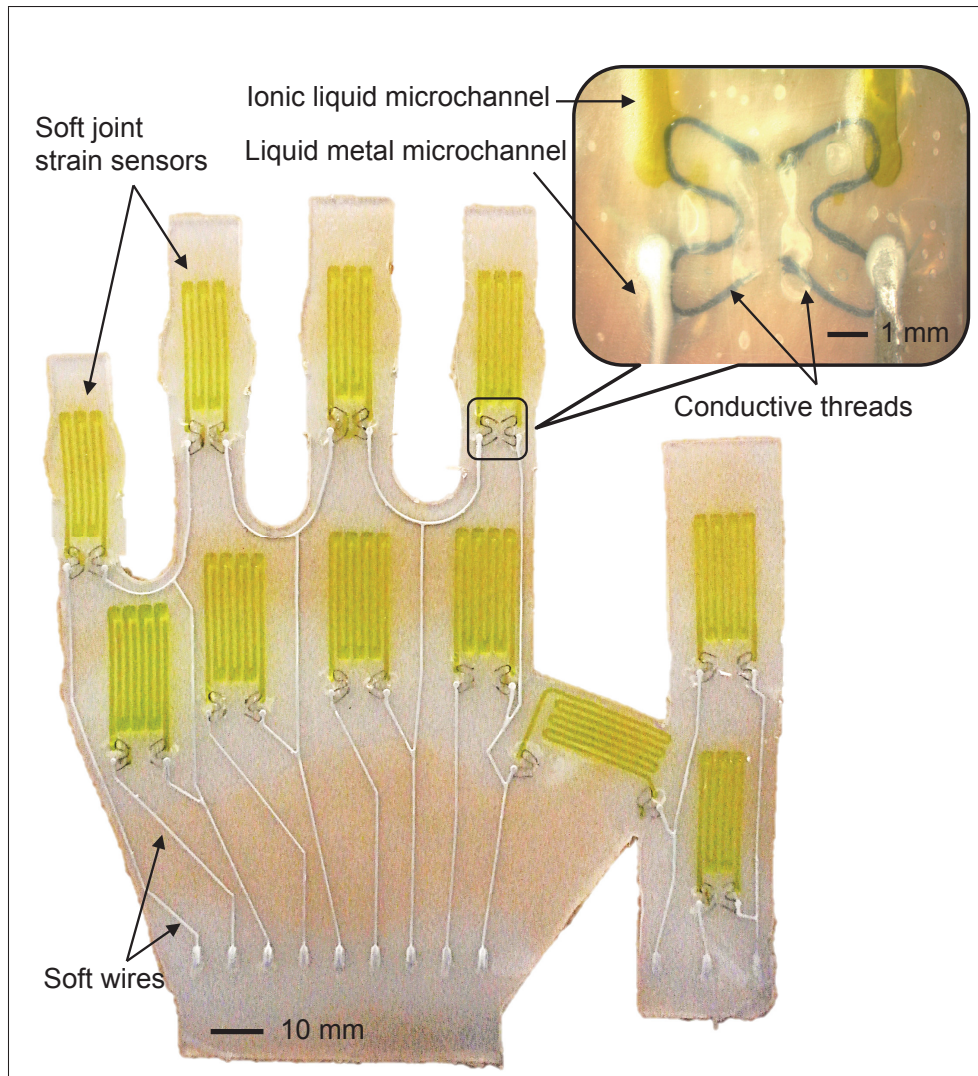


Figure 4.1 Artificial skin prototype with embedded components.

Possible reasons for the motor synergies are i) mechanically, fingers share tendons, and ii) neurophysiologically, the central nervous system simplifies the control effort for certain motions for known tasks (Todorov & Ghahramani (2004)). These synergies allow us to reduce the number of necessary sensors for reconstructing general hand motions as long as the selected sensing joints are not coupled to each other (Bianchi *et al.* (2012)).

We decided to place two sensors on each of four long fingers (i.e. index, middle, ring and little fingers), one on the metacarpal-phalangeal (MCP) and the other on the proximal inter-

phalangeal (PIP), making total eight sensors on these four fingers. The other three sensors were placed on the thumb, the first on the inter-phalangeal (IP) joint, the second on the metacarpal-phalangeal (MCP) joint, and the third between the thumb and index finger. Fig. 4.1 shows the actual prototype of the skin and the sensor configuration.

With this configuration, the skin prototype can detect the flexion and extension motions of the MCP and PIP joints of the four long fingers, and also the same motions of the IP, MCP, and Carpometacarpal (CMC) joints of the thumb. In addition, the sensor between the thumb and the index finger detects abduction and adduction motions of the thumb that are important to reconstruct the hand gestures (Ingram *et al.* (2008)).

No sensors were placed on the distal inter-phalangeal (DIP) joints since the DIP joint motions can be deduced from the PIP joint motions of the same finger based on the coupling effect of the two joints (Cobos *et al.* (2008)), which simplifies our design by reducing the number of sensors and signal wires.

4.1.2 Detection mechanism

4.1.2.1 Microfluidic sensing

Based on the research presented in previous chapters, we decided to use soft microfluidic sensors for their compliance and simple behavior. Therefore, a thin elastomer layer with embedded microchannels filled with conductive liquids was used as a highly stretchable and flexible sensor.

When placed on each joint of the hand, the microchannel of each sensor stretches as well get compressed with finger flexion motions. When stretched, the length of the microchannel increases and also the cross-sectional area decreases, which consequently increases the electrical resistance of the microchannel without disconnecting the circuit (Park *et al.* (2010, 2012a)).

Two different microchannels were embedded in our skin prototype with the cross-sectional areas of $700\ \mu\text{m}$ (width) \times $500\ \mu\text{m}$ (height) for an ionic liquid and $300\ \mu\text{m}$ (width) \times $500\ \mu\text{m}$ (height) for a liquid metal.

4.1.2.2 Conductive liquids

Again, two different conductive liquids were selected: a RTIL for strain sensing and a liquid metal for soft wiring (eGaIn ; Dickey *et al.* (2008)).

RTILs, presented in the previous chapter, are conductive liquids exclusively made of ions. Our prototype was filled with the same 1-ethyl-3-methylimidazolium ethyl sulfate (EMISE, Sigma-Aldrich) since it shows a relatively high ionic conductivity (resistivity: $\rho = 25 \times 10^{-3}\ \Omega\cdot\text{cm}$) and low toxicity.

Since typical hand motions are involved with skin stretches in multiple places on the hand, we needed to decouple finger joint motions from the skin stretches on non-joint areas for more accurate measurements. Therefore, we decided to employ a dual-liquid system in which the RTIL is used for the sensing microchannels while eGaIn is used for the soft wiring.

4.1.3 Instrumentation circuit

The conductivity of the RTIL is based on the movement of ions acting as charge carriers. If connected to a direct current, the ions of the RTIL will be attracted by the poles and polarize the electrodes, which prevents the sensors from generating reliable impedance values.

To address this issue, the impedance of the RTIL was measured by applying an alternating zero-centered signal using a custom designed instrumentation circuit. This time, the instrumentation circuit used a Programmable system - on - Chip (PSoC – CY8C38LTI068, Cypress Semiconductor) that contained an internal micro controller and firmware programmable digital and analog components.

Two operational amplifiers in this unit were used to generate a square, zero-centered, waveform whose frequency depends on the impedance of the sensor. The frequency of the waveform is then estimated within the PsoC, by a counter. Fig. 4.2 shows the overall architecture of our sensing and instrumentation system.

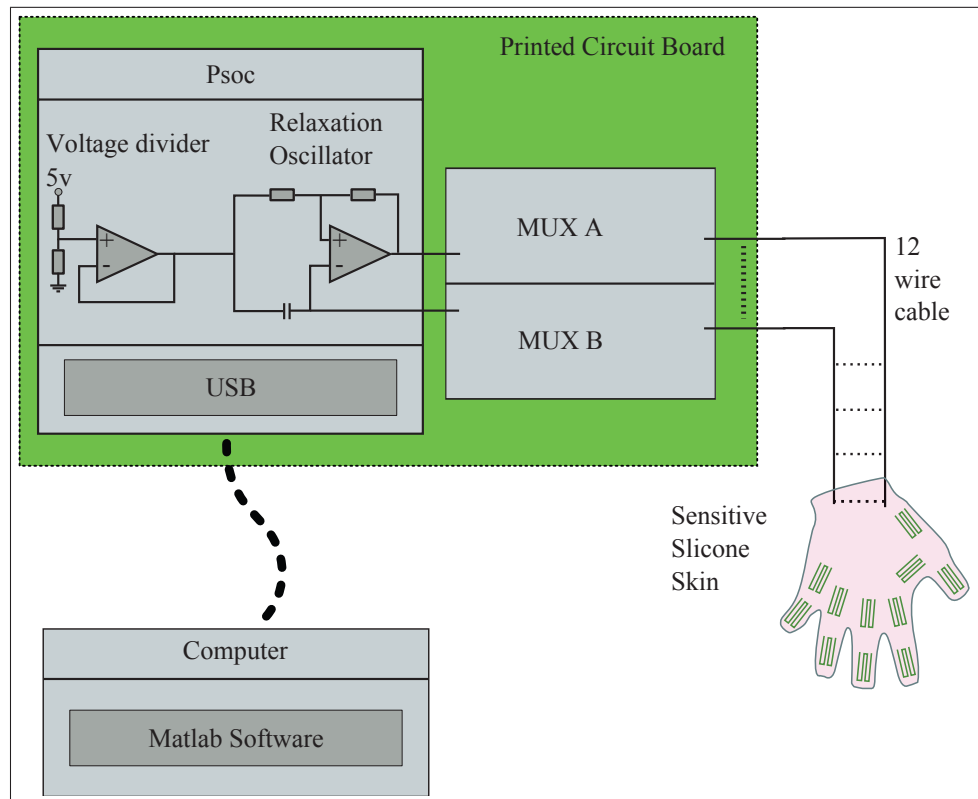


Figure 4.2 Artificial skin sensing system architecture.

In order to switch the sensor readings between the 11 sensors, a single chip dual analog multiplexer (ADG726, Analog Devices) was used, which allowed us to selectively link the PSoC to any of the 11 skin sensors.

To capture the hand motions, the multiplexer was commanded to switch the sensor readings among the 11 sensors and their impedance values were evaluated by the PSoC. Then, the sensor readings are transmitted to the computer.

Since the impedance values of the sensors change the frequency of the square wave, it is not straightforward to define the sampling rate. However, using the highest possible impedance value of the sensors, we can calculate the lowest sampling rate.

When switching the readings among the 11 sensors, the longest acquisition time for the entire skin would be $A_{cq} = 2T \times 11$ where T is the maximum period of the sensor square wave, and A_{cq} is the acquisition time.

From Chapter 2, we know the equations governing the period:

$$B = \frac{R_1}{R_1 + R_2}$$

and

$$T = 2R_s(f)C_1 \ln \frac{1+B}{1-B}$$

where C_1, R_1 and R_2 are capacitance and resistances on the circuit that is used to regulate the frequency range of our square wave. After experiments, we determined our maximum sensors impedance to be $R_s \approx 500 \text{ K}\Omega$. In our circuit, we chose $C_1 = 1 \mu\text{F}$, $R_1 = 22 \Omega$ and $R_2 = 100 \text{ K}\Omega$, which gives $T \approx 0.44 \text{ ms}$. Finally,

$$A_{cq} = 11 \times T \approx 4.84 \text{ ms}. \quad (4.1)$$

Therefore, the theoretical lowest sampling frequency for the entire skin is about 200 Hz, which is much higher than the recommended frequency for hand motion detection (Simone *et al.* (2007)).

4.2 Manufacturing

The manufacturing involves multiple steps of polymer casting and component embedding, as shown in Fig. 4.3.

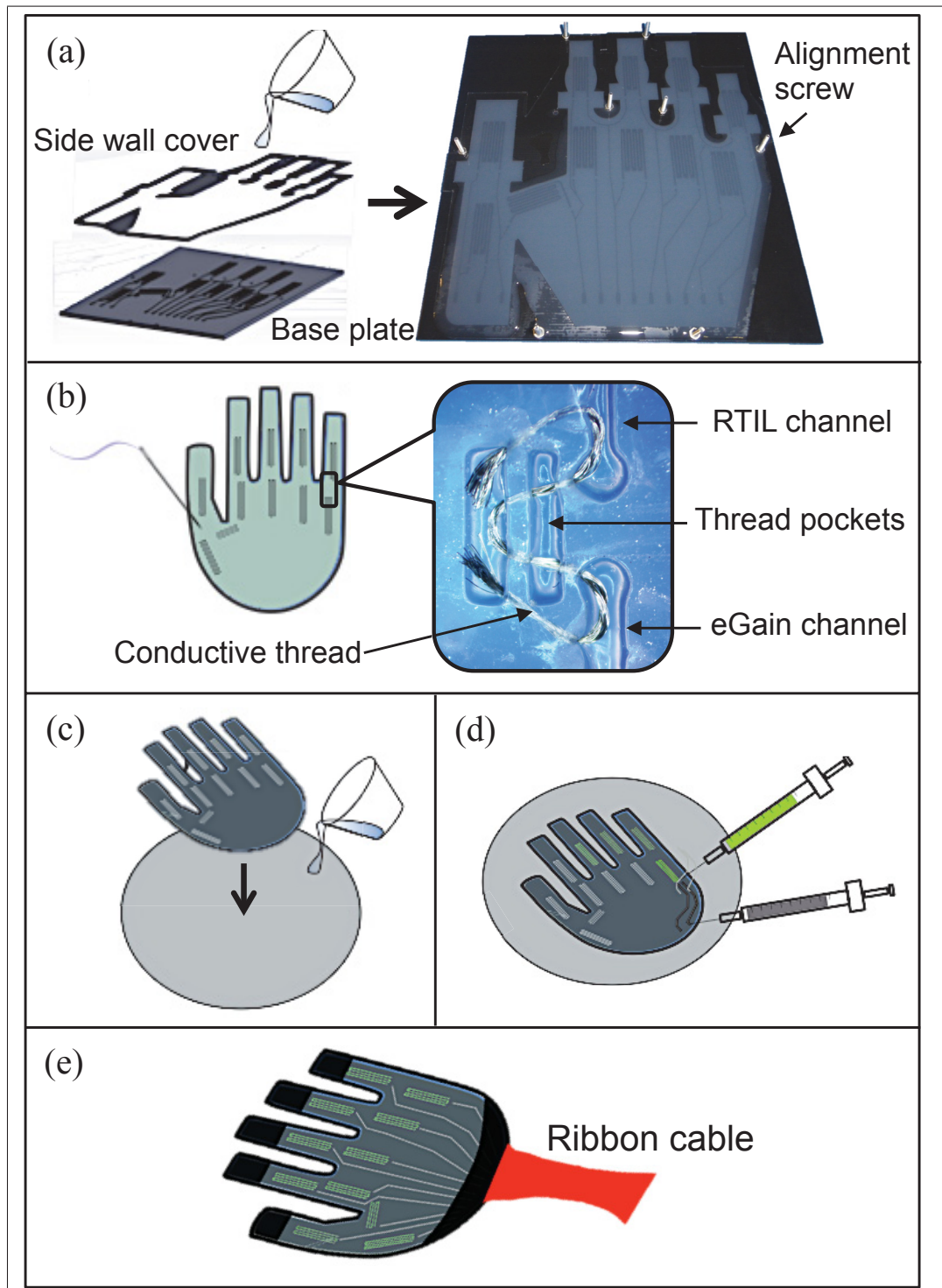


Figure 4.3 Manufacturing Process for Sensing Skin: (a) Mold preparation and elastomer casting. (b) Conductive thread embedding. (c) Microchannel sealing by laminating a flat elastomer layer. (d) Liquid conductor injection. (e) Signal wire connection and attachment of finger and hand fasteners.

4.2.1 Mold preparation

The skin prototype is made of extremely soft elastomer (Ecoflex 00-30, Smooth-On, shore hardness 00-30, elongation at break 900%) that is cured (at 60°C for approximately 25 minutes) by mixing two parts (resin and hardner, 1:1 mixed ratio in weight) in a custom-designed mold. Since the skin layer is very thin and soft, the tension of the skin does not cause any constraint (or fatigue) to the user's motion.

The mold is composed of two pieces: a 3-D printed (Objet30, Stratasys) flat base plate with protruded sensor and soft wire microchannel patterns and a laser cut (Epilog Mini, Epilog Laser) side-wall acrylic cover (1.6 mm thick) that defines the boundary of the skin to be cast. The side-wall cover is aligned and fixed to the base plate using alignment screws. The sensor channels were placed on top of the selected finger joints and the wire channels were designed to connect the sensors to the wrist.

4.2.2 Skin sensor layer

A liquid elastomer is poured on the assembled mold and cured in the oven at 60°C for approximately 25 minutes. When removed from the mold, the cured elastomer layer (1.6mm thick) contains all the microchannel patterns for strain sensing and soft wiring.

Before sealing the microchannels, conductive silver threads are manually sewn into the elastomer through the pockets near the microchannels, as embedded interfaces between RTIL and eGaIn. The multiple wavy turns of the threads not only tolerate the stretch of the skin with reliable electrical connection but also aimed at preventing one liquid from invading the other. Given the large number of channels to connect, conductive threads aimed at interfacing conductive liquids in more scalable manner than the previously manufactured soft polymer interfaces. It also allowed the use of very common and commercially available conductive material.

After all the thread interfaces are embedded, the sewing pockets are filled with a silicone glue (Sil-Poxy, Smooth-On, shore hardness 40A).

4.2.3 Sealing and injection

To seal the microchannels with the silver threads, a thin, flat base elastomer layer (approximately 800 μm) is prepared by spin-coating the same liquid elastomer at a low speed (600 rpm for 6 sec. and 350 rpm for 25 sec.) on a flat surface. Once the flat layer is fully cured, another much thinner layer of the liquid elastomer is spin-coated at a higher speed (1600 rpm for 25 sec.) on top of the cured layer to be used as a bonding agent.

Before curing the second layer, the original skin sensor layer is laminated on top. The two cured layers bond while the thin intermediate layer cures. A thickness of 2 mm was achieved over the entire area of the complete skin in this process.

When the entire skin is fully cured, conductive liquids are injected using two hypodermic syringe needles: one for injecting the liquid conductors and the other for releasing the trapped air in the microchannels.

4.2.4 Signal wires and hand fasteners

The skin is connected to the instrumentation circuit using a 12 wire flexible ribbon cable on the wrist part of the skin. Stretchable hook and loop straps are attached to the wrist and to the ends of the fingers to fasten the skin prototype to the back of the hand reliably. The stretchable fasteners allow the user to wear and take off the skin easily without constraining the natural hand motions.

4.3 Data collection and signal processing

The raw period data of 11 sensors were collected and processed using MATLAB (The MathWorks, Inc.). The mapping and 3-D graphic rendering was achieved with SynGrasp 2.0, an open source MATLAB toolbox for grasp analysis (Malvezzi *et al.* (2013)). The modeling of hand adapted in SynGrasp is based on Denavit-Hartenberg parameters. With the input joint

angles, the hand gesture could be calculated from the base joint – MCP joint in our model – of each finger.

For the maximal representations of hand motions that use all the 11 sensors in the skin, we construct a paradigmatic hand with 15 DOFs. The horizontal movements of the fingers were constrained in fixed angles due to the limitation of the 2-D sensing capability of our design.

The two sensors at the IP and MCP joints and the one between the thumb and the index finger calculate the motion of the thumb in the computational model. The motions of the other four fingers are calculated by the two sensors placed on PIP and MCP joints of each finger. The IP joint motions of the four fingers are calculated synergistically from the previous PIP joints by multiplying by a factor of $2/3$ based on Li *et al.* (2011a).

For 3-D graphical reconstruction in real-time, the skin prototype requires an initial calibration that records the sensor data of two extreme finger positions – full extension and full flexion. Then, the sensor signals are linearly interpolated to be mapped to the graphic model. The linear relationship between sensor signals and joint angles has been already verified for this type of soft strain sensors (Park *et al.* (2014)).

4.4 Preliminary characterization

To characterize and evaluate the performance of our prototype, two preliminary experiments were conducted. The first experiment is calibration of an individual sensor. In this test, a single strain sensor was linearly stretched up to 200% using a commercial force/torque test stand (Mark-10 Motorized Test Stand ESM301), and the resistance of the sensor was measured.

The second experiment is calibration of the skin prototype with a hand. The skin was mounted on a human hand, and the index finger was bent from 0° to 130° 10 times, step by step, with a 10° increment. The actual angle was measured using a manual goniometer in 2-D. The results of these two experiments are shown in Fig. 4.4.

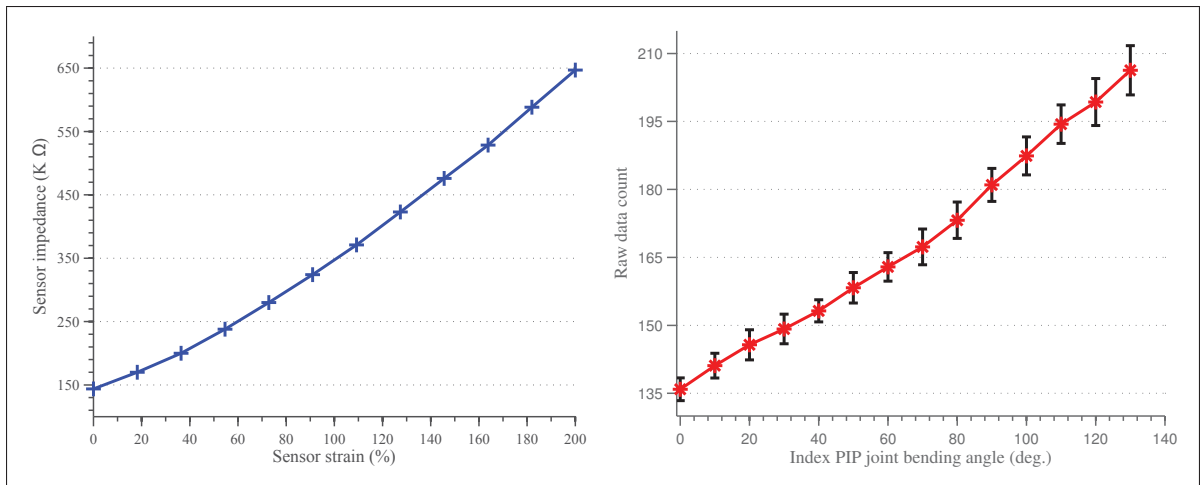


Figure 4.4 Psoc raw data of an individual sensor, during single axis strain test (left) and index joint bending (right).

Both strain and bending test results showed linear responses. The bending result also showed repeatability of the sensors with multiple tests. However, skin movement or slippage during the experiments was not examined in this stage.

Assuming the other sensors work in the same way, these preliminary results can be extrapolated to the other joint motions except for thumb abduction–adduction. Based on the initial calibration, the skin provides joint angle information in real-time without drift, and the hand motions can be easily reconstructed without any noticeable time delays, as shown in Fig. 4.5.

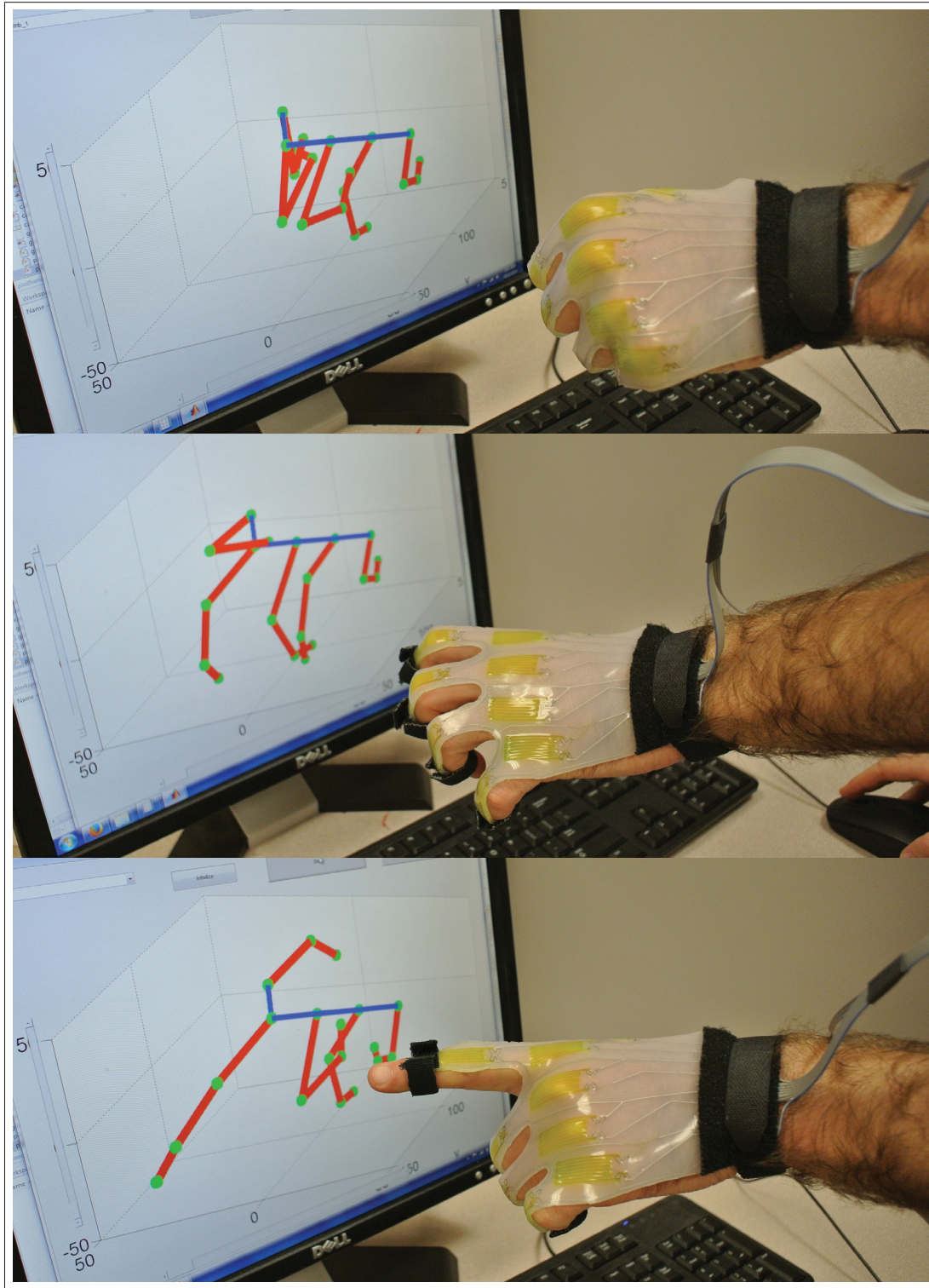


Figure 4.5 Snapshots of real-time sensing system with 3-D graphical reconstruction. All five fingers (red lines) with multiple joints (green dots) rotate on the virtual anchor (blue line) based on the sensor signals from the skin.

Part II

Prosthetic actuation through the "Programmable Permanent Magnet" actuator

CHAPTER 5

THE "PROGRAMMABLE PERMANENT MAGNET" ACTUATOR

We are all atheists about most of the gods that humanity has ever believed in. Some of us just go one god further.

Richard Dawkins



Figure 5.1 The programmable permanent magnet actuator.

Despite great technological advancement, prosthetics continue to lag behind human limbs in their abilities to perform a variety of commonplace physical tasks. One reason for this is the present-day limits of actuators.

The main problem with prosthetic actuation is that conventional electromagnetic actuators are inherently ill-suited to prosthetics. It might seem surprising that out of the variety of actuators that have been invented and improved upon since the 1830s (Doppelbauer), not a single one is truly appropriate for prosthetics. Even though innovations in actuators have brought about great improvements in electric cars, for instance, they have not done the same for prosthetics or humanoid robots, because they require a completely different type of actuation.

Conventional actuators, such as DC or brushless motors, reach high efficiency at high speeds (due to back electromotive force, or back EMF), but prosthetics applications typically require low-speed high-torque movements, for which conventional motors are much less efficient. This inefficiency has three consequences: *i.* prosthetics consume more power than necessary, thus draining batteries; *ii.* the amount of excess heat that is generated (as described by the Joule effect) can result in damage to the motor or in discomfort to the user; and *iii.* due to the risk of heat damage, the actuator's torque is limited.

This issue is not specific to prosthetics and can be found in many robotics applications too. The typical work-around to this problem has been to use gearboxes. Gearboxes change the ratio of speed to torque (converting a high-speed low-torque input to a lower-speed higher-torque output), allowing the motor to operate at a higher speed, which is more efficient. However, gearboxes introduce new issues such as backlash, additional weight, high reflected inertia during collisions, and sometimes non-backdriveability (Seok *et al.* (2013)).

Another problem with gearboxes is that they do not work for situations where a prosthetic joint applies torque in a fixed position. This is particularly relevant to prosthetics (as opposed to say, cars), because they frequently need to apply torque while not actually moving, such as while gripping an object or standing upright. In these scenarios, the actuators at the robot's joint must maintain torque without rotating; and thus the motor is operating in the zero-efficiency zone (maximum power input and zero power output).

Numerous attempts have been made to circumvent the shortcomings of conventional motors in robotics, where actuator torque is of major importance (Urata *et al.* (2008, 2010); Kozuki *et al.* (2016); Hochberg *et al.* (2013); Wensing *et al.* (2017)). One method has been to improve the actuator's heat dissipation properties. Among the most successful examples of this method is the water-cooled motor system that helped the SCHAFT team win the Darpa competition trials (Urata *et al.* (2008, 2010)). Their robot's actuators were able to output higher torque because the excess heat was dissipated by a custom-built liquid cooling system. Although this

is an ingenious method, it still does not address the root of the problem: the inefficiency of conventional motors in most robotic applications.

In light of these problems, we propose a fundamentally new approach to prosthetic and robotic actuation: the "Programmable Permanent Magnet" (PPM) actuator, which is illustrated in Fig 5.1). The PPM actuator is capable of sustaining a variety of torques indefinitely, and for a given torque, the motor's energy consumption is directly proportional to its velocity. To the best of our knowledge, this is the first actuator to have these characteristics, which are particularly promising for prosthetics applications.

Section 5.1 explains important concepts needed to understand the motor's operation. Section 5.2 presents the design of the prototype. Section 5.3 describes the experiments conducted with the prototype, and gives their results.

5.1 A novel paradigm for torque generation

A typical motor, such as a Maxon brushless motor, takes the electrical power that's supplied (P_{in}), and transforms it with some loss (P_{loss}) into mechanical power (P_{mech}), where the latter is a direct function of torque and rotational speed, thus allowing us to also calculate the efficiency (η). These relations are given by:

$$\begin{aligned} P_{in} &= P_{loss} + P_{mech}, \\ \eta &= \frac{P_{mech}}{P_{in}}, \end{aligned} \tag{5.1}$$

where

$$\begin{aligned} P_{in} &= Vi \\ P_{mech} &= \tau\omega \\ P_{loss} &= i^2R \end{aligned} \tag{5.2}$$

and where i is the actuator's current, V is its voltage, and R is the electrical resistance of the winding.

When a conventional motor operates at its maximum speed, it's not able to exert any torque. This point is known as no load speed, and when it's reached there is very little power output. However, the motor is still operating quite efficiently because it's not drawing much electrical power either, due to a phenomenon called back electromotive force (back EMF). This phenomenon balances the voltage applied across the windings, thus reducing the effective current flow and heat generation in the windings.

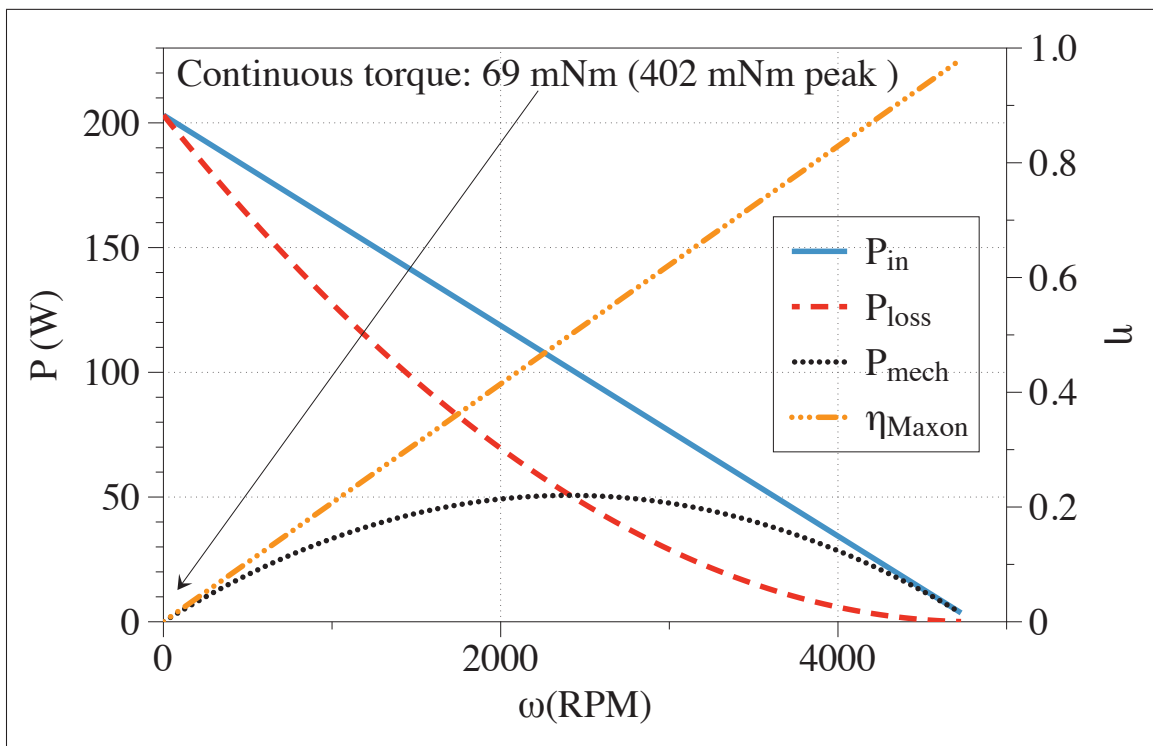


Figure 5.2 Maxon 339286 brushless motor power characteristics

As can be seen from Fig. 5.2 made using the datasheet of the Maxon brushless motor 339286, at slightly lower speeds (than maximum), the motor exerts torque. Here it operates in a very efficient zone because it is converting almost all the electrical power into mechanical power.

So at medium-to-high speed and torque, the motor is highly efficient. But at very low speeds it's a different story. At low speeds the motor is also producing very little power, but this time there is not as much back EMF to help lower the power input. Instead, the motor is consuming its maximum amount of electrical energy – and when there is no speed, all of this energy is wasted in the form of heat. To summarize, conventional motors exhibit very good efficiency at high speeds, and very low efficiency at low speeds.

In both a DC motor and in our motor, movement and torque are created by the interaction between two magnetic fields: one fixed (a permanent magnet), and one variable. However, whereas in a DC motor the variable field is a temporary electromagnetic field controlled by an electrical current, in our actuator, both the fixed and variable components are permanent magnets. We "set" the magnetic field of one permanent magnet to a given value, and create motion by constantly "resetting" this field.

To do so, our PPM actuator relies on current pulses to generate strong magnetic fields that will magnetize the hard ferromagnetic material of the windings. Hard and soft ferromagnetic materials are distinguished by their ability to retain magnetic fields: hard ferromagnetic materials are much more difficult to demagnetize than soft ferromagnetic materials.

In other words, in the PPM actuator, the current is used to magnetize magnets in the windings. The PPM actuator then generates torque due to the interaction between the magnetic fields of the stator and rotor. Assuming the magnets are neither heated past their Curie temperature nor physically battered, and that the hard ferromagnetic material can sustain the opposing magnetic field, then the "set" torque will be maintained by the actuator at no additional cost. The actuator only requires power to switch its magnets, in order to rotate its shaft, which happens when a pulse of current is sent through the windings. Therefore, the PPM actuator's power input (P_{in}) is directly related to the number of these pulses (N_p) required to cause a single rotation, to the energy contained in each pulse (E_p), and to the actuator's angular velocity (ω). So we can approximate the PPM actuator's consumption with the following equation:

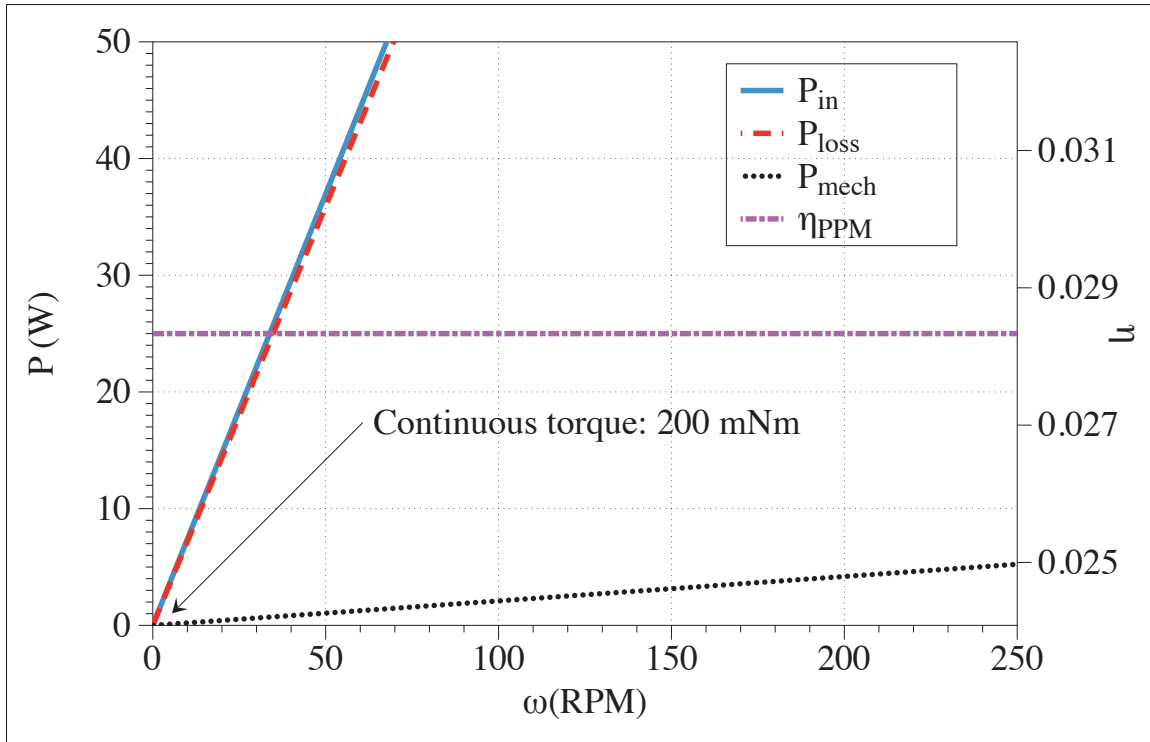


Figure 5.3 PPM actuator power characteristics

$$P_{in} = \frac{\omega}{2\pi} N_p E_p. \quad (5.3)$$

We can conclude from this equation that the power consumed by the actuator is directly proportional to how quickly the actuator rotates. The only other variable in this equation is the energy contained in each pulse E_p , since the number of pulses is fixed during the actuator design (in our case, $N_p = 4$). The amount of energy used in these pulses controls the strength of the generated magnetic fields, which results in distinct levels of torque. To summarize, by adjusting those two variables (ω and E_p), we control both the velocity and the torque produced by the actuator.

This equation also suggests that the power consumption of the PPM actuator follows a trend that is the inverse of what a conventional actuator would follow. Indeed, as can be seen from Fig. 5.2, a DC motor consumes less power as speed increases (due to back EMF), whereas our

actuator's power consumption increases linearly as a function of speed. This line crosses the origin at zero, because the actuator is able to hold a given torque indefinitely without consuming any power. This linear relationship between power input and velocity also implies a very particular efficiency profile. Indeed as we can see from eq.(5.4), the efficiency η of the actuator for a given torque is a constant.

$$\eta = \frac{P_{mech}}{P_{in}} = \frac{\tau\omega}{\omega \frac{1}{2\pi} N_p E_p} = \frac{2\pi\tau}{N_p E_p} \quad (5.4)$$

Given that our actuator's efficiency is constant, it will inevitably intersect with the efficiency curve of a conventional motor (which starts with zero efficiency at zero speed). Illustrating this phenomenon, Fig.5.4 compares the efficiency of our PPM prototype with a Maxon 339286 DC brushless motor, of very similar diameter and length. The velocity associated with point at which the two curves intersect represents the superior limit of the range of operations where our motor is always more efficient than a traditional motor. However, since efficiency is an instantaneous measurement, it may not be the best indicator of each actuator's merits for a given application. A more realistic indicator might be overall energy consumption. For example, applications like robotic grasping involve a great deal of torque-holding time. In tasks like these, the PPM actuator might consume less energy during the entire task than a conventional motor, even if it is (when rotating) occasionally less efficient than a conventional motor. The extent to which PPM actuator's efficiency is superior to a conventional motor is arguably quite limited. However, as mentioned above, our actuator is designed for low speed, high torque applications. Regarding this latter characteristic, we must point out that our actuator is able to sustain indefinitely a torque of 200 mNm when a comparable Maxon motor can only continuously produce 69 mNm.

Another consequence of this particular power consumption profile is that, unlike conventional actuators wherein heat becomes an issue when the motor needs to hold a given torque steady, our actuator will start overheating as speed increases, since increasing the speed requires sending more pulses of energy per unit of time.

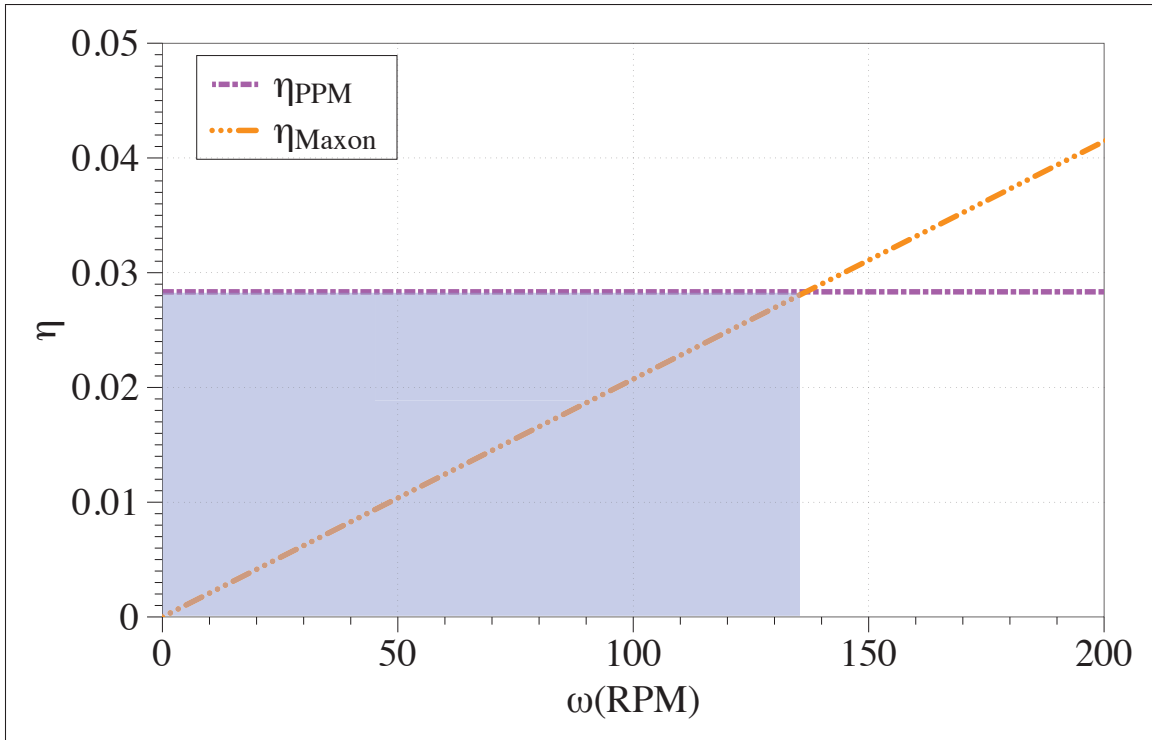


Figure 5.4 Low speed actuators efficiency comparison

5.2 The PPM actuator design

5.2.1 Recent approaches

One way to deal with the high torque demands of robots has been through static balancing, which has been promoted for increased robot compliance and human safety as well as reduced actuator power consumption (Boisclair *et al.*). Different systems such as springs (Paine *et al.* (2015)) or counter weight (Lacasse *et al.* (2013)) have been proposed to achieve it.

Another recently proposed approach is to use the electromagnetic force contained in magnets to generate passive and active torque. For example, A. Knaian created a variation of the stepper motor, the "Electropermanent" (EPM, Wikipedia, Electropermanent magnet (2017)) actuator, that uses magnets to maintain friction between the stator and rotor (Knaian (2010)). The same team also used this technology to create programmable (Gilpin *et al.* (2010)) matter and electropermanent valves in a soft robot (Marchese *et al.* (2011)). Their electropermanent actuator

relies on a pair of magnets, with one made from a softer ferromagnetic material than the other. Together they form a magnetic circuit that can be switched through the softer magnet (Alnico) to form either a closed circuit with almost no magnetic flux escaping, or an open circuit where the magnetic flux is projected outside of the arrangement of magnets. This same idea was modified for use in a drone latching mechanism, the "OpenGrab EPM" (NicaDrone website (2017)), where it enabled high payload while maintaining low power cost.

One of the limitations of using EPM in an actuator is that the arrangement of the two magnets produces a near-binary function. Indeed, the external field can practically only be turned on and off. Moreover, due to the very high coercivity of the neodymium (NdFeB) magnet, it is impossible to reverse the direction of the external magnetic field.

Our approach instead uses only one type of magnet, for which the magnetization is changed via a pulse of current in a solenoid. This enables us to "set" any amount of magnetization, in any direction, within the physical limits of the magnet's magnetization. One of the challenges with this approach is finding the right magnet. Alnico magnets, for instance, are easy to magnetize and require little energy to control, but they are also easily demagnetized (low coercivity) and can only weakly retain magnetic fields (low effective remanence). This produces a weak actuator, since a strong internal core will easily demagnetize the Alnico magnet(s).

On the other hand, some permanent magnets like NdFeB are not easily demagnetized by a strong permanent magnetic core, so they could enable a very strong actuator. However, the amount of energy required to program such a magnet is very high, making NdFeB a poor solution from the point of view of efficiency, and also one that would be difficult to implement. Thus, finding the right magnet requires finding the right trade-off between the magnet's strength and the magnetization cost.

5.2.2 Magnet Selection

Using the international notation system ¹, the relationship relationship between the magnetic flux density (B), the applied field (H), and the induced magnetization (M) is:

$$B = \mu(H + M). \quad (5.5)$$

M is a vector field expressing the permanent magnet dipole moments inside the magnet, H corresponds to the magnetic field that is applied to a ferromagnetic material in order to magnetize it, and μ is a constant such as $\mu = \mu_0\mu_r$, μ_0 and μ_r respectively being the permeability of free space and the relative permeability of the material if the magnetic flux traverses a material. Finally, B , sometimes also called magnetic field, represents the amount of magnetic flux going through a material in a unit area perpendicular to it's direction.

To fully characterize a magnet, the hysteresis curves, of whom typical examples are illustrated in Fig. 5.5, are crucial. These curves plot M and B in response to H . As a general rule, the taller these curves are, the stronger the magnet is, and the wider the curves are, the harder it is to demagnetize a magnet.

A few specific points stand out in these curves:

- The remanence, B_r , corresponds to the magnetic flux density measured when no external magnetic field is applied and after full magnetization has happened to the ferromagnetic material.
- The coercivity H_c represents the amount of external magnetic field needed to cancel the magnet's magnetic flux density.

¹ Because there are many misconceptions surrounding the field of magnetism (Sung & Rudowicz (2003)), different units, and different notations, we refer the reader to classical magnetic textbook (Cullity & Graham (2011)) and to the paper by Sung & Rudowicz (2003) for a full understanding of the misconceptions and intricacies of magnetic field theory. We will use the SI recognized *Sommerfeld* convention, and notations and only present relevant concepts.

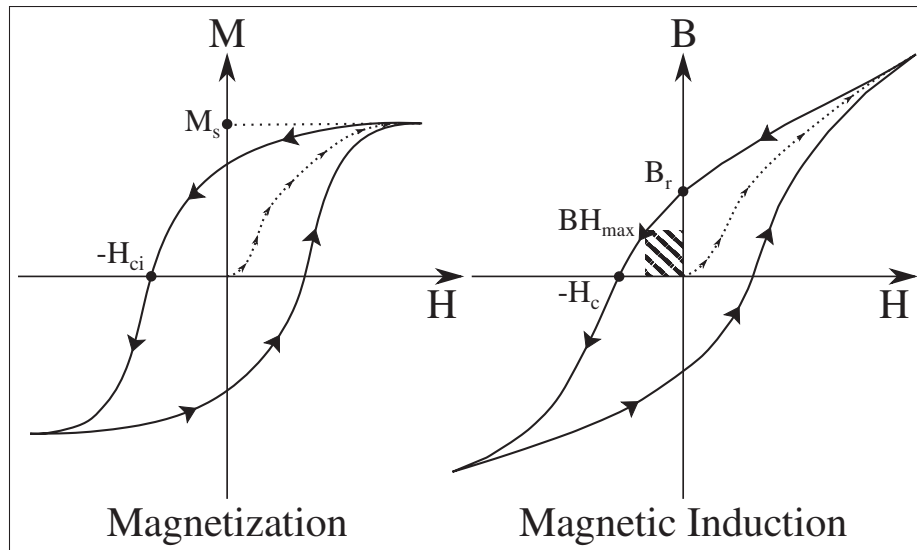


Figure 5.5 Typical ferromagnetic material hysteresis curves, independent scales.

- The intrinsic magnetization, H_{ci} , denote of the strength of magnetizing field (H) a magnet has to be subjected to in order to completely lose its magnetization (M), and is consequently directly related to a magnet energetic magnetization cost.
- The Magnetic Saturation, M_s , is the point where even if the applied field H in increased, no further magnetization of the material is possible: all the magnetic domains are aligned.
- Commonly used by the manufacturers to classify magnets, the BH_{max} is an approximate value of the maximum amount of energy stored in a magnet. It approximately corresponds to the largest rectangle under the curve, in the second quadrant of the magnetic induction graph. Since the BH_{max} does not take the magnet's shape into account.

Most of the permanent magnets used today belong to either the Aluminum-Nickel-Cobalt (Al-NiCo), Samarium-Cobalt (SmCo), or Neodymium-Iron-Boron(NdFeB) type of magnets. Each of these chemical composition grants specific characteristics in attainable remanence, coercivity and physical robustness, and can be further subdivided in many grades of magnets mainly depending on detailed chemical composition and manufacture process.

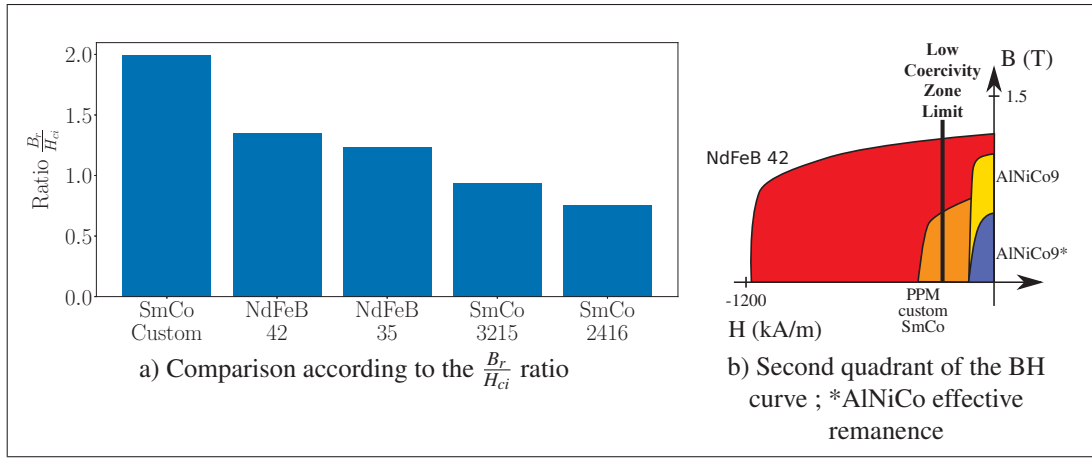


Figure 5.6 Ferromagnetic materials comparison (Dura Magnetics Website)

Since, our magnets ideally require a combination of high remanence (B_r) and low intrinsic coercivity (H_{ci}), the commonly BH_{max} is in our case inadequate. Using remanence and coercivity may lead to consider AlNiCo magnets. However, as explained before, the AlNiCo intrinsic coercivity is so weak that they cannot oppose a magnetic field without suffering demagnetization and struggle to stay magnetized when manufactured with low ratio of length over diameter. Since our magnets are as long as wide, our effective AlNiCo 9 remanence is much lower than the theoretical value and has been experimentally measured at about 0.589T, as showed by Fig 5.6b. Taking all theses parameters into consideration, we propose the following optimization function:

$$\begin{aligned} \max f(x) &= \frac{B_r}{H_{ci}} \\ \text{subject to } H_{ci} &\geq c \end{aligned} \quad (5.6)$$

where B_r is expressed in mT and H_{ci} in kA/m . According to Eq. 5.6 and as illustrated in Fig 5.6a, SmCo magnets were custom built for the PPM prototype. These magnets intrinsic coercivity is $395kA/m$, and they produce a $0.789T$ magnetic field. We do not exclude the use of some other SmCo grades in further developments.

5.2.3 Halbach magnetic circuit

5.2.3.1 Benefits

As seen above, the PPM actuator is very inefficient at high speeds. Therefore, we may want to avoid using it with a transmission gear box. If a transmission is necessary, one with a very low ratio might be preferable. To avoid the need for a transmission, we need an actuator with a very high torque-to-volume ratio, which necessitates creating a strong magnetic field within the actuator.

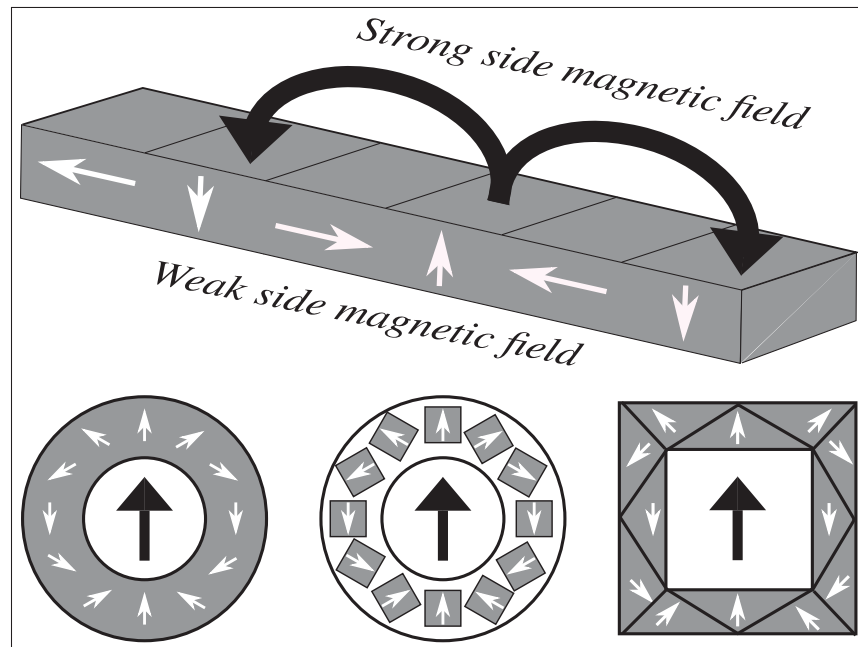


Figure 5.7 Typical Examples of Halbach arrays.

The Halbach arrays, first proposed by John Mallinson (Mallinson (1973)) and later popularized by Klaus Halbach (Halbach (1980)) are magnetic circuits that focus the magnetic flux of individual magnets to create one stronger magnetic field on only one side of the structure. ; in an either planar or circular manner as shown in Fig. 5.7. By focusing all the field in the center of the actuator, the Halbach array minimizes loss of the magnetic field outside the actuator,

which also comes with the benefit of minimizing noise that may be induced in nearby devices like sensors.

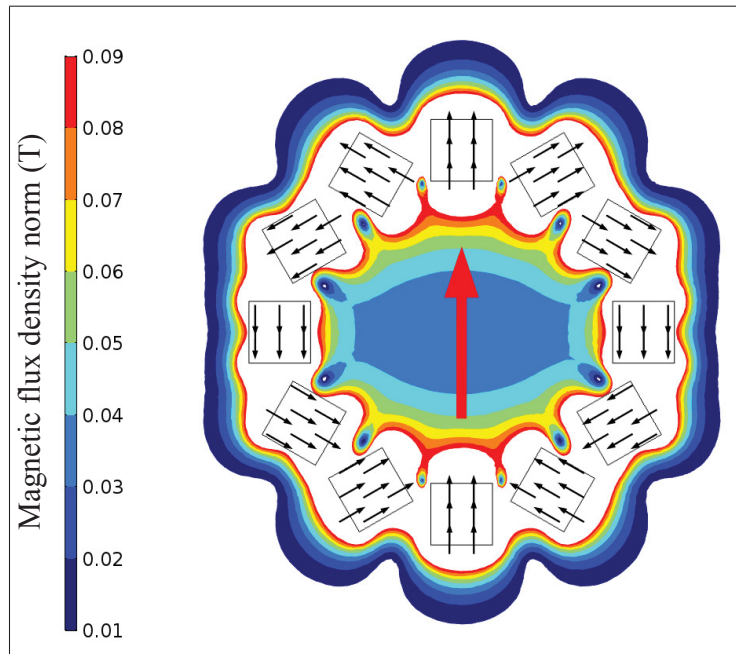


Figure 5.8 FEA magnetostatic simulation of the magnetic flux density norm (T) in one of our Halbach array.

Because they focus the magnetic flux density on only one side of the circuit and can be stacked alongside each other to further compound the magnetic field, Halbach arrays induce large magnetic fields while minimizing outer magnetic field interferences. Usual applications for these comprise Nuclear Magnetic Resonance (NMR) and particle accelerators.

As Boisclair *et al.* demonstrated, such a magnetic field also enables the generation of variable torque over large rotations of the shaft. Ideally, the torque function of the Halbach array must be as close as possible to the torque output required from the actuator. When the torque function generated by the actuator meets the robot's requirements, no additional work is needed.

In other words, if the torque needed from the PPM follows the PPM torque function, and requires an equal or inferior torque value to the PPM maximum torque output, then once the

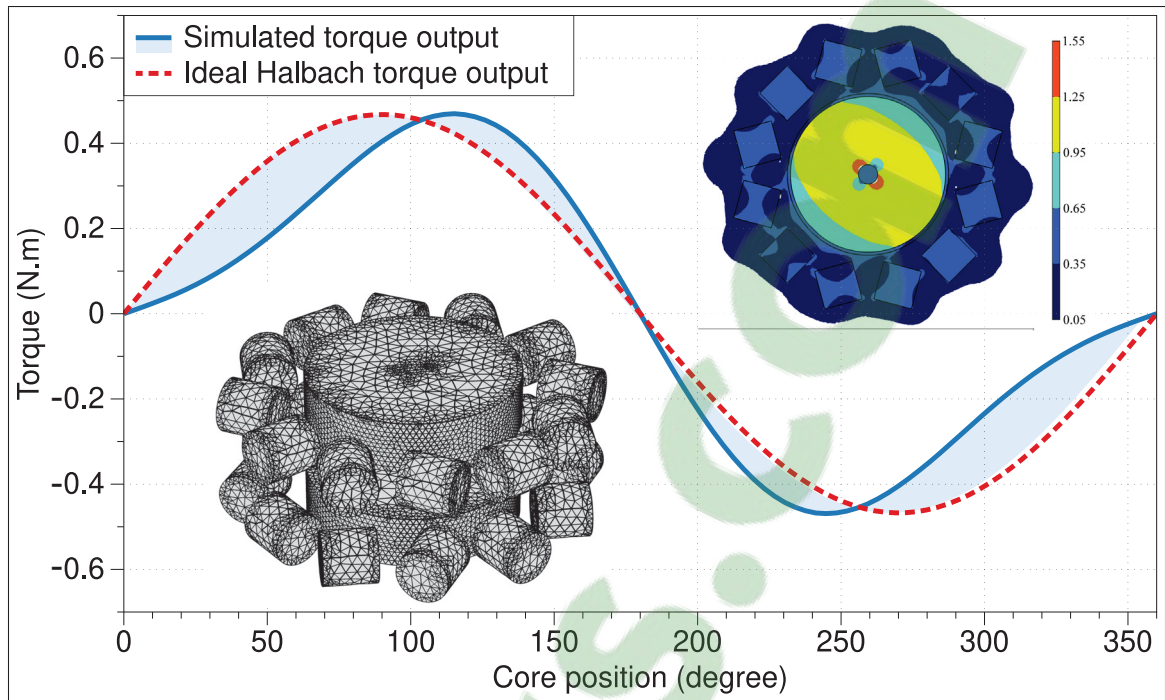


Figure 5.9 FEA maximum torque function, mesh, and magnetic flux density with core magnet.

PPM is magnetized no further energy will be required and the PPM will passively maintain the required torque.

The torque function created by our Halbach array should ideally be a sinusoid. Indeed, an actuator matching such a function satisfies the torque required by any simple one-degree-of-freedom joint operating a pendulum, one of the most essential function in actuation. Such a torque function means that the PPM actuator would exhibit a spring-like behavior when magnetized.

This function can also be modified by changing the Halbach array number of magnetic poles within the stator, to generate another torque function. Although the torque function is fixed once an actuator design is chosen, it's amplitude can be modulated by varying the magnets magnetization. A weaker magnetization will result in a similar torque function but with weaker torque. This may also be particularly useful in the fields of human prosthetic or robot legged

locomotion, where variable stiffness has been indicated as a key element for efficiency at various gaits or over different terrains (Seok *et al.* (2015)).

It has been shown that creating an Halbach array with discrete magnets rather than a single magnet of continuously changing magnetization creates a weaker magnetic field, due to increased magnetic flux leakage. Using discrete magnets is mostly for ease of manufacturing. In the context of actuators, however, the amplitude of the torque function is reduced.

Therefore, we knew our results would be worse than what is predicted for an ideal Halbach array. To find out precisely how much worse, we simulated the magnetic flux density norm using a finite element analysis (FEA) software (Comsol Multiphysics). These simulations allowed us to evaluate both the strength of the magnetic field within the Halbach array, and the amount of magnetic flux that leaked outside of it (Fig 5.8). Finally, we computed the axial torque function and compared it to the expected sinusoid function (see Fig. 5.9). Specifically, we simulated the motion of the magnets in the rotor while the stator is fully magnetized, and we obtained the PPM actuator's theoretical max torque output for one turn of the core magnets.

5.2.3.2 Design

Halbach arrays are frequently presented as a single magnet of continuously changing magnetization. However, for cost and practicality reasons, Halbach arrays are often assembled using discrete magnets. In that case, the magnets orientation must be changed according to the Halbach's required magnetization. Using a large number of magnets yields closer approximation and lower magnetic flux leakage (Raich & Blümler (2004); Soltner & Blümler (2010)).

The design of Halbach arrays has been the subject of a large number of papers ranging from dimensions optimization (Bjørk *et al.* (2010); Bjørk (2011)), coercivity and demagnetization (Bjørk *et al.* (2015); Insinga *et al.* (2016)) or torque analysis (Bjørk *et al.* (2010)). Since our Halbach arrays are made of discrete magnets, presented in Section 5.2.2, we will use the notation from papers from Raich & Blümler (2004) and Soltner & Blümler (2010) to describe magnet's positions and magnetization direction.

The vector position ${}^c\mathbf{p}_i$ of the Eq. 5.7 describes the positions of the centers of the i^{th} among n magnets in a circular Halbach array of radius r . The position of each magnet depends the number of magnets used. Thus β_i describes the angles between the i^{th} magnets centers and the Y-axis from the Cartesian coordinates as described in by Fig 5.10. The magnets orientation is described by γ_i between the same Cartesian Y-axis and the magnets own reference axes.

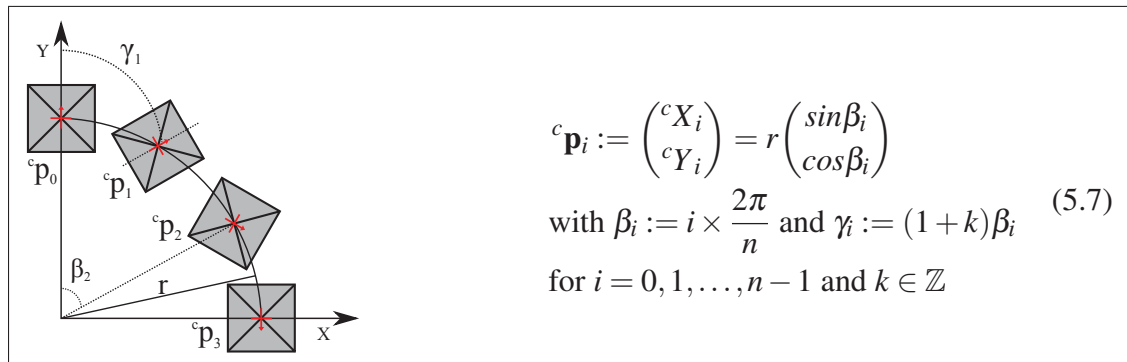


Figure 5.10 Halbach magnet positioning and orientation equations, with schematic of a quarter of a Halbach array with $n = 12$ and $k = 1$.

The number k determines both the number of pole pairs created by the Halbach array and the side on which the magnetic field will be present. For $k = 1$, a unique magnetic pole pair is created inside of the cylinder, while if $k = -2$, two pole pairs will be created outside of the cylinder. The PPM actuator is built using two Halbach arrays ($k = 1$ and $n = 12$), each creating a single internal magnetic dipole.

The arrays are aligned vertically but separated by 4.25mm and phase shifted by 90 degrees. Using two shifted arrays allows to control the actuator rotation direction by selectively switching one Halbach array's magnetization after the other, making the shaft turn by 90 degrees every time.

5.2.4 Actuator prototype

The actuator has two main components – stator and rotor – each of which is composed of permanent magnets. The stator is composed of two Halbach arrays, which are superposed and

separated by 4.25 mm. In order to maximize the strength of the generated magnetic field, we want to maximize the amount of magnetic material for a given volume of the PPM actuator. Consequently, we want to minimize the distance between each magnet – both within the Halbach arrays, and between the magnets of the arrays and the rotor.

Given that the Halbach array configuration dictates that the magnets have a certain orientation (see Fig. 5.10), in order to maximize the amount of magnet per unit of volume, we had to use relatively short magnets. The custom-made magnets used in the Halbach arrays are cylinders of 6.35 mm (0.25”) in diameter and height, which are magnetized through the length.

The rotor in our actuator is comprised of two hollow cylindrical magnets that are made of high-grade ferromagnetic material (N42 NdFeB) and are magnetized diametrically. These two magnets are also superposed and separated by 4.25 mm. Each magnet has the following dimensions: 25.4 mm (1”) in diameter, with a hollow center of 3.175 mm (0.125”) in diameter, and height of 6.35 mm (0.25”).

Each Samarium-Cobalt magnet is wrapped in a handcrafted two layer solenoid made of AWG30 wire ($N \approx 32$). The solenoids then are wired one after the other in a serial manner. The typical electrical characteristics of the solenoids and of the Halbach arrays as measured at $1kHz$ by a LCR meter (BK precision 878B) are:

$$\begin{cases} L_s \approx 7.2\mu H \\ R_s \approx 0.29\Omega \end{cases} \quad \begin{cases} L_H \approx 88\mu H \\ R_H \approx 3.5\Omega \end{cases} \quad (5.8)$$

The electrical circuit of the PPM is composed of a bank of 44 capacitors (42 ceramic Stac-kiCap 2220-1K20224-X-WS2, $0.22\mu F$ each ; two film capacitor MKP1847, $3\mu F$ each, total measured capacitance: $15.4\mu F$). The capacitors discharge in each Halbach Array through a solid state switch (thyristor). For manufacturing simplicity, each Halbach array coils are wired independently and soldered onto intermediary printed circuit boards (PCBs) placed in the stator. Both these PCBs are then wired to a larger PCB holding the motor, capacitors and thyristors and designed to integrate into a Robotiq gripper. The motor, the capacitor bank and

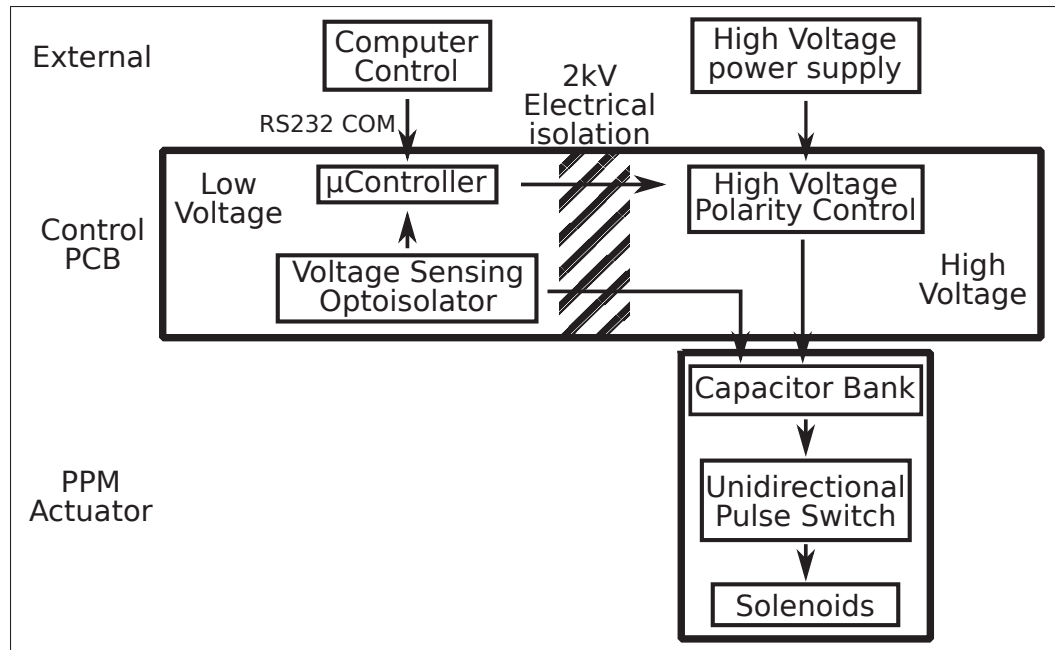


Figure 5.11 General system diagram.

the thyristors are placed on a printed circuit board (PCB) designed to integrate fully into a Robotiq gripper.

The capacitors charge and thyristor activation are operated by an external PCB, controlled by a computer through the RS-232 communication protocol. This PCB is wired to an external high voltage, high current power supply (Iseg, HPP 20 407) and regulates both the capacitors voltage and polarity. The full system's operation is illustrated in Fig. 5.11.

The motor stator is divided into two parts that have been 3-D printed (Zortrax M200), the coils and magnets are then fixed inside and the assembly is fixed using flat bearings and non-conductive screws. The complete motor with capacitors weighs about 200 grams.

The prototype was successfully integrated in a commercially available two finger Robotiq hand. When used in a Robotiq two finger gripper, our prototype generated enough torque to open and close the under-actuated robotic hand, allowing to grasp various objects as demonstrated in Fig 5.12.

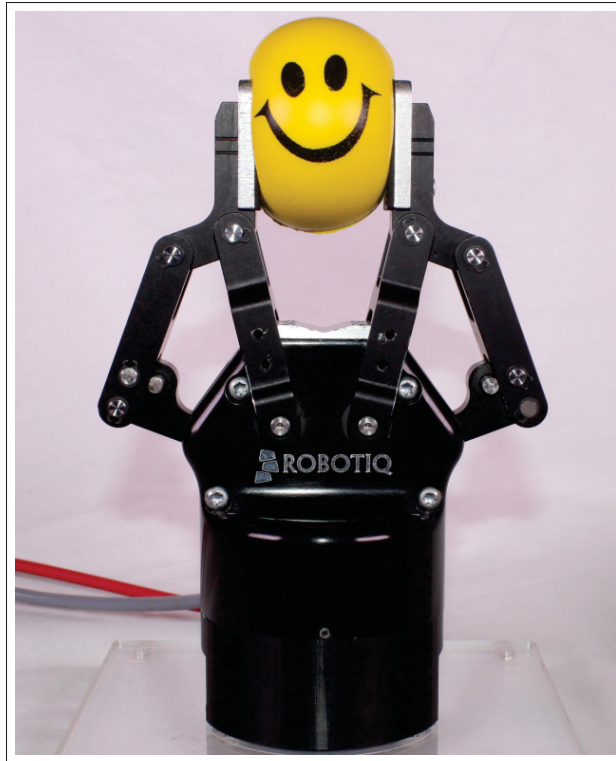


Figure 5.12 Robotiq 2-finger gripper with PPM motor grabbing a stress ball.

5.3 Experimental results

5.3.1 Actuator torque output

The PPM actuator's torque output, as a function of the capacitor's pulses is plotted in Fig. 5.13. Each point represents the mean between five experimental values captured 10cm from the shaft rotation center, by a force gauge (Mark 10, M4-10) and expressed in N.m. The maximum torque is about 0.2N.m.

The torque theoretical (Fig 5.9) and experimental (Fig 5.13) maximum values are in good agreement (0.22 N.m and 0.2 N.m), slight disparities probably being due to unaccounted ferromagnetic material in the simulation (bearings, shaft), and imperfections in the magnets. Thanks to these results, we believe the shape of both numerically computed and experimental torque

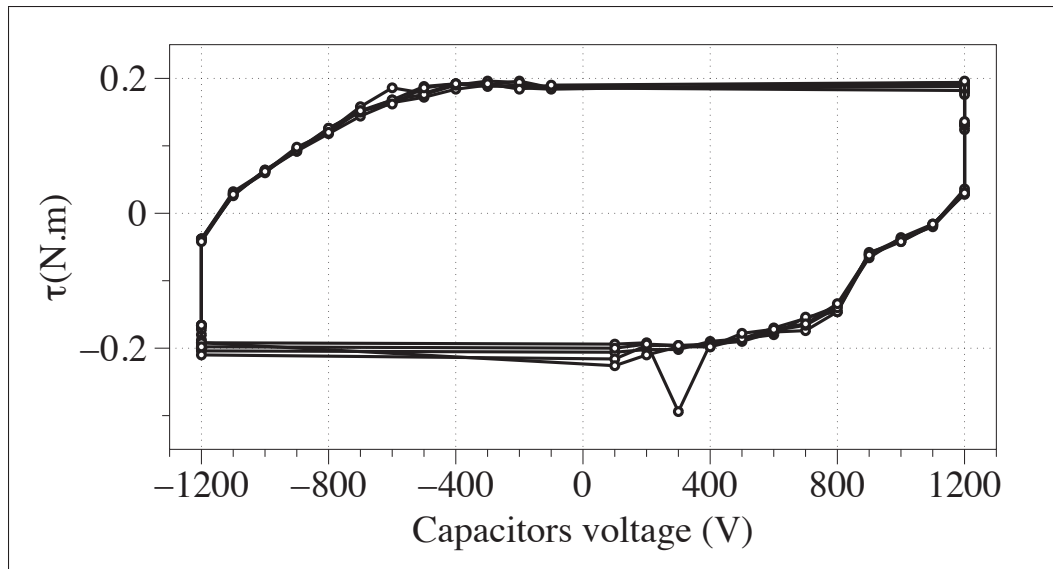


Figure 5.13 Experimental actuator torque as a function of capacitors terminal voltage.

functions to correspond closely. This function is of great importance when using the actuator to generate passive torque.

5.3.2 Halbach magnetic flux density

Experimental results of the magnetic field density generated by the Halbach array are shown in Fig. 5.14. As the capacitors pulses magnetize the Halbach array, the magnetic flux density is directly related to the capacitors voltage before discharge.

Maximum and minimum values of magnetic flux density, in Fig. 5.14, were logged autonomously by the microcontroller, after ten pulses at 100V interval, at the center of one of the two Halbach arrays, with a hall effect sensor (SS495A, Honeywell), no applied external field, and through five complete magnetization cycles. The Halbach array was manually demagnetized and remagnetized for five cycles in order to evaluate the Halbach's initial magnetization.

This is why the curve resemble, in shape, to a magnetization curve as presented earlier in Fig. 5.5. The magnetic flux density was logged autonomously by the microcontroller, from the

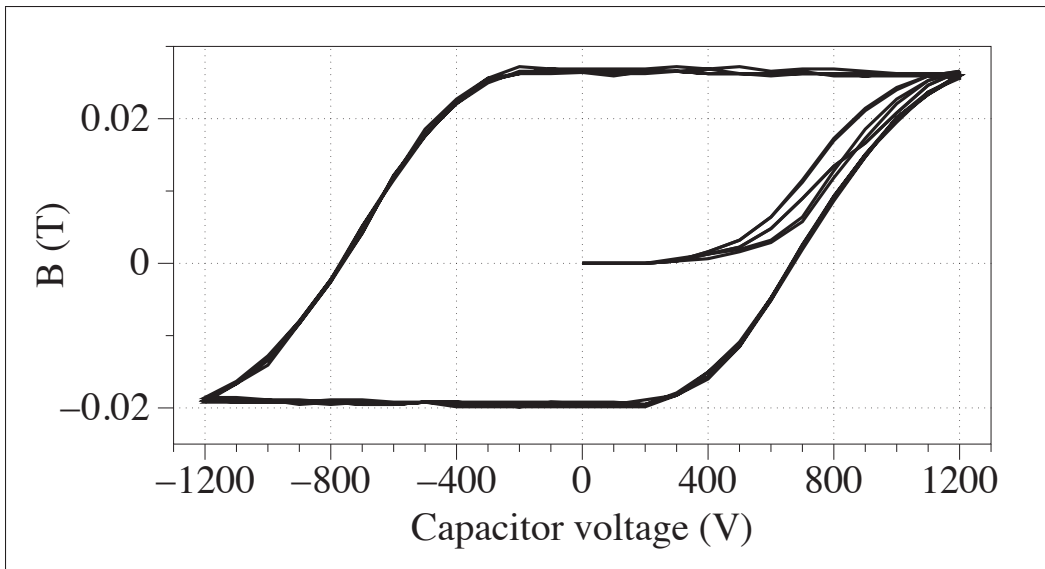


Figure 5.14 Experimental Halbach array magnetization curve.

center of the Halbach array with a hall effect sensor (SS495A, Honeywell) and through five complete magnetization cycles.

5.3.3 Pulse characterization

The magnetic field switching requires the generation of large magnetic fields in the ferromagnetic material. However, these magnetic fields only have to be maintained during very short periods of time (in the order of nanoseconds) for the magnets magnetic domains to align.

As evidenced by the Hysteresis curves shown before in Fig. 5.5, the applied magnetic field needed to magnetize a magnet depends both on the magnet's coercivity and its previous magnetic state. Strong pulses are required when the stator was previously strongly magnetized or if the ferromagnetic is very hard to magnetize. We experimentally found that rotating the actuator with the lowest number of pulses, regardless of the previous state of magnetization of the magnets, requires the capacitors to be charged to at least 1150V.

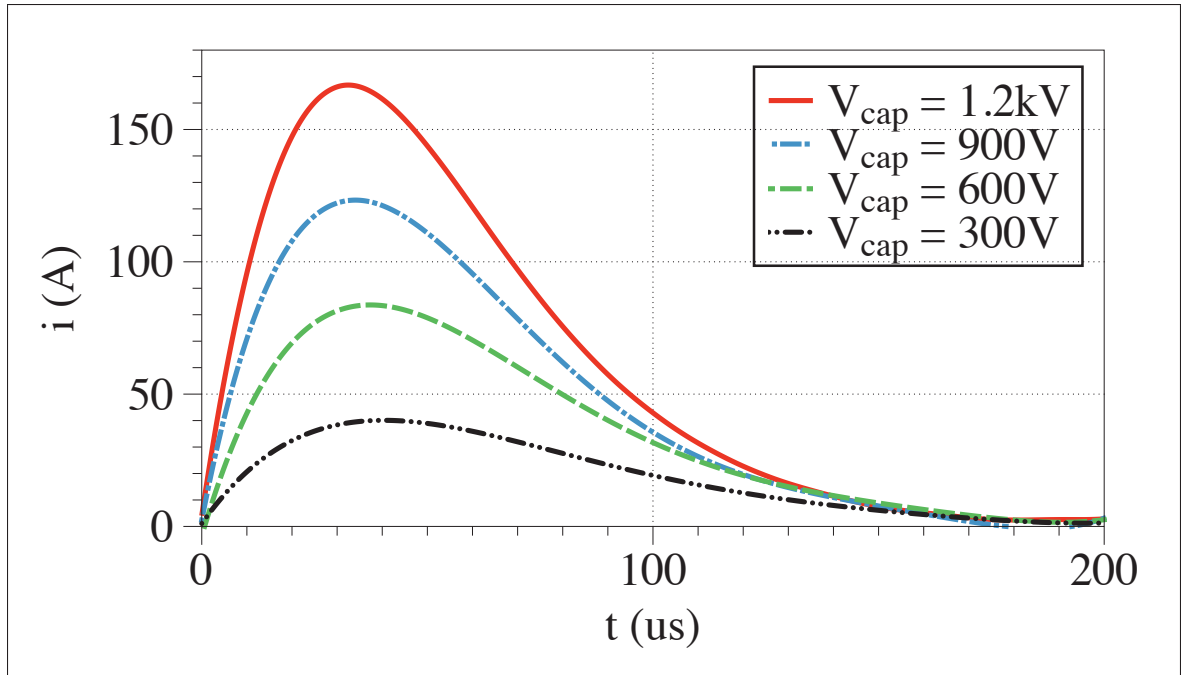


Figure 5.15 Current pulses in a single Halbach array, depending on capacitors terminal charge voltage.

Fig. 5.15 shows the experimental current pulses in one Halbach array and charging the capacitors at different voltages. The pulse was captured with an oscilloscope (Tektronix TDS 1002B) through a rogowsky current waveform transducer (Powertek CWT 6B, 5mV/A sensitivity).

Based on the current generated by the pulses (i), and using the number of wire turns in the solenoid (N), and the solenoid length (l) and diameter (d), we can estimate the applied magnetic field (H) at the magnet's center in a solenoid of equal length and diameter ($d \approx l$),

$$H = \frac{Ni}{l} \times \left[\frac{l}{\sqrt{l^2 + d^2}} \right] \approx \frac{Ni}{l\sqrt{2}} \quad (5.9)$$

Since multiple layers of wires are used, the Eq.5.9 only serves as an approximation. Using Eq. 5.9, a 1.2 kV charge of the capacitors, creating a 168 A current pulse, generates an applied magnetic field of approximately 598 kA/m, which is consistent with our magnet characteristics.

Since that multiple layers of wires are used in our solenoids, the magnetic field generated cannot be assumed uniform, and the Eq.5.9 is only a crude approximation. Since our solenoids used to magnetize ferromagnetic material, it is actually more relevant to compute the applied magnetic field (H) rather than the magnetic flux density (B).

The energy contained in the capacitors is given by the Eq. 5.10. The energy contained in capacitors depend on their voltage and capacitance such as

$$E_p = \frac{1}{2}CV^2 \quad (5.10)$$

Since the capacitance is constant, it is the capacitor's voltage that dictates the energy of a pulse. Based on Eq. 5.10, the energy contained in the most powerful pulse is obtained by charging the capacitors at 1200V, and contains approximately 11.1 Joules.

In order to minimize weight and volume, a measure of capacitors energy density seems reasonable. The ceramic capacitors are capable of storing approximately ten times more energy per unit of volume than the Vishay film capacitors, and are easier to fit inside a given space. However, other factors such as safety, over voltage resistance, and peak current capability, are important too. In all these factors, the film capacitors are superior to the ceramic capacitors.

Although storing energy in capacitors is required for the generation of these current pulses, considering the voltages and currents involved, we think it is necessary to emphasize that **one should take appropriate safety measures before trying to reproduce any of this work.**

CONCLUSION AND RECOMMENDATIONS

If you meet the buddha, kill him.

Linji

This thesis explored both sensing and actuation with the goal of improving prosthetics. Prostheses capabilities are still far inferior to biological members, and as a consequence the loss of a limb, even when replaced by a prosthesis, is an important disability. By improving prostheses, this thesis aimed at ameliorating people's quality of life.

Prosthetics are complex devices, and their adoption by amputees is driven by a large number of criteria such as financial, aesthetic, functional and health related. As engineers, we can only address a subset of these issues, and among them, we identified and focused on problems reported as most important by recent studies.

The main reported issues for upper limb prosthetics included heat generation and excessive weight as well as lack of both dexterity and sensory feedback. We proposed that these belonged mostly to two research problems, **sensing** and **actuation**, which we decided to tackle respectively in Part I and Part II.

For each of these parts, the present conclusion will reframe this thesis work among the corresponding research fields and industries, present the main thesis contributions, and then finally expand on future innovations. By doing this, we hope to give the reader both a good understanding of the context by which this research was conducted, as well as insights on possible developments.

6.1 Microfluidic sensing

6.1.1 Reframing contemporary microfluidics

The research field of Microfluidics was employed in this thesis as a soft alternative to conventional microelectronics. However, this research field was actually born out of very different motivations. Microfluidics was first motivated by chemical analysis at small scales, followed by chemical and biological threat assessments, molecular biology, and more recently soft microelectronics (Whitesides (2006)).

The need for softer microelectronics is motivated by the shrinking in size of computing power. This is driving the current trend and expectations for technological devices to move from portable to wearable. However, modern microelectronics are still largely based on semiconductors and conductors such as silicon, copper or gold; materials that are neither flexible nor stretchable.

Biological structures are compliant and often convex. As a result there is a need for softer and more adaptative devices, leading both sensing and computation to being redesigned with new materials in order to create softer devices. Microfluidics is one of the avenues being actively explored as an alternative to conventional microelectronics. Such devices are expected to find use in collaborative robotics, virtual reality, and wearable devices.

As this thesis was concerned by the design and manufacture of microfluidic sensors for ULPs proprioception, and it is thus inscribed in the larger trend toward soft microelectronics for computation and sensing.

Since large scale consumer flexible and stretchable computation is not yet available, designing soft and stretchable sensors today is really tackling two problems, both of which can be solved through a variety of techniques:

1. The design and manufacture of a soft sensor, ideally soft and stretchable, easy to measure as well as cheap and simple to manufacture.
2. The reliable connection of a soft structure (the sensor) with a harder one (the computation device).

Among all the soft sensors present on the market or in the literature, microfluidics sensors can probably boast to be the some of the softest and of the most stretchable. Indeed, microfluidics sensors often are designed by embedding liquids in polymers. As polymers have incredible elasticity and softness, and liquids being in many ways the ultimate stretchable and self healing material, the alliance of both may yield incredibly compliant sensors.

In spite of all these advantages, microfluidic sensors also have unfavorable characteristics. They are notably hard to manufacture as most liquids cannot hold a fixed shape. As a consequence, three dimensional, micro, and nano-structures can necessitate many steps to be fabricated.

Additionally, the interconnects between liquid sensing elements and silicon based computation, oftentimes metal, can be the cause of leaks. As the hardness between materials differ spectacularly and because of the mechanical deformations created during use, either a very strong bond or a large surface is needed at the interface between the materials to prevent tears.

In the first part of this thesis we used soft polymers embedded with microfluidic channels in order build a single axis strain sensor, then a force sensitive skin, and finally a wearable artificial skin for hand motion detection. That hand motion detection wearable skin can be adapted to measure the configuration of prosthesis, with minimal alterations to the overall design.

6.1.2 Recommendations on microfluidic sensing

Looking back, the technologies we use today may seem obvious choices. There was, however, a time where the magnetic hysteresis of ferrites cores was used in order to build logic circuits. Nowadays, almost every logic circuit uses transistors. As much as innovative ideas are vital, oftentimes it's the ability for large scale production that determines their use in the world.

The future of soft sensing probably resides not only in the sheer capabilities of the sensors, but also in our capability to produce them reliably, at the dimensions needed, and at large scale. This reality has been well understood by the microfluidics community, and many papers address this issue.

6.1.2.1 Liquids for microfluidics

In that respect, the use of eGaIn has been particularly successful as the oxide skin covering the liquid (when in contact with air) grants the ability to create self standing 3-D structures during manufacture (Kramer *et al.* (2013); Joshipura *et al.* (2015); Lu *et al.* (2017)).

Although low temperature melting alloys such as eGaIn exhibit very good conductivity and ease the fabrication process, many other liquids also exist. Much like silicon can be doped to create n or p-type junctions, achieving meaningful microfluidic circuits and sensors may require the use of liquids of widely different characteristics. Fortunately, as we showed in this thesis, conductive liquids such as room temperature ionic liquids can be tailored to offer a wide variety of properties such as ionic conductivity (Bonhote *et al.* (1996)), biocompatibility (Wei & Ivaska (2008)), or ferromagnetism (Hayashi *et al.* (2006)), making them potentially suitable for many different types of sensors.

Fluids of higher viscosity (gels), may also represent yet another an attractive option. Indeed, similarly to eGaIn, higher viscosity may ease manufacturing, while in the same time provide

further customization opportunities of the liquids thanks to the inclusion of nano-particles in suspensions (Wang *et al.* (2003); Tee *et al.* (2012)).

6.1.2.2 Interconnects for microfluidics

Finally, connecting these different liquids either together, with conventional microelectronics, or with stretchable electronics, will require the use of soft conductive materials. Different approaches are currently being pursued, the first being probably the use conventional rigid materials in curved designs. These, oftentimes called "wavy" structures, supported by soft substrates allow for an increased flexibility and stretchability.

Polymers doped with conductive nano-particle may be another avenue. Polymers are already the material of choice for many microfluidic devices, and by localized doping with nano-particles, one can modify both their mechanical and electrical properties.

Last of the interconnects alternatives, organic materials have been the focus of much research. Obeying to Van der Waals forces rather than the stronger atomic covalent bond of inorganic materials (such as metals), organic electronics have already demonstrated their ability for the manufacture of soft and stretchable electronics (Forrest (2004); Someya *et al.* (2016)). Organic materials may very well replace completely conventional electronics in design where stretchability is vital

6.2 Prosthetic actuation

6.2.1 Prosthetic and robotic actuation

Since the industrial revolution, assembly line robots have been tasked with the jobs described as the three "Ds": dirty, dull and dangerous. These robots are mostly designed for speed and precision, however, motivated by societal needs such as population aging, automation is

expanding to new environments. Using robots in different settings requires new attributes from the the robots, thus fostering further research. Soft and collaborative robotics are good examples of such recent trends in robotics.

Collaborative robotics essentially aims at making robots easier and safer to interact with so that they can be deployed alongside humans, while also operating on a larger set of tasks. Soft robotics, as the name implies, pursues the design of robots through soft structures. Soft robotics incentives mainly lie in healthcare applications such as minimally invasive surgery or rehabilitation. Active prosthetics, especially when battery powered, fundamentally share many characteristics with these two fields.

Actuation, is not only a necessary component of robots and prosthetics, it also constitutes an important part in terms of energy expenditure and monetary cost (Seok *et al.* (2015)). It then logically follows that special interest should be taken in the design of actuators for robots and prosthetics.

Robots and prosthetics are, to this day, mostly driven through different types of electromagnetic actuators, of which the most common are DC and brushless motors. Indeed, these actuators, first discovered in the 1830s, are well understood and can be very efficient at high speed. However, as we demonstrated in this thesis, tasks such as grasping are ill suited for conventional electromagnetic motors to be used, and the result of such inefficiency is excessive heat generation.

As heat generation limits the actuators capabilities, a strategy can be to radiate heat through liquid cooling, thus enabling higher maximum peak torque characteristics from the actuators (Urata *et al.* (2008, 2010); Kozuki *et al.* (2016); Hochberg *et al.* (2013)). Yet another may be to conceive electromagnetic actuators better suited for a specific application (Seok *et al.* (2015); Wensing *et al.* (2017)).

Subscribing to this second strategy, we demonstrated the design, manufacture, and integration of a new type of electromagnetic actuator in the second part of this thesis. This unique actuator, named the "Programmable Permanent Magnet" (PPM) actuator, requires energy only when rotating or changing its torque output. In other words, this actuator generates torque without consuming current or voltage, and this without using any mechanical locking system or gearbox.

6.2.2 Recommendations for the PPM actuator

The electropermanent actuator exhibits characteristics that set him apart from other electromagnetic actuators. The prototype manufactured, although sufficient to demonstrate the working principles, is still far from being optimized and there are many opportunities for future work.

First, a further increase in efficiency can be reached by improving the electrical circuit. Since both the total capacitance and the inductance play a role in the pulse speed, by balancing these values we expect to generate faster, more efficient pulses. The equivalent inductance can be lowered by placing the solenoids in parallel or by modifying the solenoid manufacture. The capacitance can be lowered by removing capacitors or connecting them in series, making the actuator smaller and lighter.

Actuator efficiency is a common measure used to gauge the capability of an actuator to transform electrical energy into mechanical energy. Electromagnetic magnetic fields are transient in conventional electromagnetic actuators. Therefore, a conventional actuator efficiency represents its ability to convert electrical energy in mechanical energy, at a given point in time.

In the PPM actuator, the electrical energy is used to generate and then store electromagnetic fields in magnets. Since storing electromagnetic fields in hard ferromagnetic material is by definition a dissipative process, and that the measure of efficiency relies on an instantaneous measure of power, our PPM efficiency appears very low.

A better comparison of the different types of electromagnetic actuators may be obtained by comparing electromagnetic actuators energy expenditure for a given task. Simple reproducible measures could be acquired as different actuators operate to create the same torque-speed output for comparable period of time. We expect the PPM to comparatively use much less energy than conventional actuators for tasks requiring constant torque at no speed, or very low speed and large torques.

The solid states switches used (thyristors), although known for they ability to handle large currents, are also hard to control. The use of power IGBT or Sic-Mostfets transistors may bring better control on the pulse and faster latching times.

Increasing the pulse voltage is theoretically and for efficiency purposes, always a good idea. It can be achieved in a number of ways, one of which being charging all capacitors in parallel but discharging in series. This can be done through a special voltage multiplication electrical circuit called a Marx generator. Doing so, however, increases the risks of electric arcs in the actuator.

The overall use of better materials overall should improve the actuator's reliability. High speed PCBs, plastic bushings, better component placement and better isolation between electrical components may help with electric arcs. Ultimately, custom made film capacitors may also further reduce the actuator size.

A better and more complete FEA model, with current pulses and non linear magnetization, would be extremely useful. This would permit to model the complete behavior of the actuator, from current pulse to torque output. In a second time, the model could be used for optimization under constrains, leading to insights on either actuator optimal dimensions or alternative architectures.

Key parameters for the model to adjust would be: the actuator overall size, the number of magnets, the number of magnetic poles from both the Halbach array and the core magnet, the ratio of the Halbach array external on internal radii, and finally the number of Halbach stages, as well as the space separating them vertically. Indeed, depending on the application targeted, the number of Halbach array stages as well as the number of magnetic poles can be adjusted to change to actuator torque function.

Finally, although the PPM actuator is designed for constant torque generation, other applications may require efficiency at both high and low rotational speed. In these cases, a hybrid between a conventional electromagnetic actuator (DC or brushless) and the PPM actuator may then be relevant. A conventional actuator would grant the hybrid actuator efficiency in high speed low torque conditions, added peak torque when necessary, improved bandwidth for fast actuation, and increased control for smoother shaft rotations.

Applications of the PPM actuator are anticipated for prosthetic and robotic actuation, and in general in the field collaborative robotics. Tasks such as grasping and walking seem especially suited to be fulfilled by the PPM actuator, but we hope to see the PPM actuator used in other applications.

Clicours.COM

BIBLIOGRAPHY

- Abraira, V. E. & Ginty, D. D. (2013). The sensory neurons of touch. *Neuron*, 79(4), 618–639.
- Alder, A. & Lionheart, W. R. B. (2006). Uses and abuses of eiders: an extensible software base for eit. *Physiological measurement*, 27, S25-S42.
- Atkins, D. J., Heard, D. C. & Donovan, W. H. (1996). Epidemiologic overview of individuals with upper-limb loss and their reported research priorities. *Jpo: Journal of prosthetics and orthotics*, 8(1), 2–11.
- Baldyga, J., Orciuch, W., Makowski, L., Malik, K., Özcan-Taskin, G., Eagles, W. & Padron, G. (2008). Dispersion of nanoparticle clusters in a rotor-stator mixer. *Industrial & engineering chemistry research*, 47(10), 3652–3663.
- Bianchi, M., Salaris, P. & Bicchi, A. (2012). Synergy-based optimal design of hand pose sensing. *Intelligent robots and systems (iros), 2012 ieee/rsj international conference on*, pp. 3929–3935.
- Biddiss, E., Beaton, D. & Chau, T. (2007). Consumer design priorities for upper limb prosthetics. *Disability and rehabilitation: Assistive technology*, 2(6), 346–357.
- Biddiss, E. A. & Chau, T. T. (2007). Upper limb prosthesis use and abandonment: a survey of the last 25 years. *Prosthetics and orthotics international*, 31(3), 236–257.
- Bjørk, R. (2011). The ideal dimensions of a halbach cylinder of finite length. *Journal of applied physics*, 109(1), 013915.
- Bjørk, R., Smith, A. & Bahl, C. R. H. (2010). Analysis of the magnetic field, force, and torque for two-dimensional halbach cylinders. *Journal of magnetism and magnetic materials*, 322(1), 133–141.
- Bjørk, R., Smith, A. & Bahl, C. (2015). The efficiency and the demagnetization field of a general halbach cylinder. *Journal of magnetism and magnetic materials*, 384, 128–132.
- Boisclair, J., Richard, P.-L., Laliberte, T. & Gosselin, C. Gravity compensation of robotic manipulators using cylindrical halbach arrays. *Ieee/asme transactions on mechatronics*.
- Bonhote, P., Dias, A.-P., Papageorgiou, N., Kalyanasundaram, K. & Grätzel, M. (1996). Hydrophobic, highly conductive ambient-temperature molten salts. *Inorganic chemistry*, 35(5), 1168–1178.
- Butterfaß, J., Grebenstein, M., Liu, H. & Hirzinger, G. (2001). Dlr-hand ii: Next generation of a dextrous robot hand. *Robotics and automation, 2001. proceedings 2001 icra. ieee international conference on*, 1, 109–114.
- Carrozza, M., Eisinberg, A., Menciassi, A., Campolo, D., Micera, S. & Dario, P. (2000). Towards a force-controlled microgripper for assembling biomedical microdevices. *Journal of micromechanics and microengineering*, 10(2), 271.

- ChemSpider. (2014). 1-Ethyl-3-methylimidazolium Ethyl Sulfate. [Online; (accessed 17:11, Nov 4, 2014), Consulted at CSID:16144279, <http://www.chemspider.com/Chemical-Structure.16144279.html>].
- Chen, X., Lotshaw, W., Ortiz, A., Staver, P., Erikson, C., McLaughlin, M. & Rockstroh, T. (1996). Laser drilling of advanced materials: effects of peak power, pulse format, and wavelength. *Journal of laser applications*, 8(5).
- Cheng, S. & Wu, Z. (2011). A microfluidic, reversibly stretchable, large-area wireless strain sensor. *Advanced functional materials*, 21(12), 2282–2290.
- Cheung, E. & Lumelsky, V. (1992). A sensitive skin system for motion control of robot arm manipulators. *Robotics and autonomous systems*, 10(1), 9–32.
- Cheung, E. & Lumelsky, V. J. (1989). Proximity sensing in robot manipulator motion planning: system and implementation issues. *Ieee transactions on robotics and automation*, 5(6), 740–751.
- Cheung, Y.-N., Zhu, Y., Cheng, C.-H., Chao, C. & Leung, W. W.-F. (2008). A novel fluidic strain sensor for large strain measurement. *Sensors and actuators a: Physical*, 147(2), 401–408.
- Chossat, J.-B., Park, Y.-L., Wood, R. & Duchaine, V. (2012). A soft elastomer strain sensor based on an gain/ionic solution hybrid construction.
- Chossat, J.-B., Park, Y.-L., Wood, R. J. & Duchaine, V. (2013). A soft strain sensor based on ionic and metal liquids. *Ieee sensors journal*, 13(9), 3405–3414.
- Chossat, J.-B., Shin, H.-S., Park, Y.-L. & Duchaine, V. (2015a). Soft tactile skin using an embedded ionic liquid and tomographic imaging. *Journal of mechanisms and robotics*, 7(2), 021008.
- Chossat, J.-B., Tao, Y., Duchaine, V. & Park, Y.-L. (2015b). Wearable soft artificial skin for hand motion detection with embedded microfluidic strain sensing. *Robotics and automation (icra), 2015 ieee international conference on*, pp. 2568–2573.
- Chung, H., Jang, S., Ryu, H. & Shim, K. (2004). Effects of nano-carbon webs on the electrochemical properties in lifepo₄c composite. *Solid state communications*, 131(8), 549–554.
- Cignoni, P., Callieri, M., Corsini, M., Dellepiane, M., Ganovelli, F. & Ranzuglia, G. (2008). Meshlab: an open-source mesh processing tool. *Eurographics italian chapter conference*, 2008, 129–136.
- Cobos, S., Ferre, M., Uran, M. S., Ortego, J. & Pena, C. (2008). Efficient human hand kinematics for manipulation tasks. *Intelligent robots and systems, 2008. iros 2008. ieee/rsj international conference on*, pp. 2246–2251.

- Cullity, B. D. & Graham, C. D. (2011). *Introduction to magnetic materials*. John Wiley & Sons.
- Cutkosky, M. R., Howe, R. D. & Provancher, W. R. (2008). Force and tactile sensors. In *Springer Handbook of Robotics* (pp. 455–476). Springer.
- da Silva, A. F., Goncalves, A. F., Mendes, P. M. & Correia, J. H. (2011). FBG sensing glove for monitoring hand posture. *Ieee sens j.*, 11(10), 2442-2448.
- Dargahi, J. & Najarian, S. (2005). Human tactile perception as a standard for artificial tactile sensing- a review. *The international journal of medical robotics and computer assisted surgery*, 1(1), 23–35.
- Dickey, M. D., Chiechi, R. C., Larsen, R. J., Weiss, E. A., Weitz, D. A. & Whitesides, G. M. (2008). Eutectic gallium-indium (egain): A liquid metal alloy for the formation of stable structures in microchannels at room temperature. *Advanced functional materials*, 18(7), 1097–1104.
- Ding, T., Wang, L. & Wang, P. (2007). Changes in electrical resistance of carbon-black-filled silicone rubber composite during compression. *Journal of polymer science part b: Polymer physics*, 45(19), 2700–2706.
- Dipietro, L., Sabatini, A. M. & Dario, P. (2008). A survey of glove-based systems and their applications. *Ieee transactions on systems, man, and cybernetics, part c (applications and reviews)*, 38(4), 461–482.
- Dobrzynski, M., Pericet-Camara, R. & Floreano, D. (2011). Contactless deflection sensor for soft robots. *Intelligent robots and systems (iros), 2011 ieee/rsj international conference on*, pp. 1913–1918.
- Doppelbauer, M. The invention of the electric motor 1800-1854. Accessed: 2017-08-13.
- Dubois, P., Marchand, G., Fouillet, Y., Berthier, J., Douki, T., Hassine, F., Gmouh, S. & Vaultier, M. (2006). Ionic liquid droplet as e-microreactor. *Analytical chemistry*, 78(14), 4909–4917.
- Duchaine, V. & Rana, A. (2014). Dielectric geometry for capacitive-based tactile sensor. Google Patents. US Patent App. 14/762,289.
- Duchaine, V., Lauzier, N., Baril, M., Lacasse, M.-A. & Gosselin, C. (2009). A flexible robot skin for safe physical human robot interaction. *Robotics and automation, 2009. icra'09. ieee international conference on*, pp. 3676–3681.
- Dura Magnetics Website. Accessed: 2017-01-16.
- Elsanadedy, A. (2012). *Application of electrical impedance tomography to robotic tactile sensing*. (Ph.D. thesis, Carleton University).

- Esquenazi, A. (2004). Amputation rehabilitation and prosthetic restoration. from surgery to community reintegration. *Disability and rehabilitation*, 26(14-15), 831–836.
- Fang, K., Weng, C. & Ju, S. (2009). An investigation into the mechanical properties of silicon nanoparticles using molecular dynamics simulations with parallel computing. *Journal of nanoparticle research*, 11(3), 581–588.
- Fassler, A. & Majidi, C. (2013). 3d structures of liquid-phase gain alloy embedded in pdms with freeze casting. *Lab chip*.
- Feliu, V. & Ramos, F. (2005). Strain gauge based control of single-link flexible very lightweight robots robust to payload changes. *Mechatronics*, 15(5), 547–571.
- Ferrara, E., Callegaro, L. & Durbiano, F. (2000). Optimal frequency range for the measurement of ac conductivity in aqueous solutions. *Instrumentation and measurement technology conference, 2000. imtc 2000. proceedings of the 17th ieee*, 2, 775–779.
- Forrest, S. R. (2004). The path to ubiquitous and low-cost organic electronic appliances on plastic. *Nature*, 428(6986), 911–918.
- Garg, P., Aggarwal, N. & Sofat, S. (2009). Vision based hand gesture recognition. *World academy of science, engineering and technology*, 49(1), 972–977.
- Gentner, R. & Classen, J. (2009). Development and evaluation of a low-cost sensor glove for assessment of human finger movements in neurophysiological settings. *Journal of neuroscience methods*, 178(1), 138–147.
- Gilpin, K., Knaian, A. & Rus, D. (2010). Robot pebbles: One centimeter modules for programmable matter through self-disassembly. *Robotics and automation (icra), 2010 ieee international conference on*, pp. 2485–2492.
- Halbach, K. (1980). Design of permanent multipole magnets with oriented rare earth cobalt material. *Nuclear instruments and methods*, 169(1), 1–10.
- Harris, F. & O’Konski, C. (1957). Dielectric properties of aqueous ionic solutions at microwave frequencies. *The journal of physical chemistry*, 61(3), 310–319.
- Hayashi, S., Saha, S. & Hamaguchi, H.-o. (2006). A new class of magnetic fluids: bmim [fecl/sub 4/] and nbmim [fecl/sub 4/] ionic liquids. *Ieee transactions on magnetics*, 42(1), 12–14.
- Hochberg, U., Dietsche, A. & Dorer, K. (2013). Evaporative cooling of actuators for humanoid robots. *Proceedings of the 8th workshop on humanoid soccer robots, ieee-ras international conference on humanoid robots, atlanta*.
- Hoshi, T. & Shinoda, H. (2006). Robot skin based on touch-area-sensitive tactile element. *Robotics and automation, 2006. icra 2006. proceedings 2006 ieee international conference on*, pp. 3463–3468.

- Hsiao, P.-C., Yang, S.-Y., Lin, B.-S., Lee, I.-J. & Chou, W. (2015). Data glove embedded with 9-axis imu and force sensing sensors for evaluation of hand function. *Engineering in medicine and biology society (embc), 2015 37th annual international conference of the ieee*, pp. 4631–4634.
- Hu, N., Karube, Y., Yan, C., Masuda, Z. & Fukunaga, H. (2008). Tunneling effect in a polymer/carbon nanotube nanocomposite strain sensor. *Acta materialia*, 56(13), 2929–2936.
- Ingram, J. N., K rding, K. P., Howard, I. S. & Wolpert, D. M. (2008). The statistics of natural hand movements. *Experimental brain research*, 188(2), 223–236.
- Insinga, A. R., Bahl, C., Bj rk, R. & Smith, A. (2016). Performance of halbach magnet arrays with finite coercivity. *Journal of magnetism and magnetic materials*, 407, 369–376.
- Irshad, W. & Peroulis, D. (2009). A silicon-based galinstan magnetohydrodynamic pump. *Proceedings of the 9th international workshop on micro and nanotechnology for power generation and energy conversion applications (powermems)*, pp. 127–129.
- Johnson, O., Kaschner, G., Mason, T., Fullwood, D., Hyatt, T., Adams, B., Cole, K. & Hansen, G. (2010a). Extreme piezoresistivity of silicone/nickel nanocomposites for high resolution large strain measurement. *Minerals, metals and materials society (tms)*.
- Johnson, O., Gardner, C., Fullwood, D., Adams, B., Hansen, N. & Hansen, G. (2010b). The colossal piezoresistive effect in nickel nanostrand polymer composites and a quantum tunneling model. *Computers, materials, & continua*, 15(2), 87–112.
- Joshiyura, I. D., Ayers, H. R., Majidi, C. & Dickey, M. D. (2015). Methods to pattern liquid metals. *Journal of materials chemistry c*, 3(16), 3834–3841.
- Kang, I., Schulz, M., Kim, J., Shanov, V. & Shi, D. (2006). A carbon nanotube strain sensor for structural health monitoring. *Smart materials and structures*, 15, 737.
- Kato, Y., Mukai, T., Hayakawa, T. & Shibata, T. (2007). Tactile sensor without wire and sensing element in the tactile region based on EIT method. *Sensors, 2007 ieee*, pp. 792–795.
- Kejlaa, G. (1993). Consumer concerns and the functional value of prostheses to upper limb amputees. *Prosthetics and orthotics international*, 17(3), 157–163.
- Kiesel, S., Peters, K., Hassan, T. & Kowalsky, M. (2007). Behaviour of intrinsic polymer optical fibre sensor for large-strain applications. *Measurement science and technology*, 18(10), 3144.
- Kim, D., Hilliges, O., Izadi, S., Butler, A. D., Chen, J., Oikonomidis, I. & Olivier, P. (2012). Digits: freehand 3d interactions anywhere using a wrist-worn gloveless sensor. *Proceedings of the 25th annual acm symposium on user interface software and technology*, pp. 167–176.

- Knaian, A. N. (2010). *Electropermanent magnetic connectors and actuators: devices and their application in programmable matter*. (Ph.D. thesis, Citeseer).
- Knite, M., Teteris, V., Kiploka, A. & Kaupuzs, J. (2004). Polyisoprene-carbon black nanocomposites as tensile strain and pressure sensor materials. *Sensors and actuators a: Physical*, 110(1), 142–149.
- Kortier, H. G., Sluiter, V. I., Roetenberg, D. & Veltink, P. H. (2014). Assessment of hand kinematics using inertial and magnetic sensors. *Journal of neuroengineering and rehabilitation*, 11(1), 70.
- Kost, J., Foux, A. & Narkis, M. (1994). Quantitative model relating electrical resistance, strain, and time for carbon black loaded silicone rubber. *Polymer engineering & science*, 34(21), 1628–1634.
- Kotre, C. (1994). EIT image reconstruction using sensitivity weighted filtered backprojection. *Physiological measurement*, 15(2A), A125.
- Kozuki, T., Toshinori, H., Shirai, T., Nakashima, S., Asano, Y., Kakiuchi, Y., Okada, K. & Inaba, M. (2016). Skeletal structure with artificial perspiration for cooling by latent heat for musculoskeletal humanoid kengoro. *Intelligent robots and systems (iros), 2016 IEEE/RSJ International Conference on*, pp. 2135–2140.
- Kramer, R. K., Majidi, C. & Wood, R. J. (2011a). Wearable tactile keypad with stretchable artificial skin. *Robotics and automation (icra), 2011 IEEE International Conference on*, pp. 1103–1107.
- Kramer, R. K., Majidi, C. & Wood, R. J. (2013). Masked deposition of gallium-indium alloys for liquid-embedded elastomer conductors. *Advanced functional materials*, 23(42), 5292–5296.
- Kramer, R., Majidi, C., Sahai, R. & Wood, R. J. (2011b). Soft curvature sensors for joint angle proprioception. *Intelligent robots and systems (iros), 2011 IEEE/RSJ International Conference on*, pp. 1919–1926.
- Lacasse, M., Duchaine, V. & Gosselin, C. (2010). Characterization of the electrical resistance of carbon-black-filled silicone: Application to a flexible and stretchable robot skin. *Robotics and automation (icra), 2010 IEEE International Conference on*, pp. 4842–4848.
- Lacasse, M.-A., Lachance, G., Boisclair, J., Ouellet, J. & Gosselin, C. (2013). On the design of a statically balanced serial robot using remote counterweights. *Robotics and automation (icra), 2013 IEEE International Conference on*, pp. 4189–4194.
- Làdavas, E. & Pavani, F. (1998). Neuropsychological evidence of the functional integration of visual, auditory and proprioceptive spatial maps. *Neuroreport*, 9(6), 1195–1200.
- Lambert, P. (2013). *Surface tension in microsystems - engineering below the capillary length*. Springer.

- LaViola, J. (1999). A survey of hand posture and gesture recognition techniques and technology. *Brown university, providence, ri*, 29.
- Le, T.-H.-L., Maslyczyk, A., Roberge, J.-P. & Duchaine, V. (2017). A highly sensitive multi-modal capacitive tactile sensor.
- Lee, J., Moon, H., Fowler, J., Schoellhammer, T. & Kim, C.-J. (2002). Electrowetting and electrowetting-on-dielectric for microscale liquid handling. *Sensors and actuators a: Physical*, 95(2), 259–268.
- Lee, P., Lee, J., Lee, H., Yeo, J., Hong, S., Nam, K. H., Lee, D., Lee, S. S. & Ko, S. H. (2012). Highly stretchable and highly conductive metal electrode by very long metal nanowire percolation network. *Advanced materials*, 24(25), 3326–3332.
- Li, K., Chen, I.-M., Yeo, S. H. & Lim, C. K. (2011a). Development of finger-motion capturing device based on optical linear encoder. *Journal of rehabilitation research and development*, 48(1), 69.
- Li, L., Rutlin, M., Abairra, V. E., Cassidy, C., Kus, L., Gong, S., Jankowski, M. P., Luo, W., Heintz, N., Koerber, H. R. et al. (2011b). The functional organization of cutaneous low-threshold mechanosensory neurons. *Cell*, 147(7), 1615–1627.
- Lin, B. S., Lee, I. J., Hsiao, P. C., Yang, S. Y. & Chou, W. (2014). Data glove embedded with 6-dof inertial sensors for hand rehabilitation. *Intelligent information hiding and multimedia signal processing (iih-msp), 2014 tenth international conference on*, pp. 25–28.
- Lipomi, D., Tee, B., Vosgueritchian, M. & Bao, Z. (2011). Stretchable organic solar cells. *Advanced materials*, 23(15), 1771–1775.
- Liu, T., Sen, P. & Kim, C. (2010). Characterization of liquid-metal galinstan® for droplet applications. *Micro electro mechanical systems (mems), 2010 ieee 23rd international conference on*, pp. 560–563.
- Loh, K., Lynch, J., Shim, B. & Kotov, N. (2008). Tailoring piezoresistive sensitivity of multi-layer carbon nanotube composite strain sensors. *Journal of intelligent material systems and structures*, 19(7), 747–764.
- Lu, T., Markvicka, E., Jin, Y. & Majidi, C. (2017). Soft-matter printed circuit board with uv laser micropatterning. *Acs applied materials & interfaces*.
- Luebbers, P. & Chopra, O. (1995). Compatibility of iter candidate materials with static gallium. *Fusion engineering, 1995. sofe'95.'seeking a new energy era'., 16th ieee/npss symposium*, 1, 232–235.
- Lumelsky, V., Shur, M. S. & Wagner, S. (2000). *Sensitive skin*. World Scientific.

- Maggiali, M., Cannata, G., Maiolino, P., Metta, G., Randazzo, M. & Sandini, G. (2008). Embedded distributed capacitive tactile sensor. *11th mechatronics forum biennial international conference*.
- Majidi, C., Kramer, R. & Wood, R. (2011). A non-differential elastomer curvature sensor for softer-than-skin electronics. *Smart materials and structures*, 20(10), 105017.
- Mallinson, J. (1973). One-sided fluxes—a magnetic curiosity? *Ieee transactions on magnetics*, 9(4), 678–682.
- Malvezzi, M., Gioioso, G., Salvietti, G., Prattichizzo, D. & Bicchi, A. (2013, May). Syngrasp: a MATLAB toolbox for grasp analysis of human and robotic hands. *Proc. ieee int. conf. rob. autom. (icra'13)*, pp. 1088-1093.
- Maravita, A. & Iriki, A. (2004). Tools for the body (schema). *Trends in cognitive sciences*, 8(2), 79–86.
- Marchese, A. D., Onal, C. D. & Rus, D. (2011). Soft robot actuators using energy-efficient valves controlled by electropermanent magnets. *2011 ieee/rsj international conference on intelligent robots and systems*, pp. 756–761.
- Marsh, K., Boxall, J. & Lichtenthaler, R. (2004). Room temperature ionic liquids and their mixtures—a review. *Fluid phase equilibria*, 219(1), 93–98.
- McAdams, E., Lackermeier, A., McLaughlin, J., Macken, D. & Jossinet, J. (1995). The linear and non-linear electrical properties of the electrode-electrolyte interface. *Biosensors and bioelectronics*, 10(1), 67–74.
- Mitobe, K., Kaiga, T., Yukawa, T., Miura, T., Tamamoto, H., Rodgers, A. & Yoshimura, N. (2006). Development of a motion capture system for a hand using a magnetic three dimensional position sensor. *Siggraph research posters*, pp. 102.
- Nagakubo, A., Alirezaei, H. & Kuniyoshi, Y. (2007). A deformable and deformation sensitive tactile distribution sensor. *Robotics and biomimetics, 2007. robio 2007. ieee international conference on*, pp. 1301–1308.
- NicaDrone website. (2017). OpenGrab EPM. Accessed: 2016-12-05.
- Noda, K., Iwase, E., Matsumoto, K. & Shimoyama, I. (2010). Stretchable liquid tactile sensor for robot-joints. *Robotics and automation (icra), 2010 ieee international conference on*, pp. 4212–4217.
- Paine, N., Mehling, J. S., Holley, J., Radford, N. A., Johnson, G., Fok, C.-L. & Sentis, L. (2015). Actuator control for the nasa-jsc valkyrie humanoid robot: A decoupled dynamics approach for torque control of series elastic robots. *Journal of field robotics*, 32(3), 378–396.

- Park, Y.-L., Ryu, S. C., Black, R. J., Chau, K. K., Moslehi, B. & Cutkosky, M. R. (2009). Exoskeletal force-sensing end-effectors with embedded optical fiber-bragg-grating sensors. *Robotics, iee transactions on*, 25(6), 1319–1331.
- Park, Y.-L., Majidi, C., Kramer, R., Bérard, P. & Wood, R. J. (2010). Hyperelastic pressure sensing with a liquid embedded elastomer. *Journal of micromechanics and microengineering*, 20(12).
- Park, Y.-L., Chen, B. & Wood, R. J. (2012a). Design and fabrication of soft artificial skin using embedded microchannels and liquid conductors. *Sensors journal, ieee*, 12(8), 2711–2718.
- Park, Y.-L., Tepayotl-Ramirez, D., Wood, R. J. & Majidi, C. (2012b). Influence of cross-sectional geometry on the sensitivity and hysteresis of liquid-phase electronic pressure sensors. *Applied physics letters*, 101(19).
- Park, Y.-L., Chen, B.-r., Pérez-Arancibia, N. O., Young, D., Stirling, L., Wood, R. J., Goldfield, E. C. & Nagpal, R. (2014). Design and control of a bio-inspired soft wearable robotic device for ankle–foot rehabilitation. *Bioinspiration & biomimetics*, 9(1), 016007.
- Pezzin, L. E., Dillingham, T. R., MacKenzie, E. J., Ephraim, P. & Rossbach, P. (2004). Use and satisfaction with prosthetic limb devices and related services. *Archives of physical medicine and rehabilitation*, 85(5), 723–729.
- Prattichizzo, D., Malvezzi, M. & Bicchi, A. (2010). On motion and force control of grasping hands with postural synergies.
- Proske, U. (2015). The role of muscle proprioceptors in human limb position sense: a hypothesis. *Journal of anatomy*, 227(2), 178–183.
- Raich, H. & Blümler, P. (2004). Design and construction of a dipolar halbach array with a homogeneous field from identical bar magnets: Nmr mandhalas. *Concepts in magnetic resonance part b: Magnetic resonance engineering*, 23(1), 16–25.
- Raichle, K. A., Hanley, M. A., Molton, I., Kadel, N. J., Campbell, K., Phelps, E., Ehde, D. & Smith, D. G. (2008). Prosthesis use in persons with lower-and upper-limb amputation. *Journal of rehabilitation research and development*, 45(7), 961.
- Rana, A., Roberge, J.-P. & Duchaine, V. (2016). An improved soft dielectric for a highly sensitive capacitive tactile sensor. *Ieee sensors journal*, 16(22), 7853–7863.
- Rispol, S., Rana, A. K. & Duchaine, V. (2017a). Texture roughness estimation using dynamic tactile sensing. *Control, automation and robotics (iccar), 2017 3rd international conference on*, pp. 555–562.
- Rispol, S., Rana, A. K. & Duchaine, V. (2017b). Textures recognition through tactile exploration for robotic applications. *Control, automation and robotics (iccar), 2017 3rd international conference on*, pp. 121–128.

- Rogers, J. A., Someya, T. & Huang, Y. (2010). Materials and mechanics for stretchable electronics. *Science*, 327(5973), 1603–1607.
- Sacks, O. (2009). *The man who mistook his wife for a hat*. Picador.
- Sainburg, R. L., Ghilardi, M. F., Poizner, H. & Ghez, C. (1995). Control of limb dynamics in normal subjects and patients without proprioception. *Journal of neurophysiology*, 73(2), 820–835.
- Santello, M., Flanders, M. & Soechting, J. F. (1998). Postural hand synergies for tool use. *Journal of neuroscience*, 18(23), 10105–10115.
- Seok, S., Wang, A., Chuah, M. Y., Otten, D., Lang, J. & Kim, S. (2013). Design principles for highly efficient quadrupeds and implementation on the mit cheetah robot. *Robotics and automation (icra), 2013 ieee international conference on*, pp. 3307–3312.
- Seok, S., Wang, A., Chuah, M. Y. M., Hyun, D. J., Lee, J., Otten, D. M., Lang, J. H. & Kim, S. (2015). Design principles for energy-efficient legged locomotion and implementation on the mit cheetah robot. *Ieee/asme transactions on mechatronics*, 20(3), 1117–1129.
- Shaikh, K. & Liu, C. (2007). A bi-stable latchable pdms valve employing low melting temperature metal alloys. *Solid-state sensors, actuators and microsystems conference, 2007. transducers 2007. international*, pp. 2199–2202.
- Shimojo, M., Namiki, A., Ishikawa, M., Makino, R. & Mabuchi, K. (2004). A tactile sensor sheet using pressure conductive rubber with electrical-wires stitched method. *Ieee sensors journal*, 4(5), 589–596.
- Simone, L. K., Sundarajan, N., Luo, X., Jia, Y. & Kamper, D. G. (2007). A low cost instrumented glove for extended monitoring and functional hand assessment. *Journal of neuroscience methods*, 160(2), 335–348.
- Soltner, H. & Blümler, P. (2010). Dipolar halbach magnet stacks made from identically shaped permanent magnets for magnetic resonance. *Concepts in magnetic resonance part a*, 36(4), 211–222.
- Someya, T., Bao, Z. & Malliaras, G. G. (2016). The rise of plastic bioelectronics. *Nature*, 540(7633), 379–385.
- Stucki, P. (1992). Algorithms and procedures for digital halftone generation. *Spie/is&t 1992 symposium on electronic imaging: Science and technology*, pp. 26–40.
- Sturman, D. J. & Zeltzer, D. (1994). A survey of glove-based input. *Ieee computer graphics and applications*, 14(1), 30–39.
- Suganuma, F., Shimamoto, A. & Tanaka, K. (1999). Development of a differential optical-fiber displacement sensor. *Applied optics*, 38(7), 1103–1109.

- Sung, H. & Rudowicz, C. (2003). Physics behind the magnetic hysteresis loop—a survey of misconceptions in magnetism literature. *Journal of magnetism and magnetic materials*, 260(1), 250–260.
- Tabatabai, A., Fassler, A., Usiak, C. & Majidi, C. (2013). Liquid-phase gallium-indium alloy electronics with microcontact printing. *Langmuir*, 29(20), 6194–6200.
- Tawil, D. S., Rye, D. & Velonaki, M. (2009). Improved eit drive patterns for a robotics sensitive skin. *Proceeding of australasian conference on robotics and automation (acra)*, pp. 2–4.
- Tee, B. C., Wang, C., Allen, R. & Bao, Z. (2012). An electrically and mechanically self-healing composite with pressure- and flexion-sensitive properties for electronic skin applications. *Nature nanotechnology*, 7(12), 825–832.
- To, C., Hellebrekers, T. L. & Park, Y.-L. (2015). Highly stretchable optical sensors for pressure, strain, and curvature measurement. *Intelligent robots and systems (iros), 2015 IEEE/RSJ International Conference on*, pp. 5898–5903.
- Todorov, E. & Ghahramani, Z. (2004). Analysis of the synergies underlying complex hand manipulation. *Engineering in medicine and biology society, 2004. iembs'04. 26th annual international conference of the IEEE*, 2, 4637–4640.
- Ulmen, J. & Cutkosky, M. (2010). A robust, low-cost and low-noise artificial skin for human-friendly robots. *Robotics and automation (icra), 2010 IEEE International Conference on*, pp. 4836–4841.
- Urata, J., Hirose, T., Namiki, Y., Nakanishi, Y., Mizuuchi, I. & Inaba, M. (2008). Thermal control of electrical motors for high-power humanoid robots. *2008 IEEE/RSJ International Conference on Intelligent Robots and Systems*, pp. 2047–2052.
- Urata, J., Nakanishi, Y., Okada, K. & Inaba, M. (2010). Design of high torque and high speed leg module for high power humanoid. *Intelligent robots and systems (iros), 2010 IEEE/RSJ International Conference on*, pp. 4497–4502.
- Vallbo, Å. B., Johansson, R. S. et al. (1984). Properties of cutaneous mechanoreceptors in the human hand related to touch sensation. *Hum neurobiol*, 3(1), 3–14.
- Vallbo, A. & Johansson, R. S. (1976). Skin mechanoreceptors in the human hand: neural and psychophysical thresholds. *Sensory functions of the skin in primates*, 185–99.
- Vauhkonen, M., Lionheart, W. R., Heikkinen, L. M., Vauhkonen, P. J. & Kaipio, J. P. (2001). A matlab package for the eiders project to reconstruct two-dimensional eit images. *Physiological measurement*, 22(1), 107.
- Visser, A. E., Bridges, N. J. & Rogers, R. D. (2009). *Ionic liquids: Science and applications*. OUP USA.

- Vogt, D. M., Park, Y.-L. & Wood, R. J. (2013). Design and characterization of a soft multi-axis force sensor using embedded microfluidic channels. *Ieee sensors journal*, 13(10), 4056-4064.
- Wang, P., Zakeeruddin, S. M., Comte, P., Exnar, I. & Grätzel, M. (2003). Gelation of ionic liquid-based electrolytes with silica nanoparticles for quasi-solid-state dye-sensitized solar cells. *Journal of the american chemical society*, 125(5), 1166–1167.
- Wei, D. & Ivaska, A. (2008). Applications of ionic liquids in electrochemical sensors. *Analytica chimica acta*, 607(2), 126–135.
- Wensing, P. M., Wang, A., Seok, S., Otten, D., Lang, J. & Kim, S. (2017). Proprioceptive actuator design in the mit cheetah: Impact mitigation and high-bandwidth physical interaction for dynamic legged robots. *Ieee transactions on robotics*.
- Whitesides, G. M. (2006). The origins and the future of microfluidics. *Nature*, 442(7101), 368.
- Wikipedia, Electropermanent magnet. (2017). Electropermanent magnet, Wikipedia, The Free Encyclopedia. Online; accessed 12-August-2017].
- Williams, N., Penrose, J., Caddy, C., Barnes, E., Hose, D. & Harley, P. (2000). A goniometric glove for clinical hand assessment: construction, calibration and validation. *Journal of hand surgery*, 25(2), 200–207.
- Wise, S., Gardner, W., Sabelman, E., Valainis, E., Wong, Y., Glass, K., Drace, J. & Rosen, J. M. (1990). Evaluation of a fiber optic glove for semi-automated goniometric measurements. *Journal of rehabilitation research and development*, 27(4), 411.
- Wong, R. D. P., Posner, J. D. & Santos, V. J. (2012). Flexible microfluidic normal force sensor skin for tactile feedback. *Sensors and actuators a: Physical*, 179, 62-69.
- Wu, C.-Y., Liao, W.-H. & Tung, Y.-C. (2011). Integrated ionic liquid-based electrofluidic circuits for pressure sensing within polydimethylsiloxane microfluidic systems. *Lab on a chip*, 11(10), 1740–1746.
- Xu, Q., Oudalov, N., Guo, Q., Jaeger, H. M. & Brown, E. (2012). Effect of oxidation on the mechanical properties of liquid gallium and eutectic gallium-indium. *Physics of fluids*, 24(6), 063101.
- Yan, J. & Pan, T. (2011). An ultra-high sensitivity, capacitive pressure sensor using ionic liquid. *Micro electro mechanical systems (mems), 2011 ieee 24th international conference on*, pp. 557–560.
- Yang, J.-Z., Lu, X.-M., Gui, J.-S. & Xu, W.-G. (2004). A new theory for ionic liquids—the interstice model part 1. the density and surface tension of ionic liquid emise. *Green chemistry*, 6(11), 541–543.

- Ying, H., Xiulan, F., Min, W., Panfeng, H. & Yunjian, G. (2007). Research on nano-sio₂/carbon black composite for flexible tactile sensing. *Information acquisition, 2007. icia'07. international conference on*, pp. 260–264.
- Zhao, H., O'Brien, K., Li, S. & Shepherd, R. F. (2016). Optoelectronically innervated soft prosthetic hand via stretchable optical waveguides. *Science robotics*, 1(1), eaai7529.
- Zhu, Y., Chao, C., Cheng, C.-H. & Leung, W. W.-F. (2009). A novel ionic-liquid strain sensor for large-strain applications. *Ieee electron device letters*, 30(4), 337–339.
- Zucker, O., Langheinrich, W., Kulozik, M. & Goebel, H. (1993). Application of oxygen plasma processing to silicon direct bonding. *Sensors and actuators a: Physical*, 36(3), 227–231.
- Zuo, G., Zhao, Z., Yan, S. & Zhang, X. (2010). Thermodynamic properties of a new working pair: 1-ethyl-3-methylimidazolium ethylsulfate and water. *Chemical engineering journal*, 156(3), 613–617.